


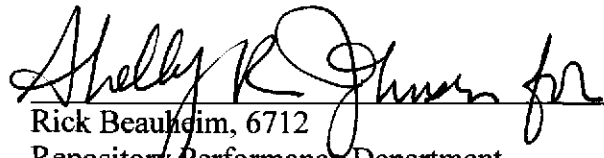
553276

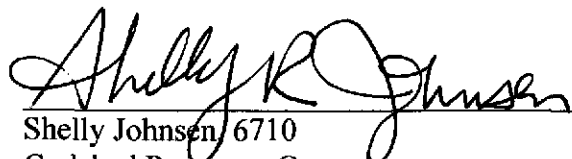
## Development of Culebra T Fields for CRA 2009 PABC

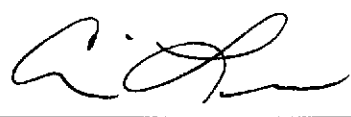
Task Number: 1.2.5

4/1/2010

Author:   
Kristopher L. Kuhlman, 6712  
Repository Performance Department 4/1/2010  
Date

Technical Review:   
Rick Beauheim, 6712  
Repository Performance Department 4-1-10  
Date

QA Review:   
Shelly Johnson, 6710  
Carlsbad Programs Group 4-1-10  
Date

Management Review:   
Christi Leigh, 6712  
Repository Performance Department 4-1-10  
Date

WIPP:1.2.5:PA:QA-L:549013

Information Only

1 of 114

## Contents

<i>List of Figures</i> .....	5
<b>TFIELD-1 Overview of the T-Field Development, Calibration, and Modification Process</b> .....	<b>11</b>
<b>TFIELD-2 Geologic Data</b> .....	<b>13</b>
<i>TFIELD-2.1 Refine Geologic Boundaries</i> .....	13
TFIELD-2.1.1 Rustler Halite Margins .....	13
TFIELD-2.1.2 Salado Dissolution .....	18
<i>TFIELD-2.2 Confinement and Recharge in the Culebra</i> .....	19
TFIELD-2.2.1 Surface Drainage Basins .....	19
TFIELD-2.2.2 Culebra Confinement .....	21
<b>TFIELD-3 T-Field Conceptual Model</b> .....	<b>24</b>
<i>TFIELD-3.1 Model Domain</i> .....	26
<i>TFIELD-3.2 Overburden Thickness</i> .....	26
<i>TFIELD-3.3 Fracture Interconnection</i> .....	28
<i>TFIELD-3.4 Salado Dissolution</i> .....	28
<i>TFIELD-3.5 Rustler Halite Margins</i> .....	29
<i>TFIELD-3.6 High-Transmissivity Zones</i> .....	29
<i>TFIELD-3.7 Linear Transmissivity Model</i> .....	29
<b>TFIELD-4 T-Field Construction Using Indicator Kriging</b> .....	<b>32</b>
<i>TFIELD-4.1 Step 1 – Linear Regression Analysis</i> .....	32
<i>TFIELD-4.2 Step 2 – Creation of “Soft Data”</i> .....	33
TFIELD-4.2.1 Halite Bounding .....	35
TFIELD-4.2.2 Gypsum Cements .....	35
TFIELD-4.2.3 Diffusivity and Hydraulic Connections .....	40
TFIELD-4.2.4 Combined Soft Data.....	41
<i>TFIELD-4.3 Step 3 – Indicator Variography</i> .....	41
<i>TFIELD-4.4 Step 4 – Conditional Indicator Simulation</i> .....	42

<i>TFIELD-4.5</i>	<i>Step 5 – Construction of Transmissivity Fields</i> .....	45
<b>TFIELD-5</b>	<b>T-Field Calibration</b> .....	<b>50</b>
<i>TFIELD-5.1</i>	<i>Model Calibration Targets</i> .....	51
<i>TFIELD-5.2</i>	<i>Step 1 – Calibration Setup and Configuration</i> .....	53
<i>TFIELD-5.2.1</i>	Creation of Parameter Zones.....	53
<i>TFIELD-5.2.2</i>	Selection of Pilot Point Locations.....	59
<i>TFIELD-5.2.3</i>	Transmissivity-Specific Pilot Point Settings.....	60
<i>TFIELD-5.2.4</i>	Anisotropy-Specific Pilot Point Settings .....	61
<i>TFIELD-5.2.5</i>	Storativity-Specific Pilot Point Settings.....	61
<i>TFIELD-5.2.6</i>	Recharge-Specific Pilot Point Settings .....	62
<i>TFIELD-5.2.7</i>	Selection of Initial Values.....	63
<i>TFIELD-5.2.8</i>	Creation of Transmissivity Fields .....	65
<i>TFIELD-5.2.9</i>	Observations and Residuals .....	66
<i>TFIELD-5.2.10</i>	MODFLOW Numerical Model .....	66
<i>TFIELD-5.3</i>	<i>Step 2 – Inverse Calibration Process</i> .....	67
<i>TFIELD-5.3.1</i>	PEST Calibration Process .....	67
<i>TFIELD-5.3.2</i>	Calibrated Correction of Steady-State Head Values .....	69
<i>TFIELD-5.3.3</i>	Evaluation of Impact of Multiple Calibration Processes.....	70
<i>TFIELD-5.3.4</i>	Selection of Best-Calibrated Fields.....	71
<i>TFIELD-5.4</i>	<i>Step 3 – Post-Calibration Analysis</i> .....	73
<i>TFIELD-5.4.1</i>	Statistical Analysis of Resulting T, A, and S Fields .....	73
<i>TFIELD-5.4.2</i>	Forward Model Results using the Calibrated Fields .....	83
<b>TFIELD-6</b>	<b>Culebra T-Field Mining Modifications</b> .....	<b>86</b>
<i>TFIELD-6.1</i>	<i>Overview</i> .....	86
<i>TFIELD-6.2</i>	<i>Model Domain, Boundary, and Initial Conditions</i> .....	87
<i>TFIELD-6.2.1</i>	Boundary and Initial Conditions .....	88

TFIELD-6.2.2	Determination of Potential Mining Areas .....	89
TFIELD-6.2.3	Use of Mining Zones in Forward Simulations .....	93
TFIELD-6.2.4	Particle Tracking Simulations .....	93
<i>TFIELD-6.3</i>	<i>Particle Tracking Results</i> .....	<i>94</i>
TFIELD-6.3.1	Particle Travel Times .....	94
TFIELD-6.3.2	Flow Directions .....	96
TFIELD-6.3.3	Particle Speeds .....	101
TFIELD-6.3.4	Particle Tracking Discussion .....	104
<i>TFIELD-6.4</i>	<i>Mining Modification Summary</i> .....	<i>106</i>
<b>TFIELD-7</b>	<b>Summary</b> .....	<b>107</b>
<b>TFIELD-8</b>	<b>References</b> .....	<b>108</b>

## List of Figures

Figure TFIELD 2-1. Generalized stratigraphy near WIPP .....	13
Figure TFIELD 2-2. Stratigraphic nomenclature of the Rustler Formation. ....	14
Figure TFIELD 2-3. M-1/H-1 halite margin in the lower Los Medaños Member .....	16
Figure TFIELD 2-4. M-2/H-2 halite margin in the upper Los Medaños Member .....	16
Figure TFIELD 2-5. M-3/H-3 halite margin in the Tamarisk Member .....	16
Figure TFIELD 2-6. M-4/H-4 halite margin in the Forty-niner Member .....	16
Figure TFIELD 2-7. Salado dissolution and Rustler mudstone/halite margins.....	17
Figure TFIELD 2-8. Elevation (m above mean sea level) of top of Culebra member of Rustler Formation.....	18
Figure TFIELD 2-9. Closed drainage sub-basins identified in southern Nash Draw; white areas either outside Nash Draw or outside the study area.....	21
Figure TFIELD 2-10. Culebra confinement map for southern Nash Draw study area; white areas outside study area.....	23
Figure TFIELD 3-1. Culebra Dolomite conceptual model near WIPP. Culebra T values decrease to the east (increasing overburden and halite), and fracturing increases to the west (Salado dissolution zone). Halite appears both above (H-3) and below (H-2) the Culebra in the east. ....	24
Figure TFIELD 3-2. The model domain with margins and wells.....	25
Figure TFIELD 3-3. Thickness of Culebra overburden.....	27
Figure TFIELD 3-4. Histogram of $\log_{10}$ Culebra transmissivity.....	28
Figure TFIELD 3-5. Conceptual model zones with indicator values and zone numbers (Equation TFIELD 3.2). ....	31
Figure TFIELD 4-1. Regression lines for low-T wells (blue), high-T/non-dissolution wells (green), and wells within the Salado dissolution zone (red). ....	33
Figure TFIELD 4-2. Areas where no gypsum has been found in core samples. A selection of points within this area received low $P_{low}$ values, indicating the greater likelihood of having higher T values. ....	37

Figure TFIELD 4-3. Areas where wells have either no or low gypsum content. The areas not shaded, therefore, are likely to have high gypsum content and lower T, and this white area receives high  $P_{low}$  values. .... 38

Figure TFIELD 4-4. Diffusivity values calculated between wells from pumping test data. Connections where  $\log_{10}D > 0.2$  are included as conditioning data with  $P_{low} = 0.25$ . .... 39

Figure TFIELD 4-5. Soft data points (open symbols) generated during step 2. Hard data points (filled symbols) are located at wells with pumping test estimates of T. .... 40

Figure TFIELD 4-6. Experimental variogram (dots) and spherical model (line) for indicator values.  $x$ -axis is lag distance [meters],  $y$ -axis is the unitless indicator. .... 42

Figure TFIELD 4-7. Sample indicator field for realization r123, where 1 indicates low T and 0 indicates high T. .... 43

Figure TFIELD 4-8. Average indicator values across all 1000 base realizations. .... 44

Figure TFIELD 4-9. Standard deviation of indicator values across all 1000 base realizations. .... 45

Figure TFIELD 4-10. Sample  $\log_{10} T$  base field realization: r123. .... 47

Figure TFIELD 4-11. Mean  $\log_{10} T$  values across all 1000 base realizations. .... 48

Figure TFIELD 4-12. Standard deviation of  $\log_{10} T$  values across all 1000 base realizations. .... 49

Figure TFIELD 5-1. Transmissivity zone map for a single realization. Zones 0 and 1 are the stochastic zones created in (Hart et al., 2008); Zone 2 is the high-T Salado dissolution area; Zone 3 is the very low-T halite-bounded area; Zone4 is inactive (no flow). .... 55

Figure TFIELD 5-2. Storativity zones; Zone 0 is confined; Zone 1 is transition between confined and unconfined; Zone 2 is unconfined; Zone 3 is confined and held static at the initial confined value; Zone 4 is inactive (no flow) .... 57

Figure TFIELD 5-3. Zone 1 is the area of recharge; the remaining area had no recharge. .... 58

Figure TFIELD 5-4. Flow zones: the fixed-head zone is green; the no-flow zone is salmon; the white area is normal flow. The fixed-head zone includes one cell along the boundaries. .... 59

Figure TFIELD 5-5. Transmissivity pilot point locations. Blue points are fixed values and red points are variable parameters. .... 60

Figure TFIELD 5-6. Anisotropy pilot point locations. All anisotropy pilot points were variable parameters. .... 61

Figure TFIELD 5-7. Storativity pilot point locations. Only pilot points along transient pumping test connections and points in the unconfined zones (zones 1 and 2) were variable (red dots), the remaining points were fixed at the initial storativity value (blue dots). ..... 62

Figure TFIELD 5-8. Recharge pilot point locations. .... 63

Figure TFIELD 5-9. Initial head values for use in MODFLOW steady-state solution. Brick red head values were fixed at the ground surface elevation (>1,000 m AMSL). ..... 65

Figure TFIELD 5-10. Flow chart showing the numerical model used in the inverse calibration. ... 67

Figure TFIELD 5-11. The PEST calibration process. .... 68

Figure TFIELD 5-12. Complete calibration process for a single field. .... 69

Figure TFIELD 5-13. Recalibration boundary shown in red to the northeast of the WIPP site. Recalibration boundary limits are UTM X and Y NAD27 Zone 13 (m). .... 70

Figure TFIELD 5-14. Selection of best fields from all fields - graph of steady-state errors vs. pumping test errors. .... 73

Figure TFIELD 5-15. Mean effective transmissivity for zones 0-2 across the 100 final selected fields. .... 75

Figure TFIELD 5-16. Standard deviation of effective transmissivity for all zones across the 100 final selected fields. .... 76

Figure TFIELD 5-17. High-T zone membership calculated for the base T values. .... 77

Figure TFIELD 5-18. High-T zone membership, calculated for the calibrated T values. .... 78

Figure TFIELD 5-19. Number of fields where low-T became high-T. .... 79

Figure TFIELD 5-20. Number of fields where high T became low T. .... 80

Figure TFIELD 5-21. Mean storativity values across the 100 final calibrated fields. Values in zone 3 (halite-bounded) are non-zero due to an applied shifting term. .... 81

Figure TFIELD 5-22. Standard deviation of storativity values across the 100 final calibrated fields. Red oval shows P-14 to WIPP-25 area of influence. Values in zone 3 (halite-bounded) are non-zero due to an applied shifting term. .... 82

Figure TFIELD 5-23. Recharge as viewed through columns from the south. The initial value was set at  $10^{-3.5}$  m/year. The sharp dropoff to the west is the transition to the single fixed-recharge point of  $10^{-11.5}$  m/year (interpreted as zero by REAL2MOD). .... 83

Figure TFIELD 5-24. Results for 42 of the 44 total steady-state head measurements for the 100 selected fields. Observed heads are red X's along the diagonal line. Wells SNL-6 and SNL-15 are not included because they are located in the fixed-head region of the model. .... 84

Figure TFIELD 5-25. Histogram of steady-state head errors for the 100 selected fields (not including wells SNL-6 and SNL-15). Red dashed line is the  $\pm 3\sigma$  section of the measurement error PDF. The slight skew to right is an artifact of the binning. .... 85

Figure TFIELD 6-1. Comparison of minable potash to the flow and transport modeling domains; green hatched area from BLM shapefile (Cranston, 2009). .... 89

Figure TFIELD 6-2. Stencil used to expand areas of predicted potash (red cell with M) to model cells affected by mining-related subsidence from 45° angle of draw (blue cells with A) ..... 90

Figure TFIELD 6-3. Definitions of mining-affected areas in full-mining scenario between current and previous models. Base image is Figure 3.2 from Lowry and Kanney (2005). .... 91

Figure TFIELD 6-4. Definitions of partial-mining-affected areas between current and previous applications; base image is Figure 3.3 from Lowry and Kanney (2005). .... 92

Figure TFIELD 6-5. Comparison of minable potash distribution inside WIPP LWB for PABC-2004 (dark gray) and PABC-2009 (translucent green). The WIPP repository plan is shown for comparison, from Figure 3.6 of Lowry and Kanney (2005) ..... 93

Figure TFIELD 6-6. CDF of advective particle travel times from the center of the WIPP waste panels to the WIPP LWB for full, partial, and non-mining scenarios ..... 95

Figure TFIELD 6-7. Comparison of advective particle travel time CDFs for PABC-2009, PABC-2004, and CCA. .... 96

Figure TFIELD 6-8. Particle tracks for non-mining scenario; black box is WIPP LWB, green circles are Culebra monitoring well locations. .... 97

Figure TFIELD 6-9. Particle tracks for R1. Small magenta squares and black crosses indicate centers of MODFLOW cells located within potash and mining-affected areas, respectively; thin black line is minable potash definition. .... 97

Figure TFIELD 6-10. Particle tracks for R2. Small magenta squares and black crosses indicate centers of MODFLOW cells located within potash and mining-affected areas, respectively; thin black line is minable potash definition. .... 98

Figure TFIELD 6-11. Particle tracks for R3. Small magenta squares and black crosses indicate centers of MODFLOW cells located within potash and mining-affected areas, respectively; thin black line is minable potash definition. .... 98



Figure TFIELD 6-12. Histograms of particle  $x$ -coordinates at exit point from LWB; full and partial-mining include all three replicates (note different vertical scales between plots; no mining contains 100 particles while mining scenarios include 300 particles) ..... 99

Figure TFIELD 6-13. Particle density in each cell for non-mining scenario. .... 100

Figure TFIELD 6-14. Magnitude of Darcy flux for r440 R2 for no, partial, and full-mining scenarios using cell-based coordinates; LWB (black) and SECOTP2D transport model domain (red) shown for reference..... 101

Figure TFIELD 6-15. Particle speeds for non-mining scenario computed from DTRKMF results 102

Figure TFIELD 6-16. Particle speeds for R1, computed from DTRKMF results ..... 103

Figure TFIELD 6-17. Particle speeds for R2, computed from DTRKMF results ..... 103

Figure TFIELD 6-18. Particle speeds for R3, computed from DTRKMF results ..... 104

Figure TFIELD 6-19. Mining factor and travel time to WIPP LWB for full-mining scenario (all replicates)..... 105

Figure TFIELD 6-20. Mining factor and travel time to WIPP LWB for partial-mining scenario (all replicates)..... 105

## List of Tables

Table TFIELD 4-1. $\beta$ -values for regression Equation TFIELD 4.1. ....	32
Table TFIELD 4-2. Listing of coordinates, depth and $\log_{10}$ transmissivity values used in regression model.....	34
Table TFIELD 4-3. Listing of coordinates, depth and $\log_{10}$ transmissivity values used in regression model.....	34
Table TFIELD 4-4. Variogram parameters for isotropic fit to indicator data variogram. Omnidirectional variogram calculated with a lag spacing of 500 m. ....	42
Table TFIELD 4-5. Correlation of $\beta$ and $I$ values from Equation TFIELD 4.1 to the $a$ and $b$ values in Equation TFIELD 4.3. ....	46
Table TFIELD 5-1. Steady-state freshwater head observations used as calibration targets.....	52
Table TFIELD 5-2. Summary of transient observations used as calibration targets .....	53
Table TFIELD 5-3. Initial values of parameters at pilot points. See.....	64
Table TFIELD 5-4. Parameters for T model variogram, fitted to transmissivity data using an omnidirectional variogram with lag spacing of 1,500 m. ....	66
Table TFIELD 5-5. Cutoff values for final field selection. ....	71
Table TFIELD 5-6. Final selected field identifiers.....	72
Table TFIELD 5-7. Bulk $\log_{10}$ transmissivity values comparison. ....	74
Table TFIELD 6-1. Particle tracking travel time statistics (years); PABC-2004 statistics from Table 3.22 of Lowry and Kanney (2005).....	95

## **TFIELD-1      Overview of the T-Field Development, Calibration, and Modification Process**

Modeling the transport of radionuclides through the Culebra Dolomite Member of the Rustler Formation is one component of the Performance Assessment (PA) performed for the Waste Isolation Pilot Plant (WIPP) 2009 Compliance Recertification Application (CRA) and PA Baseline Calculation (PABC). This transport modeling requires a model of groundwater flow through the Culebra. This Attachment describes the process used to develop and calibrate the model parameter fields for the Culebra. Calibrated model parameters are referred to broadly as “T-fields”, although more than transmissivity is being calibrated as part of the 2009 PA model. The T-fields are modified for the possible effects of potash mining for use in flow modeling for the CRA-2009 PABC.

The work described in this attachment was performed under two Sandia National Laboratories Analysis Plans (APs): AP-114 (Beauheim, 2008) and AP-144 (Kuhlman, 2009). AP-114 (Analysis plan for the evaluation and recalibration of Culebra transmissivity fields) dealt with the development and calibration of the T-fields (here including transmissivity (T), storativity (S), horizontal anisotropy (A), and vertical recharge (R)), in addition to the development of T-field acceptance criteria. AP-144 (Analysis plan for the calculation of Culebra flow and transport for CRA2009PABC) dealt with the modification of T fields for the potential effects of potash mining and radionuclide-transport calculations. The transport calculations are not described herein.

The starting point in the T-field development process was to assemble and update information on geologic factors that might affect Culebra T (Section TFIELD-2). These factors include dissolution of the upper Salado Formation below the Culebra, the thickness of overburden above the Culebra, and the spatial distribution of halite in the Rustler Formation both above and below the Culebra. Geologic information is available from hundreds of oil and gas wells and potash exploration holes in the vicinity of the WIPP site, while T values are available from only 64 well locations. Details of the geologic data compilation are given in (Powers, 2002; 2003), updated in (Powers, 2007a; 2007b) and summarized below in Section TFIELD-2.

A two-part “geologically based” approach was then used to generate Culebra base T-fields. In the first part (Section TFIELD-3), a conceptual model for geologic controls on Culebra T was formalized, and the hypothesized geologic controls were regressed against Culebra T data at monitoring wells to determine linear regression coefficients. The regression includes one continuously varying function, Culebra overburden thickness, and three indicator functions that assume values of 0 or 1 depending on the occurrence of open, interconnected fractures, Salado dissolution, and the presence or absence of halite in units bounding the Culebra.

In the second part (Section TFIELD-4), a method was developed for applying the linear regression model to predict Culebra T across the WIPP area. The regression model was combined with the maps of geologic factors to create 1,000 stochastically varying Culebra base T-fields. Details about the development of the regression model and the creation of the base T-fields are given in (Hart et al., 2008).

Several types of “soft data” were used to additionally constrain the stochastic simulation, including halite in the Rustler, the presence of gypsum cements in the Rustler, and diffusivity values obtained from hydraulic tests. The indicator kriging process for including soft data is detailed in (Hart et al., 2008) and summarized here in Section TFIELD-4.2.

Section TFIELD-5 of this attachment presents details on the modeling approach used to calibrate the T-fields to both steady-state heads and transient drawdown measurements. Heads measured in 42 observation wells around May 2007 were used to represent steady-state conditions in the Culebra, and drawdown responses in 67 total observation wells (62 unique locations) across nine pumping tests were used to provide transient calibration data. Details on the steady-state heads are described in (Johnson, 2009), and the transient drawdown data are summarized in (Hart et al., 2009). Assumptions made in modeling, the definition of an initial head distribution, assignment of boundary conditions, discretization of the spatial and temporal domain, weighting of the observations, and the use of PEST in combination with MODFLOW-2000 to calibrate the T-fields using a pilot-point method are described in detail in (Hart et al., 2009) and summarized in Section TFIELD-5 of this attachment. Section TFIELD-5.3.4 addresses the development and application of acceptance criteria for the T-fields. Acceptance was based on a combination of objective fit independently to both the steady-state and transient pumping test calibration data. Of the 200 fields calibrated, the 100 best were chosen using this metric. Section TFIELD-5.4 provides summary statistics and other information for the 100 T-fields that were judged to be acceptably calibrated.

Section TFIELD-6 of this attachment discusses the modification of the T-fields to account for the effects of potash mining both within and outside the WIPP land withdrawal boundary. Mining-affected areas were delineated, random transmissivity multipliers were applied to the transmissivity field in those areas, and particle tracks and travel times were determined (Kuhlman, 2010). The flow fields produced by these mining-affected T-fields are input to SECOTP2D for the CRA-2009 PABC radionuclide-transport calculations. Section TFIELD-7 provides an executive summary of the development of T-fields.

## TFIELD-2 Geologic Data

The work outlined in section TFIELD-2 was performed under AP-114, Analysis Plan for Evaluation and Recalibration of Culebra Transmissivity Fields (Beauheim, 2004). Geologic data were updated as part of the process of creating new T-fields. Geologic boundaries were refined using newly available field and log data (TFIELD-2.1). The confinement of the Culebra in the southeastern portion of Nash draw was also investigated (TFIELD-2.2).

### TFIELD-2.1 Refine Geologic Boundaries

The locations of the Rustler halite margins (TFIELD-2.1.1) and the Salado dissolution margin (TFIELD-2.1.2) both affect the conceptual model of transmissivity in the Culebra (see Figure TFIELD 2-1 for general relationships between Rustler, Salado and the WIPP repository). These were updated as part of the current geologic study.

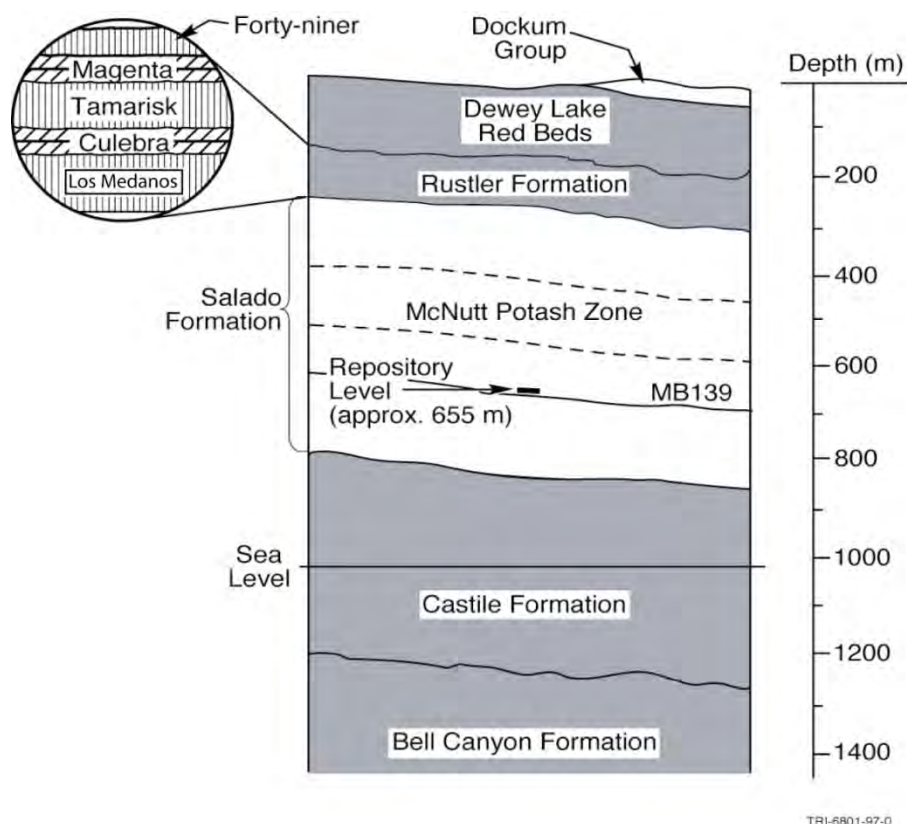
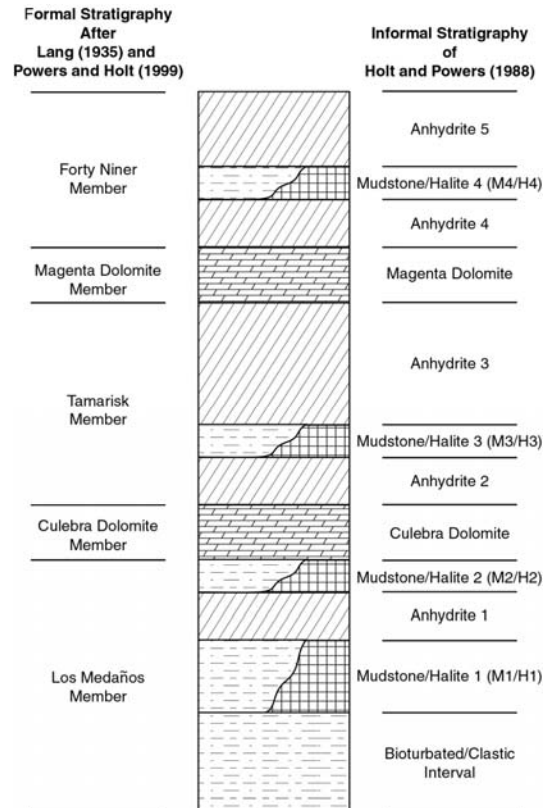


Figure TFIELD 2-1. Generalized stratigraphy near WIPP

#### TFIELD-2.1.1 Rustler Halite Margins

The Rustler Formation stratigraphic column given in Figure TFIELD 2-2 shows two types of geologic variability. Vertical stratigraphy places older formations below younger formations at the same location in space (e.g., the Los Medaños Member is older than Culebra Member), while facies changes place two units of similar age at different spatial locations, due to changes in depositional

environments (e.g., Mudstone 4 (M4) and Halite 4 (H4) of the Forty-niner Member are of the same age, but occur in different locations).



**Figure TFIELD 2-2. Stratigraphic nomenclature of the Rustler Formation.**

The presence of halite in the non-dolomite members of the Rustler Formation is an important factor in the transmissivity of the Culebra dolomite. When halite exists both above (M3/H3) and below (M2/H2) the Culebra, hydraulic transmissivities in the Culebra are very low.

Powers (2002) provided geologic data from the Culebra modeling domain that included maps of the margins of halite within the Rustler Formation. Those margins were largely based on work in Powers and Holt (1995), modified by some data collected from potash drillholes, especially in the northern area of the Culebra modeling domain. The margins provided by Powers (2002) have been published elsewhere in simpler forms (Powers et al., 2003; Holt et al., 2005). The observed distribution of halite in the Rustler is interpreted as the result of sedimentary structures and facies relationships controlled by deposition, rather than the result of dissolution alone (Holt and Powers, 1988; Powers and Holt, 1999; Powers and Holt, 2000). Some minor zones adjacent to the depositional margins have been interpreted as having undergone some post-depositional dissolution of halite, specifically the halite in the Tamarisk Member (Beauheim and Holt, 1990).

Significant changes to the locations of the M3/H3 and M2/H2 margins have been made in some areas since CRA-2004 as part of Task 1A of AP-114. As such, the Rustler halite margins shown in Figure TFIELD 2-1 are as defined in Powers (2007a; 2007b).

Both wells (H-17 and H-12) located where halite occurs in the Tamarisk Member (M3/H3 interval; Figure TFIELD 2-5) but not in the Los Medaños Member (M2/H2 interval; Figure TFIELD 2-4) of the Rustler Formation show low transmissivity. We assume that high-transmissivity zones do not occur in regions where halite is present in the M2/H2 or M3/H3 intervals. Margins near WIPP remain nearly unchanged, and all modifications to the margins do not change the basic interpretation that the margins are the result of deposition and local syndepositional dissolution of halite (Holt and Powers, 1988; Powers and Holt, 2000; Powers et al., 2006). Core evidence from well SNL-8 shows limited brecciation of A3 that is interpreted as an extension of a narrow margin along the H-3 margin where a limited amount of halite was dissolved after deposition.

One result of refining the Rustler halite margins is that all mudstone/halite margins now show similar gross trends (Figure TFIELD 2-7). Southeast of WIPP, halite thickens and the margins resemble the outline of a depocenter that is elongate roughly northwest to southeast. The gross trends of these margins are similar to the trend in the elevation of the top of Culebra (Figure TFIELD 2-8). As previously described (e.g., (Holt and Powers, 1988; Powers et al., 2003)), this anticlinal feature was called the “Divide anticline”. Mudstone dominates along this trend in three of the mudstone-halite units of the Rustler, and the evidence presented for depositional facies rather than dissolution leads to the proposition that halite facies were deposited in mini-basins formed by nascent salt withdrawal in underlying formations and halite migration into the anticline.

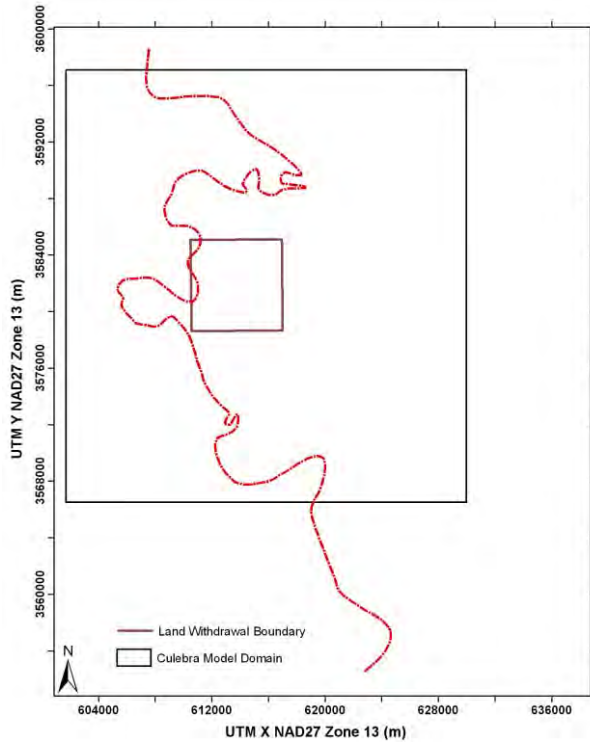


Figure TFIELD 2-3. M-1/H-1 halite margin in the lower Los Medaños Member

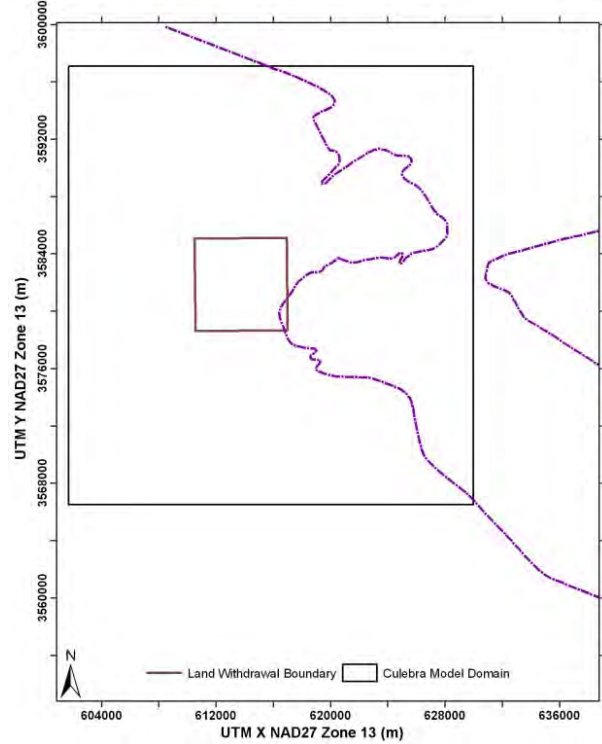


Figure TFIELD 2-4. M-2/H-2 halite margin in the upper Los Medaños Member

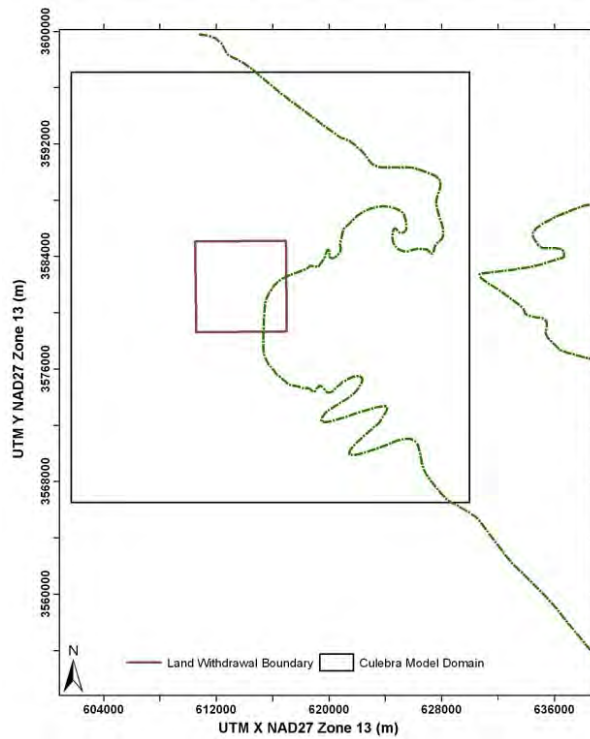


Figure TFIELD 2-5. M-3/H-3 halite margin in the Tamarisk Member

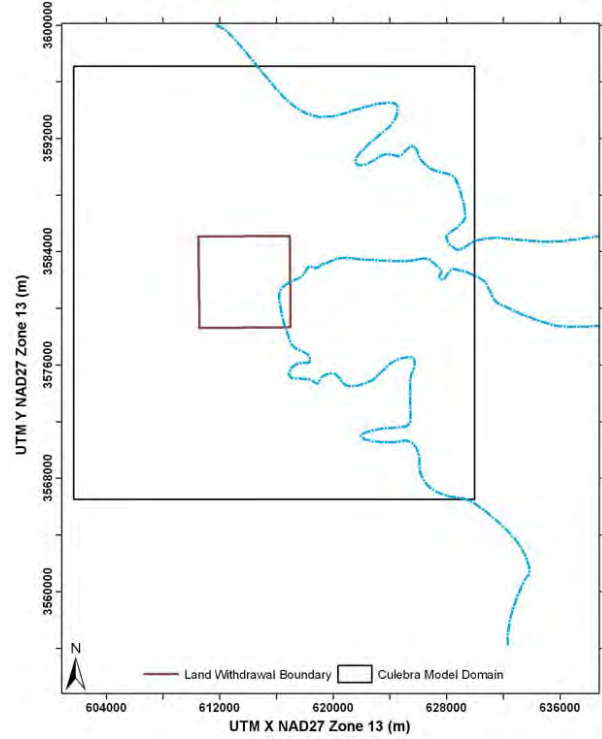


Figure TFIELD 2-6. M-4/H-4 halite margin in the Forty-niner Member



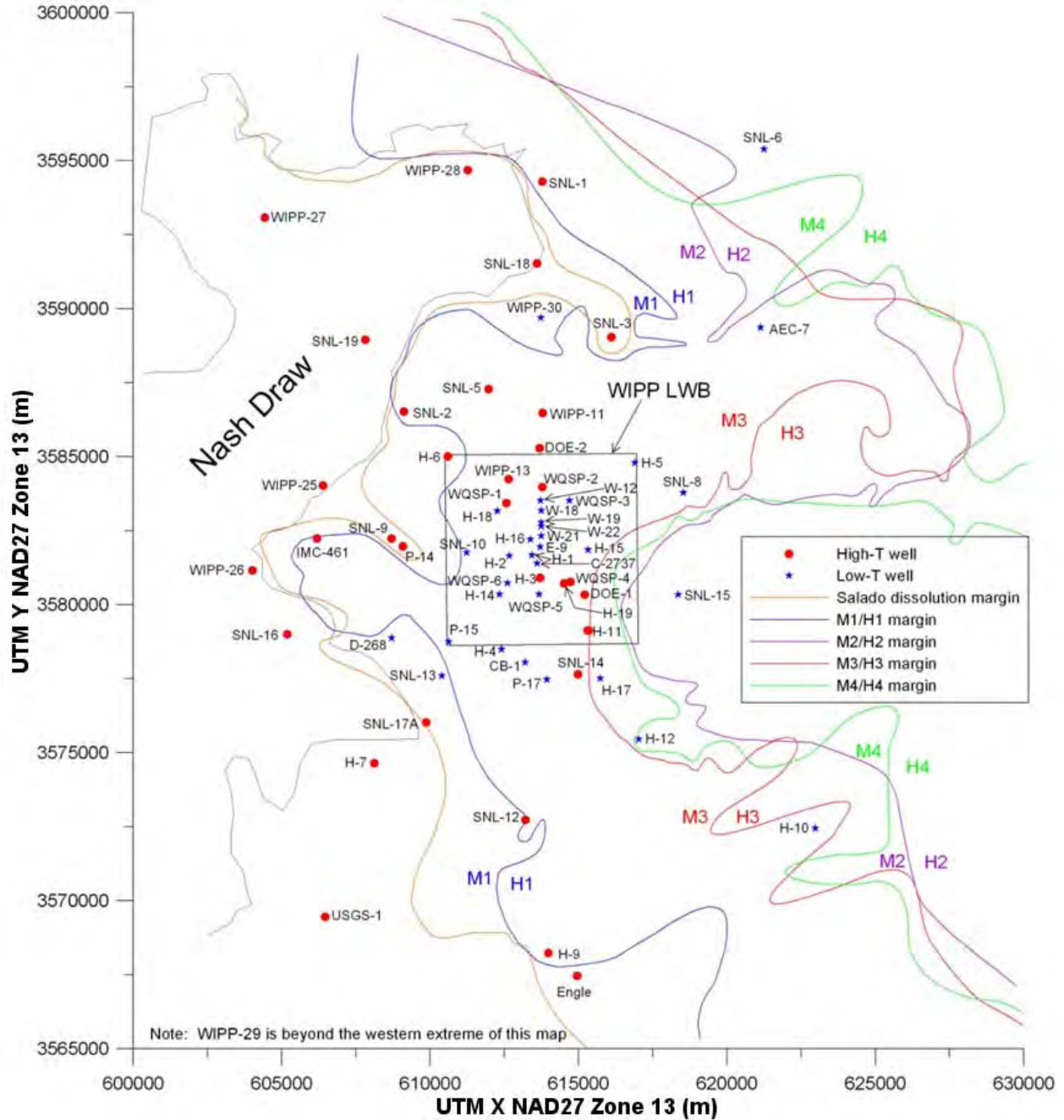


Figure TFIELD 2-7. Salado dissolution and Rustler mudstone/halite margins.

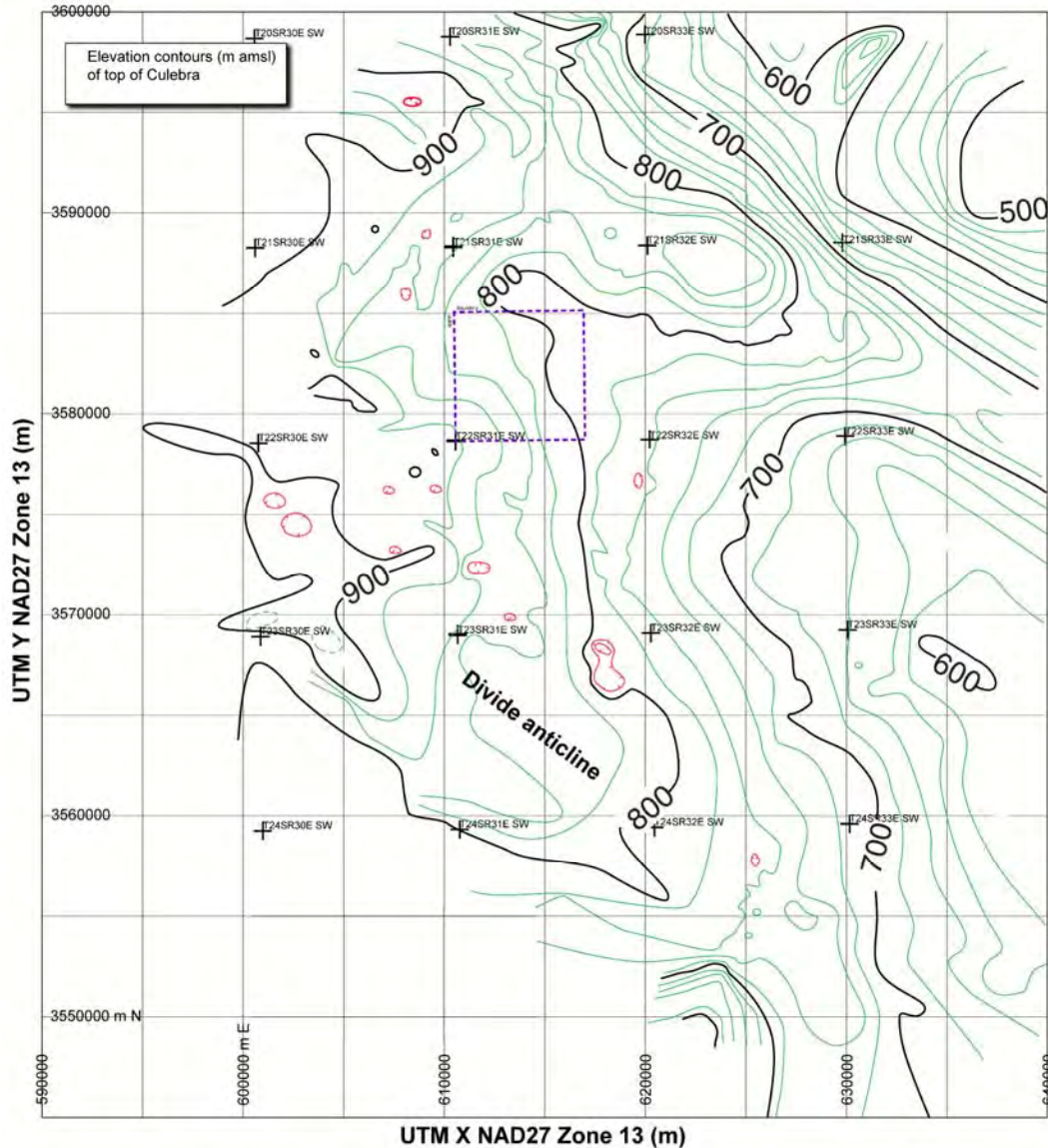


Figure TFIELD 2-8. Elevation (m above mean sea level) of top of Culebra member of Rustler Formation.

### TFIELD-2.1.2 Salado Dissolution

A margin for dissolution of upper Salado Formation halite was inferred based on significant local changes in thickness of the interval between the Culebra Dolomite and the Vaca Triste Sandstone Member of the Salado (Powers, 2002). The margin was modified somewhat to reflect other information that indicated embayments of the dissolution margin. Additional data were added south of the WIPP, with log cross-sections, to delineate the margin more accurately (Powers, 2003). Some of these data are reflected in simplified maps included in (Powers et al., 2003) and (Holt et al., 2005).

South and west of the WIPP site, Cenozoic dissolution has affected the upper Salado Formation. Where this dissolution has occurred, the rocks overlying the Salado, including the Culebra, are

strained (leading to larger apertures in existing fractures), fractured, collapsed, and brecciated (e.g., (Beauheim and Holt, 1990)). All WIPP Culebra wells within the dissolution zone fall within the high-transmissivity population, and we hypothesize that all regions affected by Salado dissolution have well-interconnected fractures and high transmissivity in the Culebra.

The Salado dissolution margin has been updated (see Appendix G from the Analysis Report for Task 5 of AP-114 (Hart et al., 2008)) based on reinterpretation of borehole logs in the vicinity of H-9. This analysis has, specifically, placed H-9 east of the dissolution line, where previously it was considered to be within the area affected by Salado dissolution. The Salado dissolution margin, reflecting the change near H-9, is shown with the Rustler halite margins in Figure TFIELD 2-7.

## ***TFIELD-2.2      Confinement and Recharge in the Culebra***

Field and mapping studies were performed to identify potential recharge locations south and west of WIPP in the southeastern arm of Nash Draw (Powers, 2006). This work also identified unconfined areas in the Culebra in the same area. The boundaries to the west and south correspond to the limits used for earlier modeling – see Figure 2 of Beauheim (2004); the northern and eastern boundaries included the southeastern arm of Nash Draw and an area beyond the apparent eastern extent of the draw.

Five “elements” were identified that contribute to understanding recharge and that can be useful for modeling the possible effects of recharge to the Culebra in the study area. These elements are:

1. surface drainage basins,
2. an estimate of areas with differing confinement of the Culebra,
3. the location and character of drainage channels within drainage basins,
4. the location of specific points of recharge (e.g., sinkholes), and
5. estimating the relationship between soil characteristics and rainfall infiltration across the study area (i.e., curve number).

Of these elements, the estimate of Culebra confinement is the most interpretive. Drainage basins, channels and specific points of recharge are identified using surface topography features identifiable from maps, aerial photos, or field reconnaissance. Existing maps of soils, combined with surface reconnaissance and aerial photographs, permit relatively direct assignment of soil properties controlling runoff. The degree of confinement of the Culebra in the study area, however, is not directly determinable from the surface data. As a result, a variety of surface features and well data are combined for an estimate of the areas where the Culebra is relatively less confined than it is at the WIPP site, where well test and drillhole data are more readily available.

### ***TFIELD-2.2.1      Surface Drainage Basins***

Drainage basin size and characteristics are important elements in determining how rainfall, infiltration, and runoff may contribute to recharge of the Culebra and other near-surface hydrologic units. Topographic maps, aerial photographs, and some field checking were used to define separate surface drainage basins.

The drainage basins are mainly separated by topographic divides and local lows or concentration points that can be distinguished on the standard 7.5-minute quadrangle maps supplemented by study of aerial photographs. Because this is an area of evaporite karst (e.g., (Powers and Owsley, 2003)), collapse features, caves, or sinkholes may capture local drainage in smaller basins or subbasins (wholly enclosed by another basin). An example is drainage basin #7 (Figure TFIELD 2-9), which is wholly enclosed in drainage basin #6. These very localized closed drainage basins in Nash Draw represent potential recharge locations for the Rustler Formation. Mapping the basins is the first step in understanding the complex geology and hydrology inside Nash Draw, which expresses itself as water level fluctuations in some Culebra wells near Nash Draw(Hillesheim et al., 2007).

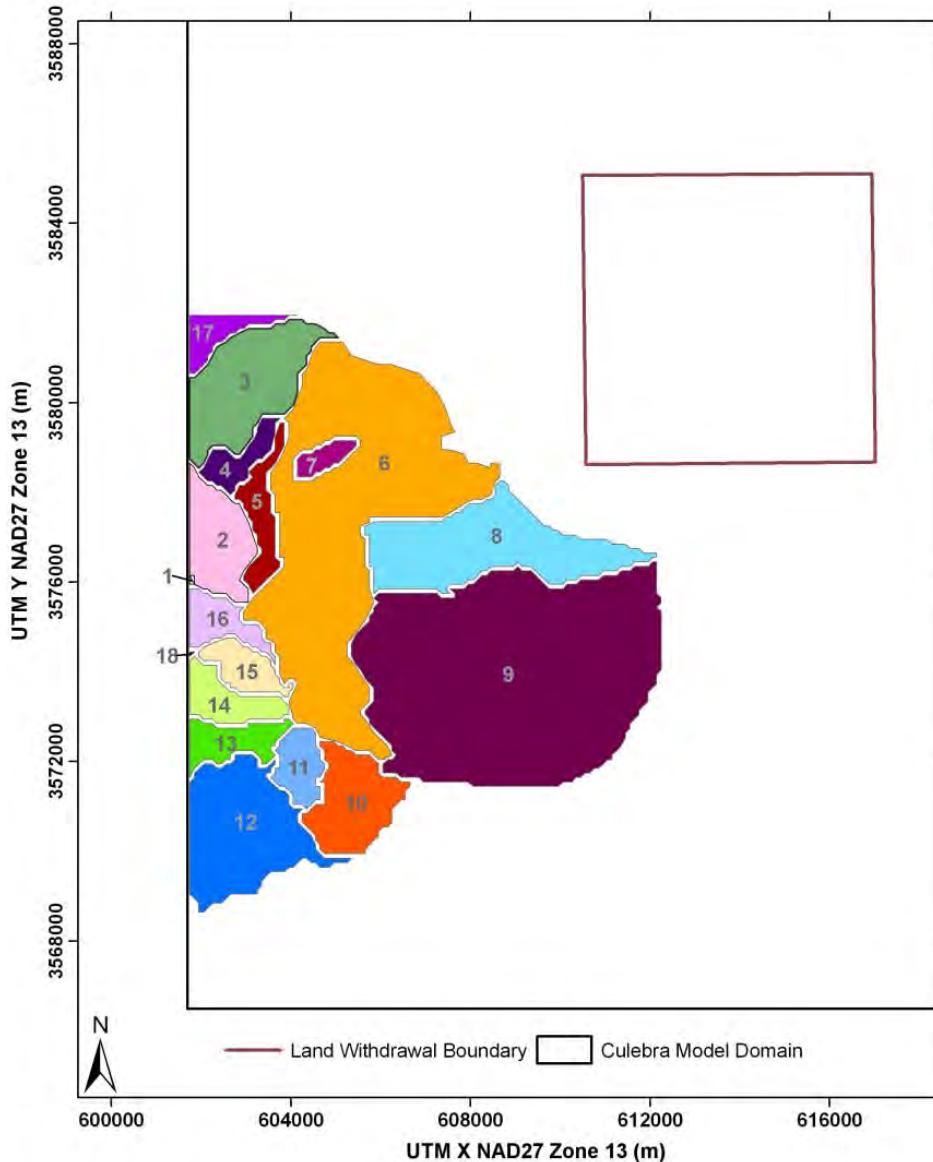


Figure TFIELD 2-9. Closed drainage sub-basins identified in southern Nash Draw; white areas either outside Nash Draw or outside the study area.

### TFIELD-2.2.2 Culebra Confinement

The Culebra can be considered confined with little potential for direct vertical recharge for the relatively short time period covered in model calibration the Culebra at the WIPP site (the length of multi-well pumping tests). Within portions of Nash Draw, it is clear that the Culebra is not significantly confined because water levels respond to surface events in a very short time (Hillesheim et al., 2007). It is unlikely that a completely defined boundary exists between areas where the Culebra is confined and where it is unconfined. In developing the Culebra T-fields, three zones have been identified, corresponding to the notion that there are areas where the Culebra is confined, areas where it is unconfined, and areas that represent a transition zone. The “confined”

area has a relatively unambiguous definition, whereas the boundary between “transition” and “unconfined” is much more subjective.

The area of the Culebra considered “confined” (white in Figure TFIELD 2-10) is defined approximately by the interpreted margin of upper Salado halite dissolution (Powers et al., 2003). There is a significant increase in Culebra transmissivity (T) values west and south of this margin, and this change is attributed to changes in fracture aperture associated with strain induced by dissolution. The “transition” zone (Figure TFIELD 2-10) includes areas where some data from wells indicate there is some vertical isolation of the Culebra, but the time constant is not known.

Most of the “unconfined” zone (Figure TFIELD 2-10) in the Culebra is within the more central portions of Nash Draw and out of the study area. The strategy for estimating relative Culebra confinement was to select areas where the Culebra is known or believed to be very shallow (~ 30 m or less) and where observed recharge points (caves, sinkholes, alluvial dolines) are believed to access units below the Magenta. Some large caves and sinkholes are developed in the Tamarisk gypsum beds and have a greater likelihood of providing hydraulic connection to the Culebra than similar openings in the Forty-niner gypsum beds. Many potash exploration holes within Nash Draw encountered lost-circulation zones, but the stratigraphic relationships of these zones to the Culebra are not overly constrained. Thus, there is a general sense of factors away from Livingston Ridge (the escarpment marking the eastern edge of the surface expression of Nash Draw) and the upper Salado dissolution margin that contribute to greater vertical permeability above the Culebra, but these factors are generally qualitative.

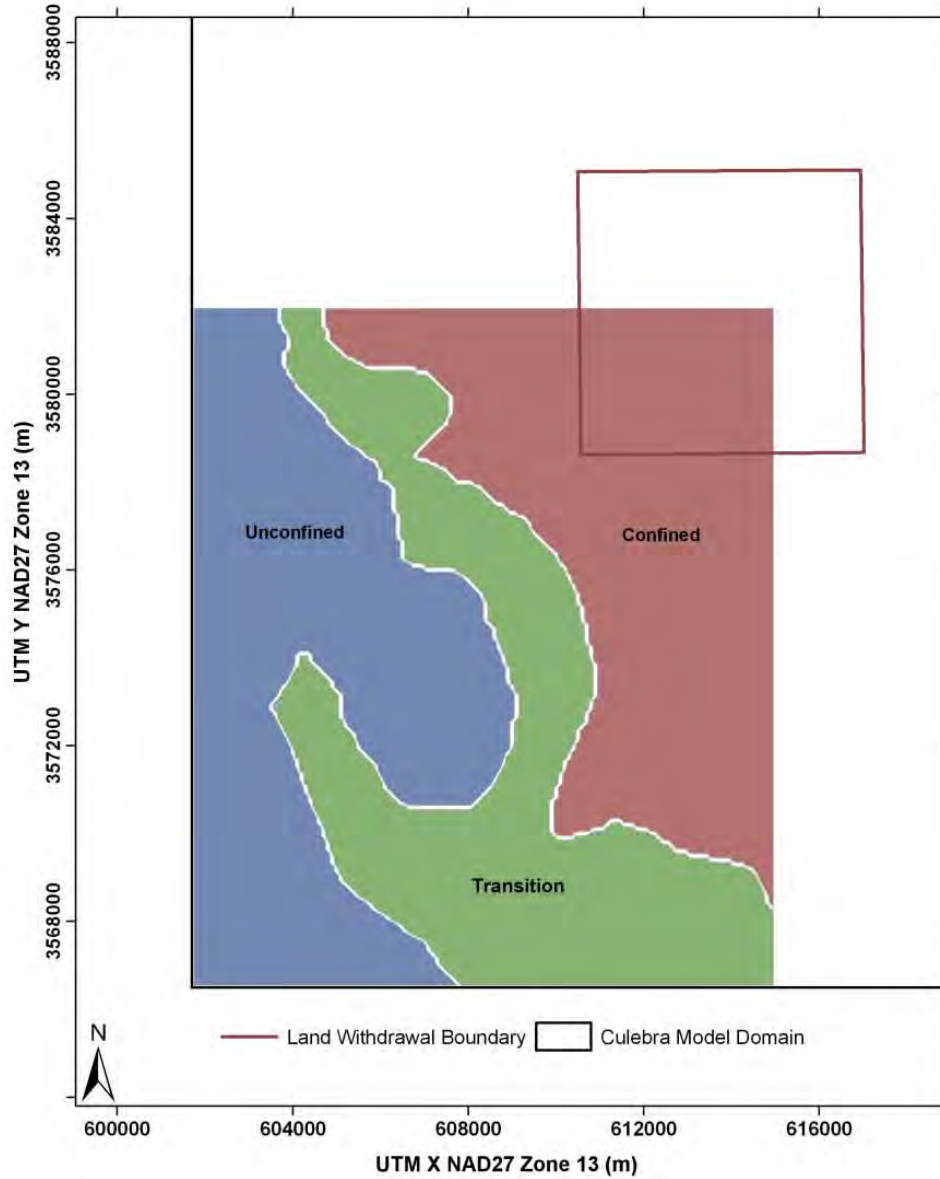
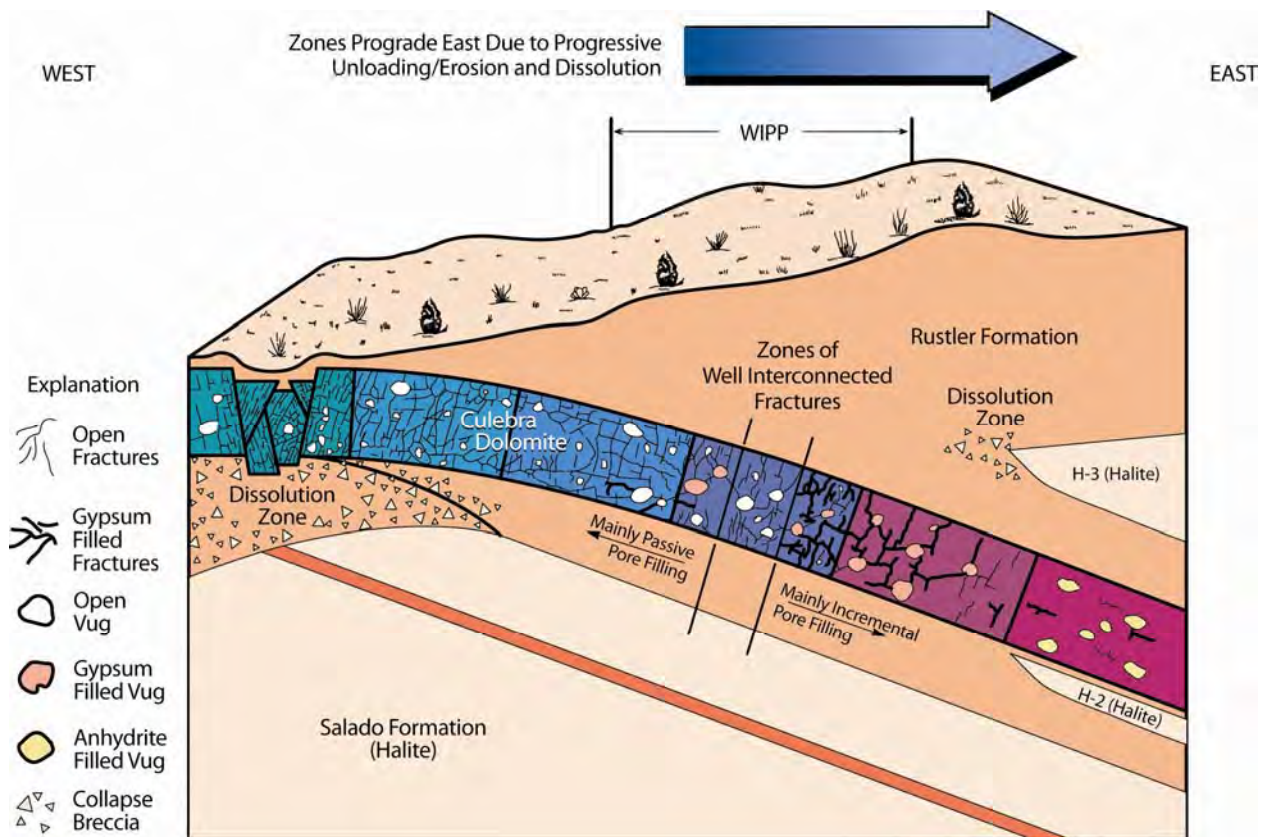


Figure TFIELD 2-10. Culebra confinement map for southern Nash Draw study area; white areas outside study area

## TFIELD-3 T-Field Conceptual Model

The work outlined in section TFIELD-3 was performed under AP-114, Analysis Plan for Evaluation and Recalibration of Culebra Transmissivity Fields (Beauheim, 2004). The conceptual model for base field creation was originally explained in Holt and Yarbrough (2002), as Subtask 1 of Task 2 of AP-088. While the data used have been updated and improved, the model itself has changed very little. Any deviations from the original model due to updates in data or process are discussed in the text below.

A conceptual model of the geology of the Culebra dolomite located in the area of the WIPP site is shown in Figure TFIELD 3-1. Geologic controls on Culebra transmissivity are identified and a linear mathematical model relating these controls to transmissivity is constructed. The geology and geologic history of the Culebra has been described in the literature (Holt and Powers, 1988; Beauheim and Holt, 1990; Holt, 1997). The following conceptual model is developed from this published work and is consistent with the interpretations presented therein. Specifically, we follow Holt (1997) and assume that variability in Culebra transmissivity is due strictly to post-depositional processes. Throughout the following discussion, the informal stratigraphic subdivisions of Holt and Powers (1988) are used to identify geologic units within the Rustler Formation, as listed in Figure TFIELD 2-2.



**Figure TFIELD 3-1. Culebra Dolomite conceptual model near WIPP. Culebra T values decrease to the east (increasing overburden and halite), and fracturing increases to the west (Salado dissolution zone). Halite appears both above (H-3) and below (H-2) the Culebra in the east.**



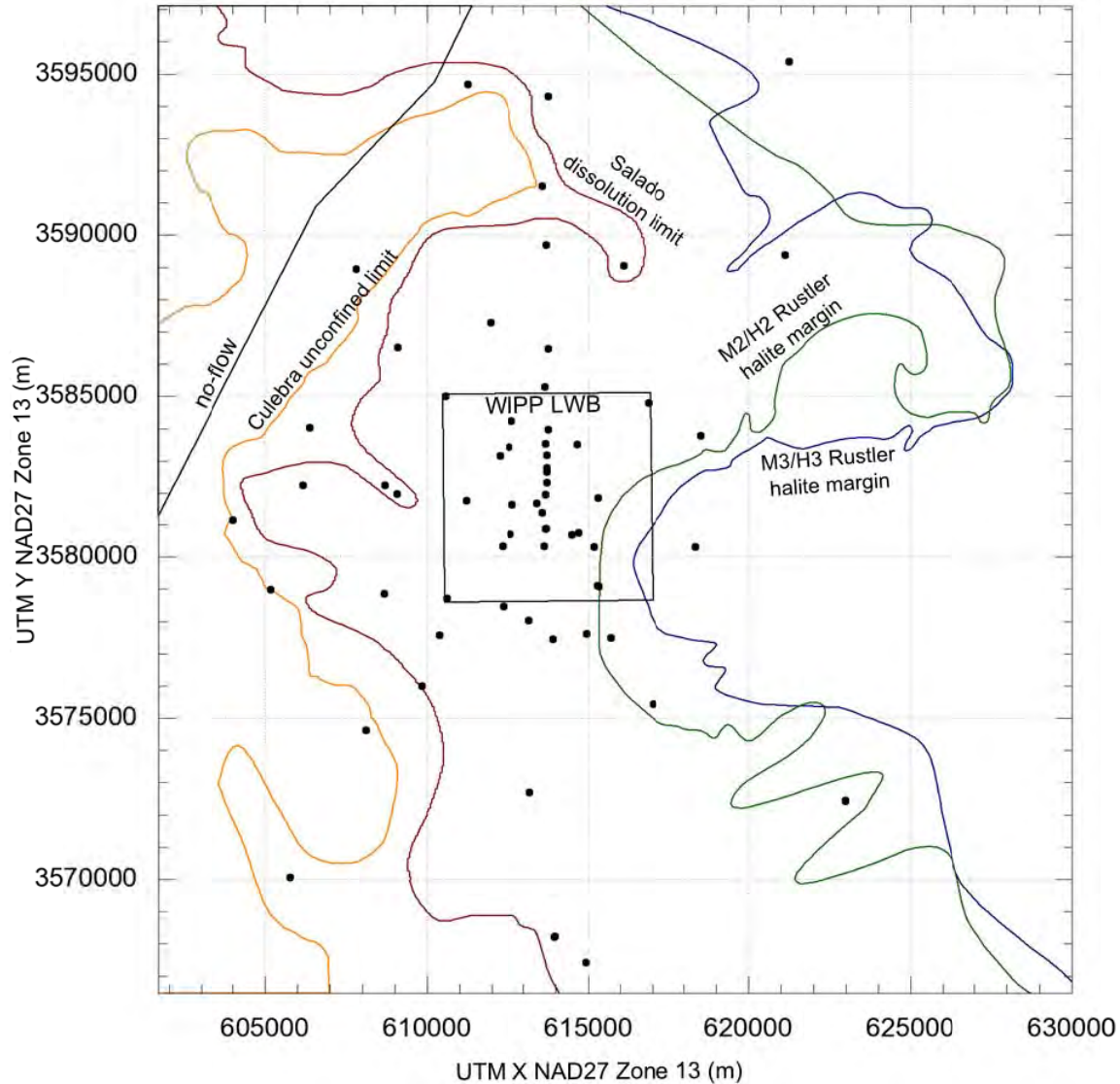


Figure TFIELD 3-2. The model domain with margins and wells.

We hypothesize that spatial distribution of Culebra transmissivity is a function of several geologic factors that can be determined at any location using geological map data, including:

1. Culebra overburden thickness,
2. fracture interconnection,
3. dissolution of the upper Salado Formation below the Culebra, and
4. occurrence of halite in units above or below the Culebra.

High-T regions near the WIPP cannot be predicted using geologic data, as they represent areally persistent zones of well-interconnected fractures, and fracture interconnection cannot be observed

or inferred from core or geophysical log data. We therefore treat fracture interconnection as a stochastic process.

### ***TFIELD-3.1 Model Domain***

The model domain has been expanded to the east relative to the domain used for the 2004 Compliance Recertification Application (CRA-2004; (U.S. DOE, 2004)) in order to reach an area where halite is present in all of the non-dolomite members of the Rustler Formation. This change was made in order to simplify the specification of the eastern boundary condition of the model. The new extent of the model domain is 601,700 UTM NAD27 east to 630,000 UTM NAD27 east and 3,566,500 UTM NAD27 north to 3,597,100 UTM NAD27 north. The domain is discretized into 100-m square cells, yielding a model that is 284 cells wide by 307 cells tall. The Culebra is modeled as a single layer that is of uniform 7.75-m thickness (U.S. DOE, 1996). Figure TFIELD 2-7 shows the model domain with the WIPP site boundary and the various Culebra monitoring wells.

### ***TFIELD-3.2 Overburden Thickness***

We hypothesize an inverse relationship between Culebra overburden thickness and Culebra transmissivity. Overburden thickness is a metric for two different controls on Culebra transmissivity. First, fracture apertures are limited by overburden thickness (e.g., (Currie and Nwachukwu, 1974)), which should lead to lower transmissivity where Culebra depths are greater (Beauheim and Holt, 1990; Holt, 1997). Second, erosion of overburden leads to stress-relief fractures, and the amount of Culebra fracturing increases as the overburden thickness decreases (Holt, 1997). Contours of Culebra overburden thickness are given in Figure TFIELD 3-3; the depth to the Culebra is defined as  $d(x, y)$  for all points in the domain.

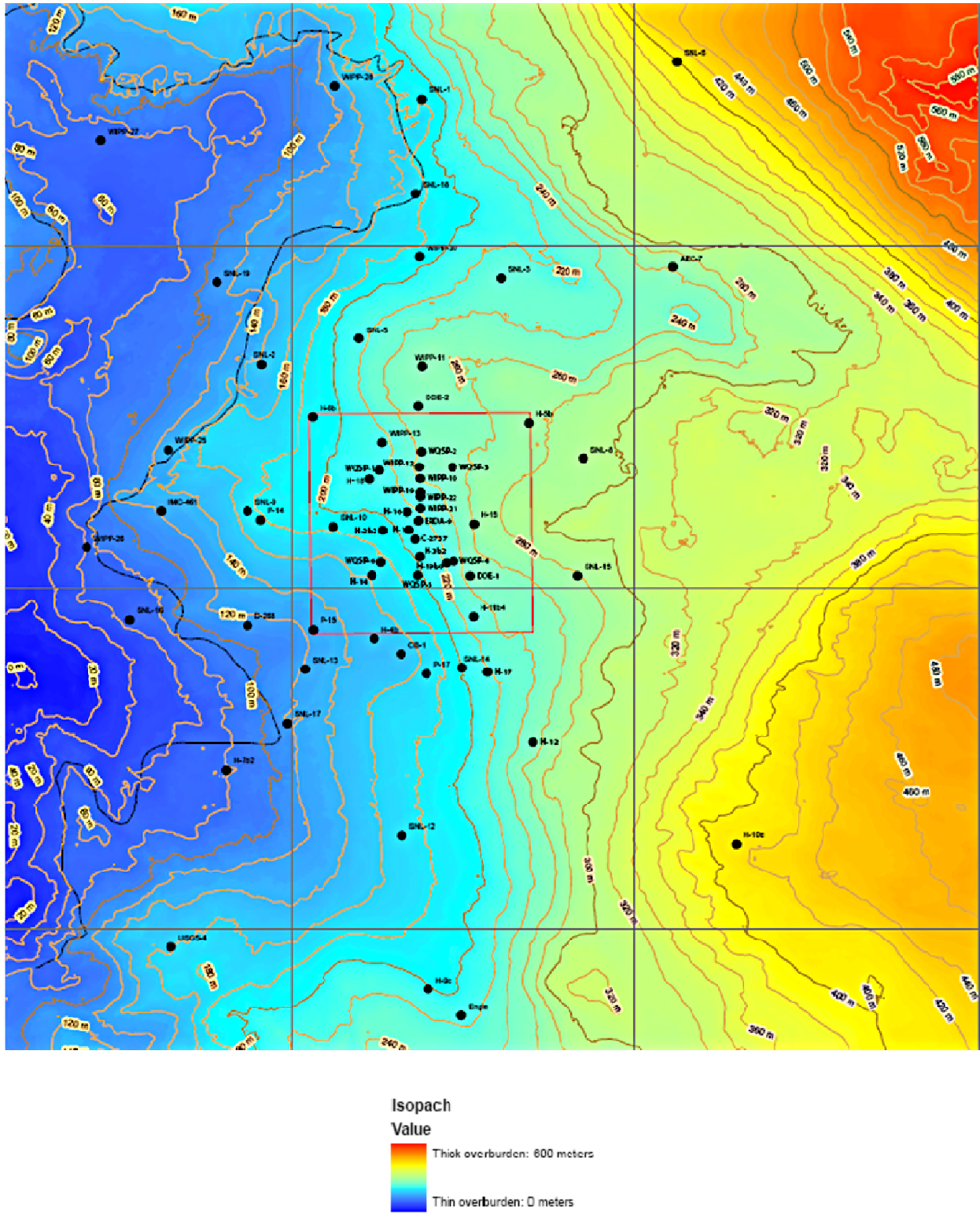


Figure TFIELD 3-3. Thickness of Culebra overburden.

### TFIELD-3.3 Fracture Interconnection

The Culebra transmissivity data used in the modeling are the same as those used by Holt and Yarbrough (2002), supplemented by more recent data reported from recent pumping tests (Roberts, 2006; Roberts, 2007; Bowman and Roberts, 2008). The log transmissivity data show a bimodal distribution in Figure TFIELD 3-4. As closely spaced wells can show very different values, we hypothesize that higher transmissivity values reflect the presence of well-interconnected fractures that are absent at lower transmissivity locations. For example, wells WQSP-2 and WIPP-12 are only 454 m apart, but have T values differing by over two orders of magnitude. Thus, the fractures present at WQSP-2 apparently do not extend to WIPP-12. Well-interconnected fractures occur in regions affected by Salado dissolution (e.g., Nash Draw) and in areas with complicated cement dissolution and precipitation histories (e.g., high-transmissivity zones near the WIPP site). The natural break between the measured  $\log_{10} T$  ( $m^2/s$ ) values at  $-5.4$  described by Holt and Yarbrough (2002) is illustrated with a vertical black line in Figure TFIELD 3-4. The fracture-interconnection indicator,  $I_f$ , is defined as

$$I_f = \begin{cases} 1, & \log_{10} T (m^2/s) \geq -5.4 \\ 0, & \log_{10} T (m^2/s) < -5.4 \end{cases} \quad (\text{TFIELD 3.1})$$

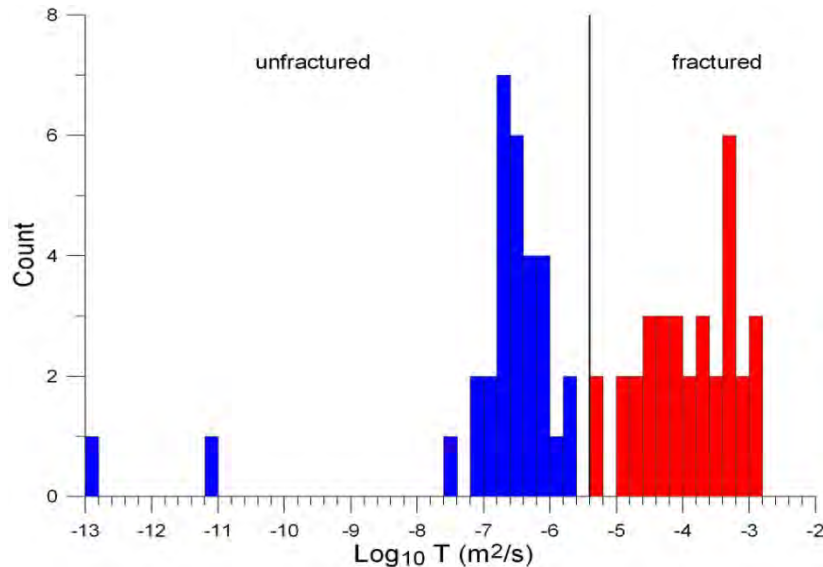


Figure TFIELD 3-4. Histogram of  $\log_{10}$  Culebra transmissivity.

### TFIELD-3.4 Salado Dissolution

Slight modification was made to the Salado dissolution margin, as outlined in Section TFIELD-2.1.2. The indicator variable for Salado dissolution is  $I_D$ , and is defined to be 1 in areas of the model domain where dissolution has occurred, and 0 otherwise. The Salado dissolution margin is plotted with the Rustler halite margins in Figure TFIELD 2-7.

### **TFIELD-3.5      *Rustler Halite Margins***

The M2/H2 and M3/H3 Rustler halite margins were modified as outlined in Section TFIELD-2.1.1; the margins are shown individually in Figure TFIELD 2-4 and Figure TFIELD 2-5, and together with the M1/H1 and M4/H4 Rustler halite margins and Salado dissolution margin in Figure TFIELD 2-7.

Wells SNL-6 and SNL-15 are new wells drilled since Holt and Yarbrough (2002), and are located east of the M2/H2 and M3/H3 halite margins, where halite is present in both intervals (see Figure TFIELD 2-2). As predicted by Holt (1997), the Culebra itself was partially cemented with halite at these locations, and measured transmissivities were extremely low (Roberts, 2007; Bowman and Roberts, 2008). Due to these new observations, we assume that transmissivity in the region where halite occurs both above (in the M3/H3 interval) and below (in the M2/H2 interval) the Culebra is lower than where halite occurs in only one interval. The indicator term  $I_H$  is defined to be 1 at any point where halite is present in both the M2/H2 and M3/H3 margins and to be 0 elsewhere.

### **TFIELD-3.6      *High-Transmissivity Zones***

High-transmissivity zones within the Culebra can occur between areas bounded on the west by the Salado dissolution margin and bounded on the east by halite present in the M2/H2 and/or M3/H3 intervals (the central zone in Figure TFIELD 3-5). In these zones, fractures are well-interconnected, and fracture interconnectivity is controlled by a complicated history of fracturing with several episodes of cement precipitation and dissolution (Beauheim and Holt, 1990; Holt, 1997). Unfortunately, no geologic metric for fracture interconnectivity is identifiable in cores or from subsurface geophysical logs, and fracture interconnectivity can only be identified from *in situ* hydraulic test data.

Because of this lack of a geologic metric, we consider the spatial location of high-transmissivity zones to be a stochastic process that cannot be predicted deterministically. Instead, the spatial layout of these zones is created using geostatistical indicator kriging with conditioning data. This is a change from (Holt and Yarbrough, 2002), where the only conditioning information was based on the known T-values at wells. We have added information to the geostatistical model to increase the likelihood of high T being placed between two wells that hydraulic testing has shown to be quite connected. Likewise, areas where there is evidence of high levels of gypsum will be given a slightly lower probability of being in a high-T zone. This allows us to merge both hydraulic and geologic data in the creation of high-T zones, while still keeping zone placement and shape a stochastic process. Details regarding the soft data used are presented in Section TFIELD-4.2.

### **TFIELD-3.7      *Linear Transmissivity Model***

Using hypothesized geologic controls on Culebra transmissivity, we construct the following linear model for  $Y(x, y) = \log_{10} T(x, y)$

$$Y(x, y) = \begin{cases} \beta_1 + \beta_2 d(x, y) + \beta_3 + \beta_4 & \text{Salado Dissolution} & I_D = 1, I_f = 1, I_H = 0 \\ \beta_1 + \beta_2 d(x, y) + \beta_3 & \text{Central High-T} & I_D = 0, I_f = 1, I_H = 0 \\ \beta_1 + \beta_2 d(x, y) & \text{Central Low-T} & I_D = 0, I_f = 0, I_H = 0 \\ \beta_1 + \beta_2 d(x, y) & \text{M2/H2} \oplus \text{M3/H3} & I_D = 0, I_f = 0, I_H = 0 \\ \beta_1 + \beta_2 d(x, y) + \beta_5 & \text{M2/H2} \& \text{M3/H3} & I_D = 0, I_f = 0, I_H = 1 \end{cases} \quad (\text{TFIELD 3.2})$$

where  $\beta_{1...5}$  are regression coefficients, the two-dimensional location vector  $(x, y)$  consists of NAD27 UTM Zone 13  $x$  and  $y$  coordinates,  $d(x, y)$  is the overburden thickness,  $I_f$  is an indicator of whether fracturing is present in the Culebra,  $I_D$  is the Salado dissolution indicator, and  $I_H$  is the halite bounding indicator. In this model, regression coefficient  $\beta_1$  is the intercept value for the linear model. Coefficient  $\beta_2$  is the slope of  $Y(x, y)/d(x, y)$ . The coefficients  $\beta_3$ ,  $\beta_4$ , and  $\beta_5$  represent adjustments to the intercept for the occurrence of interconnected fractures, Salado dissolution, and halite bounding, respectively. Although other types of linear models could be developed, our model is consistent with our conceptual model relating transmissivity to geologic controls and can be tested using published WIPP geologic and transmissivity data.

Because there are only two data points for transmissivity in the zone where Culebra is bounded by halite, and both are significantly lower than any other transmissivity values in the model, we include the  $\beta_5 I_H$  term in Equation TFIELD 3.2 to take into account the very low T zone. This was done to keep the conceptual model consistent for all zones, recognizing that the base fields are primarily a starting point for following inverse calibration.

The combined results of the regression and the indicator kriging (presented in the next section) are 1,000 base transmissivity fields that share certain geologic features, but are all different. This difference is provided by the stochastic placement of high-T areas in the central zone. These areas are placed using the GSLIB Sequential Indicator Simulation (SISIM) routine. This routine uses geostatistical methods to create stochastic indicator (Boolean value) fields.

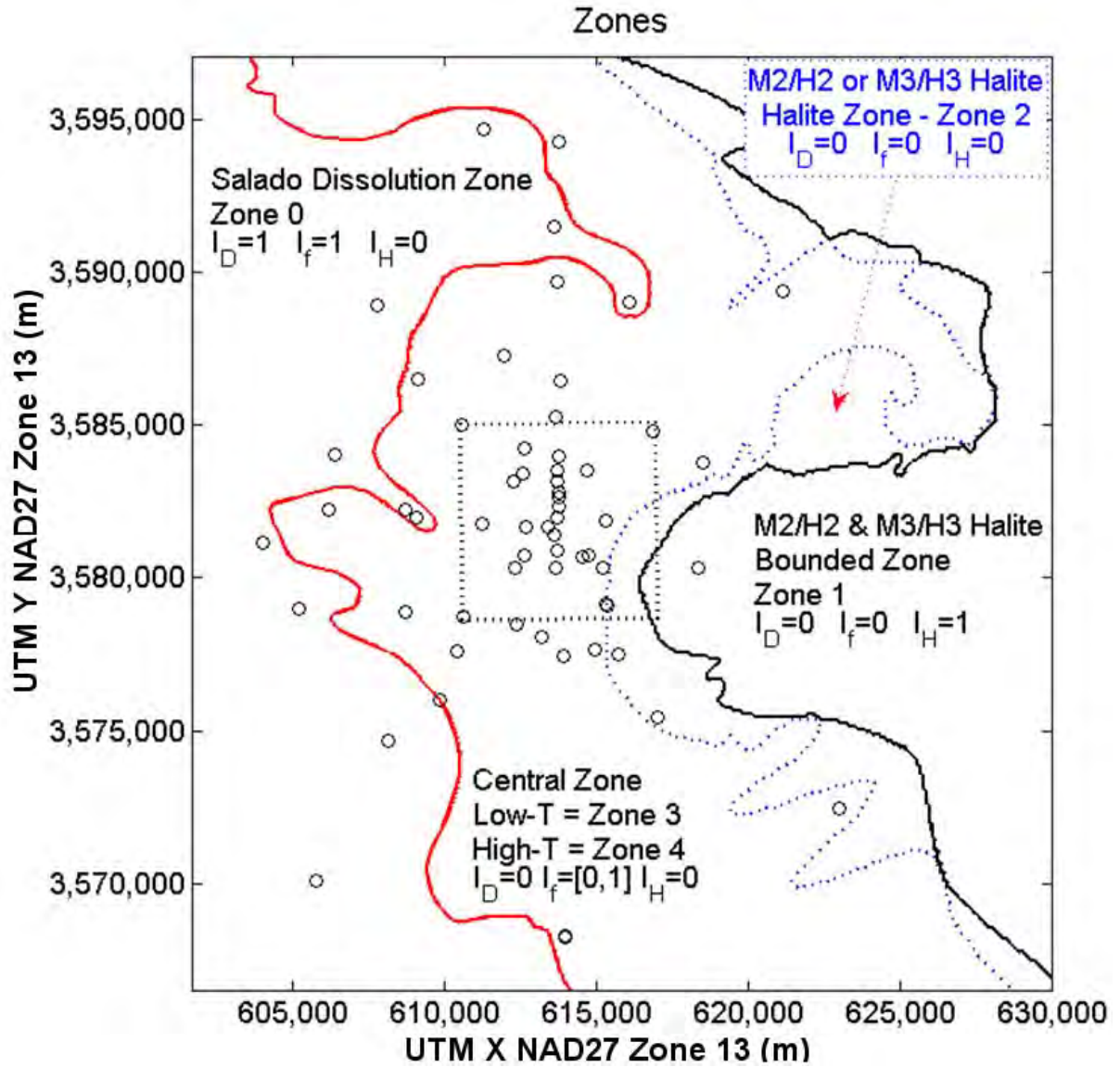


Figure TFIELD 3-5. Conceptual model zones with indicator values and zone numbers (Equation TFIELD 3.2).

## TFIELD-4 T-Field Construction Using Indicator Kriging

The work outlined in section TFIELD-4 was performed under AP-114, Analysis Plan for Evaluation and Recalibration of Culebra Transmissivity Fields (Beauheim, 2004). Indicator kriging is a specific form of the general kriging linear estimator where cutoffs, rather than values, are estimated. Here, stochastic simulation based on indicator kriging is used to predict where high and low transmissivity areas will be located, taking various constraints into account. The constraints include a linear regression relationship between  $\log_{10} T$  and Culebra overburden (see Section TFIELD-4.1) and geologic soft data such as the presence of halite in nearby units or gypsum cements in the Culebra (see Section TFIELD-4.2). The indicator variograms are constructed from these data (see Section TFIELD-4.3) and used to stochastically simulate the cutoff between high and low transmissivity in the Culebra (see Section TFIELD-4.4). The indicator kriging simulation result is then incorporated into the base T-fields (see Section TFIELD-4.5).

### TFIELD-4.1 Step 1 – Linear Regression Analysis

The best fit for the known transmissivity data is based on a multi-line regression. The wells are separated into three groups: wells in the Salado dissolution zone, wells with low-T pumping test results, and wells with high-T pumping test results. The graph displayed in Figure TFIELD 4-1 shows the  $\log_{10} T$  values from pumping test results along with the regression lines. The cutoff between low and high  $\log_{10} T$  is -5.4. Wells located where the Culebra is bounded above and below by halite (SNL-6 and SNL-15) are considered outliers and were not included in the regression analysis. Instead, the  $\beta_5 I_H$  term is chosen to yield values close to those measured at SNL-6 and SNL-15 (presented in Appendix F of (Hart et al., 2008), Table F-1); this value is directly modified during the calibration stage in AP-114 Task 7 (Hart et al., 2009). The final regression equation (TFIELD 4.1) and a table of the  $\beta$  values (Table TFIELD 4-1) resulted in a fit characterized by  $R^2 = 0.92$  and  $F = 216$ .

$$T(x, y) = \beta_1 + \beta_2 \cdot d(x, y) + \beta_3 \cdot I_f(x, y) + \beta_4 \cdot I_D(x, y) + \beta_5 \cdot I_H(x, y) + \varepsilon \quad (\text{TFIELD 4.1})$$

The remainder  $\varepsilon$  represents the misfit between the regression model and observed data.

**Table TFIELD 4-1.  $\beta$ -values for regression Equation TFIELD 4.1.**

$\beta_1$	$\beta_2$	$\beta_3$	$\beta_4$	$\beta_5$
-5.69805	$-3.48357 \times 10^{-3}$	2.06581	0.68589	-4.75095

The data and Mathcad sheet used to calculate these values are provided in Appendix A of (Hart et al., 2008).



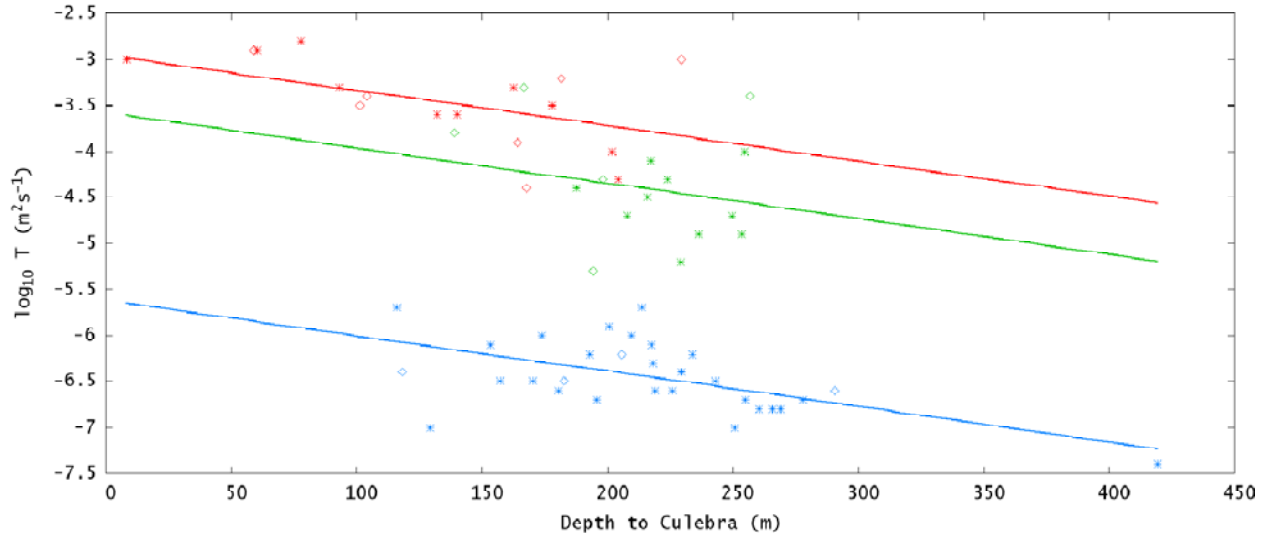


Figure TFIELD 4-1. Regression lines for low-T wells (blue), high-T/non-dissolution wells (green), and wells within the Salado dissolution zone (red).

## ***TFIELD-4.2 Step 2 – Creation of “Soft Data”***

Geologic and hydraulic information are included as “soft data” to maintain the geologic conceptual model through the stochastic indicator kriging simulations in Section TFIELD-4.4. Soft data define probabilities,  $P_{low}$ , that a new well at a given point would have a low T value. For model cells that include wells where  $\log_{10} T$  ( $m^2/s$ )

has been estimated from pumping tests, the observation is referred to as “hard data”, to distinguish it from more indirect contributions to T values. Model cells where hard data (observed  $\log_{10} T$ ) is greater than -5.4 are assigned  $P_{low} = 0$ , while  $P_{low} = 1$  for all cells containing low-T pumping test results. The transmissivity values for all of the wells are presented in

Table TFIELD 4-2. Listing of coordinates, depth and  $\log_{10}$  transmissivity values used in regression model  
Table TFIELD 4-3 (from Listing A.1 of Appendix A in Hart et al. (2008)).

**Table TFIELD 4-2. Listing of coordinates, depth and log<sub>10</sub> transmissivity values used in regression model****Table TFIELD 4-3. Listing of coordinates, depth and log<sub>10</sub> transmissivity values used in regression model**

Well	UTM X NAD27, Zone 13 (m)	UTM Y NAD27, Zone 13 (m)	depth to Culebra (m)	log <sub>10</sub> T (m <sup>2</sup> /s)
H-10b	622975	3572473	419.25	-7.4
P-15	610624	3578747	129.24	-7.0
WIPP-12	613710	3583524	250.7	-7.0
AEC-7	621126	3589381	269.14	-6.8
H-15	615315	3581859	265.79	-6.8
WQSP-3	614686	3583518	260.38	-6.8
H-12	617023	3575452	254.97	-6.7
H-5c	616903	3584802	277.82	-6.7
WIPP-30	613721	3589701	195.69	-6.7
H-17	615718	3577513	219.03	-6.6
SNL-8	618523	3583783	291.5	-6.6
WIPP-21	613743	3582319	225.85	-6.6
WQSP-6	612605	3580736	180.31	-6.6
CB-1	613191	3578049	157.27	-6.5
H-14	612341	3580354	170.23	-6.5
SNL-10	611217	3581777	182.58	-6.5
WIPP-18	613735	3583179	243.08	-6.5
SNL-13	610394	3577600	118.26	-6.4
WIPP-22	613739	3582653	229.51	-6.4
ERDA-9	613696	3581958	218.08	-6.3
C-2737	613597	3581401	205.74	-6.2
H-2c	612666	3581668	192.94	-6.2
WIPP-19	613739	3582782	233.93	-6.2
H-16	613369	3582212	217.46	-6.1
H-4c	612406	3578499	153.31	-6.1
H-1	613423	3581684	209.55	-6.0
P-17	613926	3577466	173.89	-6.0
WQSP-5	613668	3580353	200.67	-5.9
D-268	608702	3578877	115.98	-5.7
H-18	612264	3583166	213.57	-5.7
SNL-5	611970	3587285	194.16	-5.3
H-19b0	614514	3580716	229.2	-5.2
DOE-1	615203	3580333	253.44	-4.9
WQSP-4	614728	3580766	236.42	-4.9
H-3b1	613729	3580895	207.87	-4.7
WQSP-2	613776	3583973	249.72	-4.7
WQSP-1	612561	3583427	215.79	-4.5
H-6c	610610	3584983	187.61	-4.4
SNL-9	608705	3582238	167.64	-4.4
Engle	614953	3567454	204.22	-4.3
H-11b4	615301	3579131	223.93	-4.3
SNL-14	614973	3577643	198.12	-4.3
WIPP-13	612644	3584247	217.17	-4.1
DOE-2	613683	3585294	254.51	-4.0

Well	UTM X NAD27, Zone 13 (m)	UTM Y NAD27, Zone 13 (m)	depth to Culebra (m)	$\log_{10} T$ (m <sup>2</sup> /s)
H-9c	613974	3568234	201.78	-4.0
SNL-18	613606	3591536	163.98	-3.9
SNL-2	609113	3586529	138.99	-3.8
WIPP-25	606385	3584028	140.06	-3.6
WIPP-28	611266	3594680	131.98	-3.6
P-14	609084	3581976	178	-3.5
SNL-17	609863	3576016	101.19	-3.5
SNL-19	607816	3588931	103.94	-3.4
WIPP-11	613791	3586475	256.95	-3.4
SNL-12	613210	3572728	166.73	-3.3
USGS-1	606462	3569459	162.44	-3.3
WIPP-27	604426	3593079	92.97	-3.3
SNL-1	613781	3594299	181.66	-3.2
SNL-3	616103	3589047	229.51	-3.0
WIPP-29	596981	3578694	8.23	-3.0
SNL-16	605265	3579037	58.83	-2.9
WIPP-26	604014	3581162	60.2	-2.9
H-7c	608095	3574640	77.88	-2.8

#### TFIELD-4.2.1 Halite Bounding

Two geologic margins, M2/H2 and M3/H3, are updated in (Powers, 2007a; 2007b) (and summarized in Section TFIELD-2.1.1) as areas of transition from mudstone to halite below and above the Culebra, respectively. Wells penetrating the Culebra in areas that are bounded both above and below by halite (e.g., SNL-6 and SNL-15) have been found to have very low T values, less than  $10^{-11}$  m<sup>2</sup>/s (Roberts, 2007). Wells bounded by only one margin (e.g., H-12 and H-17) have been shown to have lower than average T values.

Because high-T fractures are not predicted where halite is present in the Rustler, model cells located on the combined M2/H2 and M3/H3 margin were assigned a likelihood  $P_{low} = 1$ . This ensures that no high-T areas will be placed on the boundary itself. Additionally, regression results for all model cells in the halite zone will be replaced with values directly from the regression equation, eliminating any high-T indicators that may have been placed east of the margin by the simulation.

#### TFIELD-4.2.2 Gypsum Cements

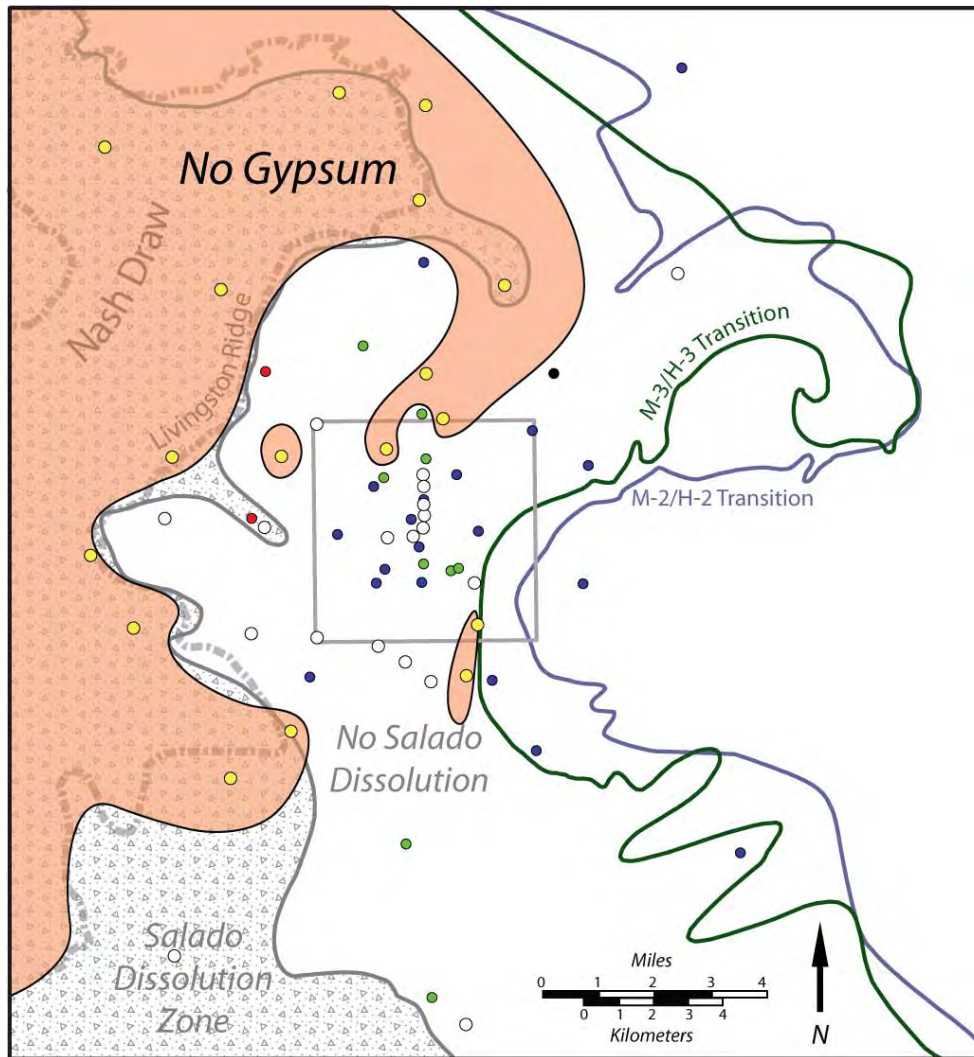
The amount of gypsum cements in fractures and vuggy porosity within the Culebra is believed to be inversely related to Culebra T (Beauheim and Holt, 1990). They postulated that gypsum fracture fillings limited Culebra T by closing fracture apertures, filling critical fracture junctions. The postulated relationship remained qualitative because too few well locations had both measured T values and describable core. Since 1990, the Culebra has been cored and hydraulically tested at 24 additional locations, providing sufficient data to construct a quantitative model linking Culebra T with the presence of gypsum cements.

In Appendix F of Hart et al. (2008), a simple quantitative model is constructed relating Culebra gypsum content to T. Using units defined by Holt (1997), maps were developed that illustrate the spatial occurrence of gypsum in the Culebra using a gypsum index that accounts for the relative gypsum content in the Culebra (Figure TFIELD 4-2 and Figure TFIELD 4-3). Using a critical value of the gypsum index, the high-T/low-T status of Culebra well locations can be predicted with an accuracy of greater than 97% for WIPP well locations where both sufficient core and T data exist. These maps reveal that regions of no gypsum occur predominantly where Salado dissolution has affected the Culebra and that the low-gypsum region in the WIPP area is similar to the high-diffusivity region defined by Beauheim (2007), see Figure TFIELD 4-4. Soft data are used to incorporate information about the influence of gypsum content on Culebra T.

In all cases where sufficient core and T data exist, wells with no gypsum (Figure TFIELD 4-2) have high T, due to well-interconnected fractures. To account for this relationship, cells are assigned  $P_{low} = 0.05$  where there is no gypsum present. As can be seen in Figure TFIELD 4-2, this is a fairly large area; rather than give all the cells in the area such a low  $P_{low}$  value, cells were selected from a 13-cell tetrahedral grid to receive soft data assignments (Figure TFIELD 4-5). After some experimentation, a value of 13 cells was used as the grid spacing because it provided sufficient definition of the boundaries without overwhelming the simulation program.

It is observed that in all cases where sufficient core and T data exist, wells outside of the low-gypsum region (Figure TFIELD 4-3) have low T, because fracture interconnectivity is limited by gypsum cements. In the indicator kriging, areas outside of the low-gypsum region are assigned  $P_{low} = 0.95$ , to increase the likelihood of predicting low T in the simulation.

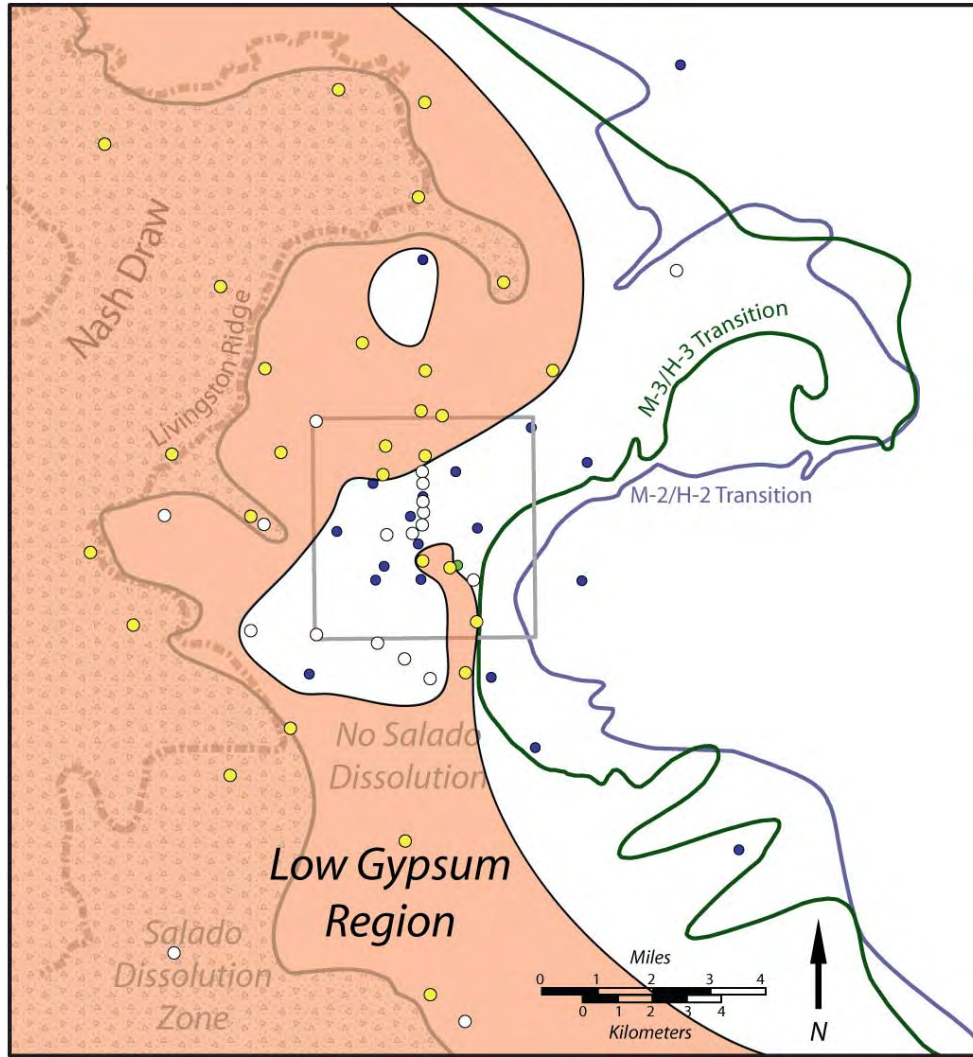
Because the areas of no-gypsum and high-gypsum content cannot, by definition, overlap, the high-gypsum data are sampled on the same tetrahedral grid used by the no-gypsum data. By using fractional likelihoods and sparse sampling, these soft data do not overwhelm the random sampling algorithm of SISIM and allow for greater variation between base field realizations. The high/low-gypsum content map is shown in Figure TFIELD 4-3. The low-gypsum region is not sampled, since it overlaps the no-gypsum region. Instead, the high-gypsum region is used. The area of high gypsum directly north of the WIPP Land Withdrawal Boundary (LWB) is sampled using a square 3-cell grid, to compensate for the diffusivity soft data described in the next section.



Explanation

- High T Location - Salado Dissolution
- High T Location - No Dissolution
- Low T Location
- No Gypsum
- No Gypsum Data
- No Hydraulic Data

Figure TFIELD 4-2. Areas where no gypsum has been found in core samples. A selection of points within this area received low  $P_{low}$  values, indicating the greater likelihood of having higher T values.



Explanation

- High T Location - Salado Dissolution
- High T Location - No Dissolution
- Low T Location
- Low Gypsum Content
- No Gypsum Data

Figure TFIELD 4-3. Areas where wells have either no or low gypsum content. The areas not shaded, therefore, are likely to have high gypsum content and lower T, and this white area receives high  $P_{low}$  values.

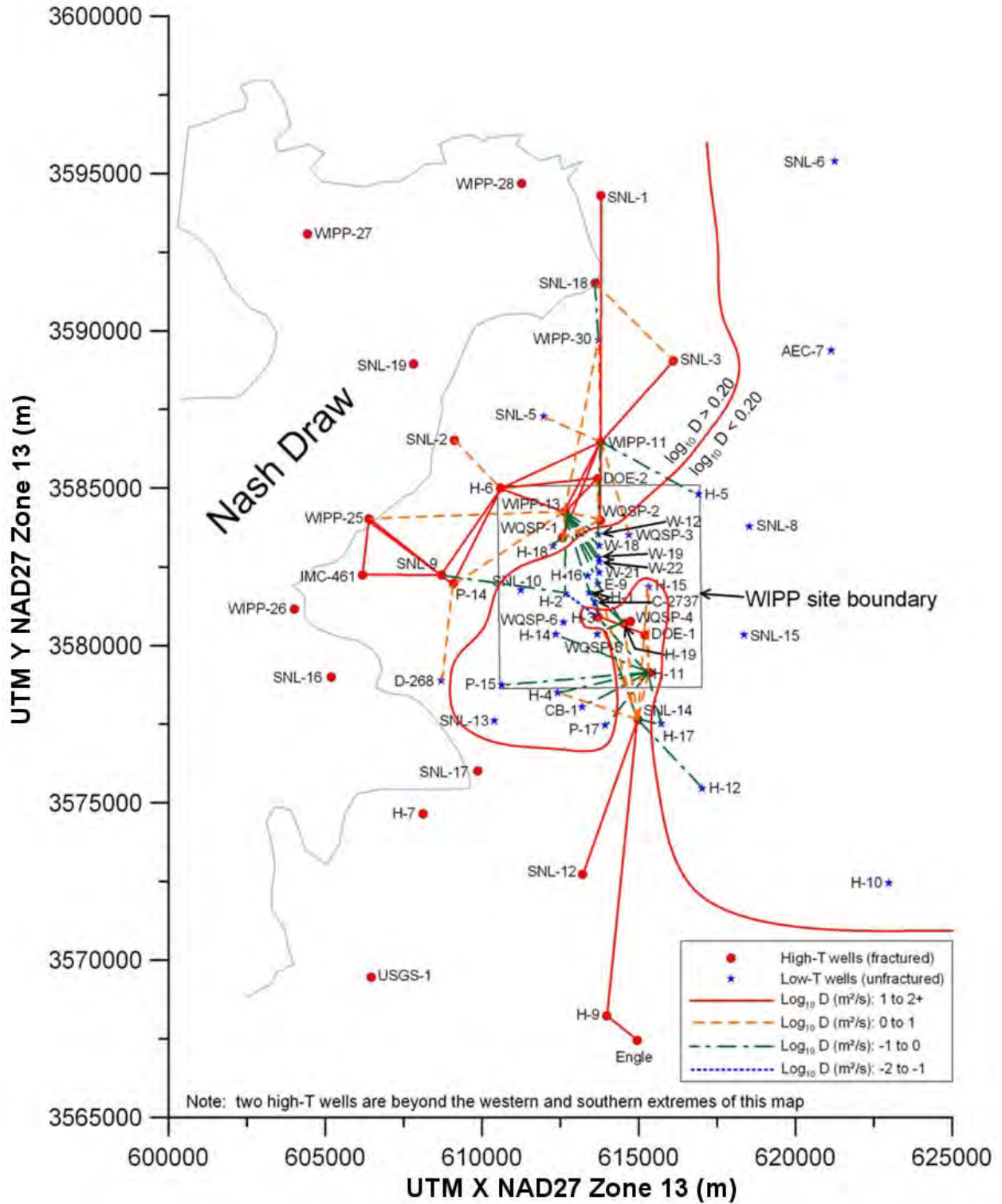


Figure TFIELD 4-4. Diffusivity values calculated between wells from pumping test data. Connections where  $\log_{10} D > 0.2$  are included as conditioning data with  $P_{low} = 0.25$ .

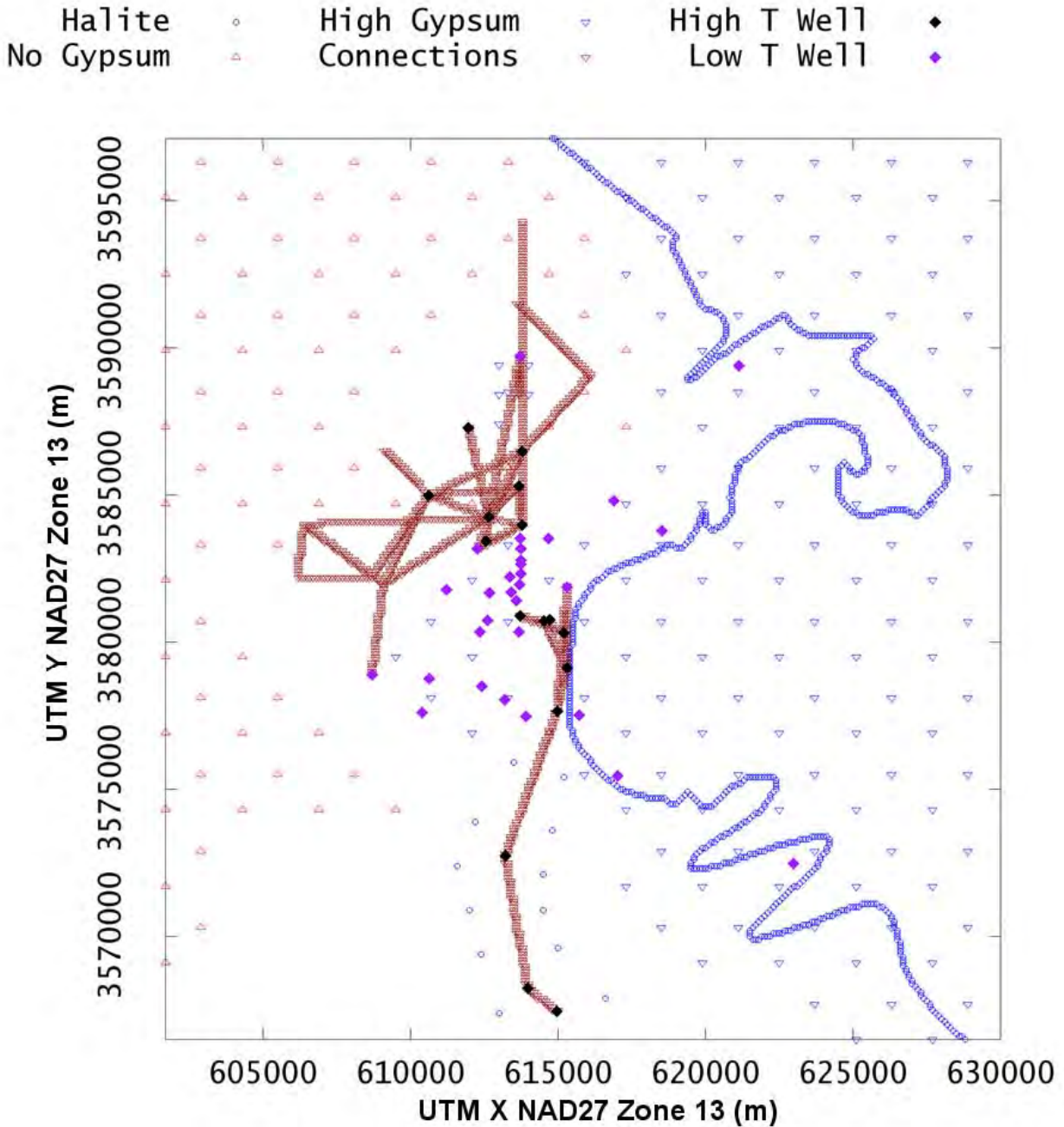


Figure TFIELD 4-5. Soft data points (open symbols) generated during step 2. Hard data points (filled symbols) are located at wells with pumping test estimates of T.

### TFIELD-4.2.3 Diffusivity and Hydraulic Connections

Expressions of the degree of hydraulic connections between pairs of wells are also brought into the construction of the base fields using soft data. The diffusivity  $D$  ( $m^2/s$ ) of the overall connection



between any pumping and observation well has been calculated for many hydraulic tests that have been performed at the WIPP site (Beauheim, 2007), and a map of these values is shown in Figure TFIELD 4-4. The cells between two wells that have a calculated  $\log_{10} D > 0.2$  were assigned  $P_{low} = 0.25$ , to account for the increased likelihood that a cell on the connecting line will be high T. Using  $P_{low} = 0$  would have forced SISIM to create a direct path connecting two wells where a strong response to pumping was observed, and there is no geologic reason that these connections would have to be straight.

In addition to the high-T connection lines, a set of low-T points was placed adjacent to the SNL-14/SNL-12/H-9 connection path to keep the high-T connection relatively narrow. Pumping at the SNL-14 well produced a strong response at the H-9 well nearly ten kilometers to the south. During testing of the hydraulic models, it was found that the only way to get this type of response was to have a relatively narrow connecting zone of high T. Without adding some low-T points along the flanks of this path, SISIM tended to create a high-T area too wide to allow any drawdown response to propagate from SNL-14 to H-9. Also, this type of response seems to indicate a linear feature, which is difficult to model on a 100-m grid scale. These low-T points were only guidance points, and many base fields still have large areas of high T that extend past these points. These points were assigned a  $P_{low} = 1$ , to ensure they would impact the indicator kriging simulation.

#### **TFIELD-4.2.4 Combined Soft Data**

The final, combined soft data field is shown in Figure TFIELD 4-5. The hard data are filled diamonds, with purple points indicating low-T values, and black points indicating high-T values. The soft data were created in MATLAB, using the data files and scripts provided in Appendix B of Hart et al. (2008).

#### **TFIELD-4.3 Step 3 – Indicator Variography**

The geostatistical indicator simulations done as part of the base T-field development are only utilized in the central section of the model domain, between the Salado dissolution area to the west and the low-T halite-sandwiched region to the east. Therefore, only wells in this middle section are used for construction of the indicator variogram. There are a total of 46 wells that provide information regarding  $\log_{10} T$  used in the calculation of the indicator variograms. The indicator value is determined by comparing each  $\log_{10} T$  value to a threshold  $\log_{10} T$  value,  $T_t = -5.4$ ,

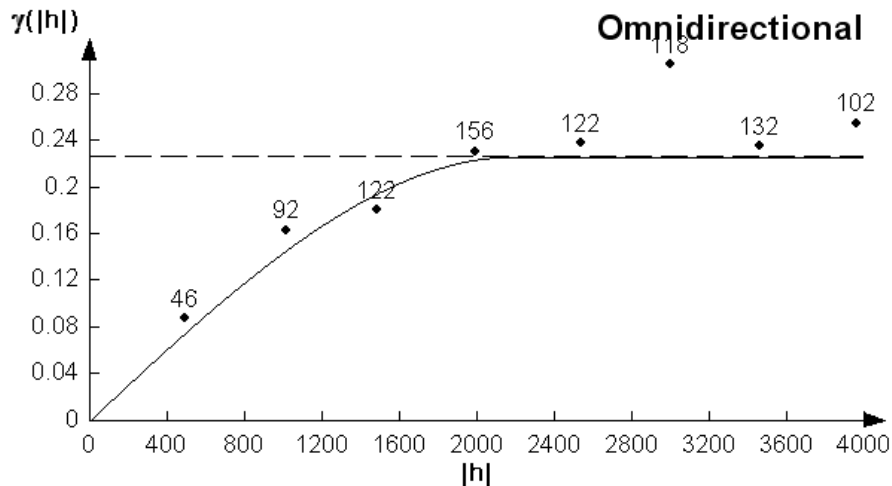
$$I(x, y) = \begin{cases} 1 & \text{if } \log_{10} T < T_t \\ 0 & \text{if } \log_{10} T \geq T_t \end{cases} \quad (\text{TFIELD 4.2})$$

where  $I(x, y)$  denotes the indicator value at well location  $(x, y)$ . The indicator values,  $I$ , and their variograms are unitless. The indicator variogram is fit with a spherical model. The variogram model parameters are given in Table TFIELD 4-4, and Figure TFIELD 4-6 shows the experimental and model variograms. The proportion of low- $T$  values in the data set is 0.652. The variance of an indicator value is  $(1.0 - p)p$ , where  $p$  is the proportion of high or low values. The variance for these indicator data is 0.227 and is used directly as the sill in the variogram modeling (dashed horizontal line in Figure TFIELD 4-6). The parameters in Table TFIELD 4-4 are used as input to

the SISIM program for creation of the stochastic component of the base T-fields. Analyses with directional variograms calculated in the NE-SW and NW-SE directions to identify anisotropy were inconclusive (see Appendix C of Hart et al. (2008)).

**Table TFIELD 4-4. Variogram parameters for isotropic fit to indicator data variogram. Omnidirectional variogram calculated with a lag spacing of 500 m.**

Parameter	Value
Model Type	Spherical
Nugget	0.0
Sill	0.227
Range	2195 m



**Figure TFIELD 4-6. Experimental variogram (dots) and spherical model (line) for indicator values. x-axis is lag distance [meters], y-axis is the unitless indicator.**

#### ***TFIELD-4.4 Step 4 – Conditional Indicator Simulation***

With the indicator variogram model, known T hard data values, and soft data in place, stochastic realizations of high-T zones are constructed using the GSLIB program SISIM (Deutsch and Journel, 1998). Maps summarizing statistics for the resulting fields are presented in Figure TFIELD 4-8 and Figure TFIELD 4-9. These figures show the impact of conditioning information on the overall fields. The combined M2/H2 and M3/H3 margins have a standard deviation of 0 and are constant at the proper value as desired. Areas designated as higher likelihood of high T do show an average value that trends towards the high-T value (in this case, 0), but they still have a standard deviation that is non-zero, indicating that there is still variability in those areas. The same is true in areas outside the low-gypsum region. Additionally, areas with no conditioning information have even higher standard deviations, indicating that placement in those locations is allowed full variability. Though there are some visible artifacts from the grids used in the average and standard deviation fields (locations of soft data points in Figure TFIELD 4-5 are discernable in

Figure TFIELD 4-8 and Figure TFIELD 4-9), the individual realizations, such as Figure TFIELD 4-7, do not show these artifacts. Additionally, the majority of the artifacts occur outside the central zone, which is the only place the indicator fields are used. The indicator fields created by this process are believed to be the best possible combination of hydraulic and geologic conditioning given current data.

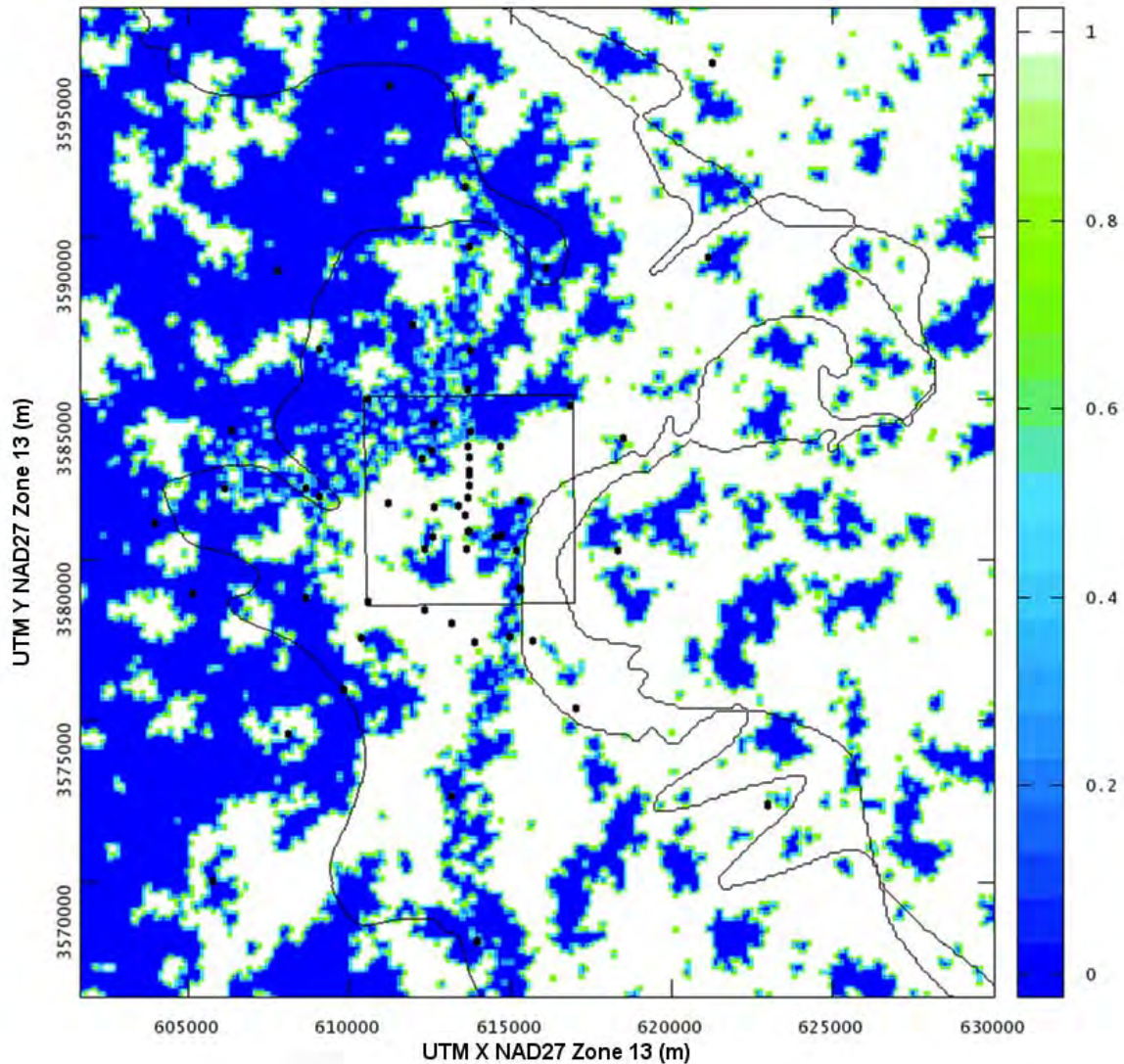


Figure TFIELD 4-7. Sample indicator field for realization r123, where 1 indicates low T and 0 indicates high T.

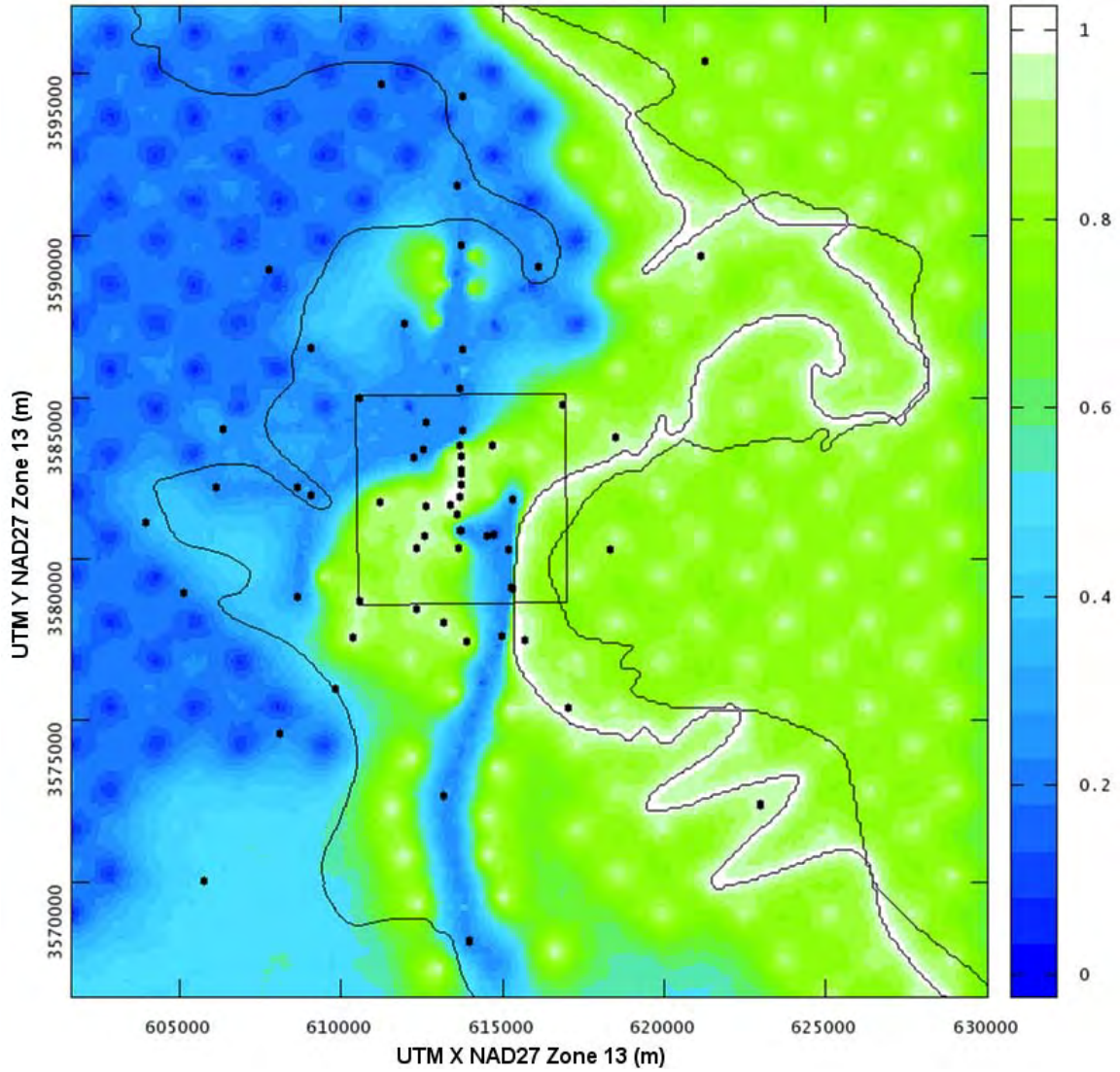


Figure TFIELD 4-8. Average indicator values across all 1000 base realizations.

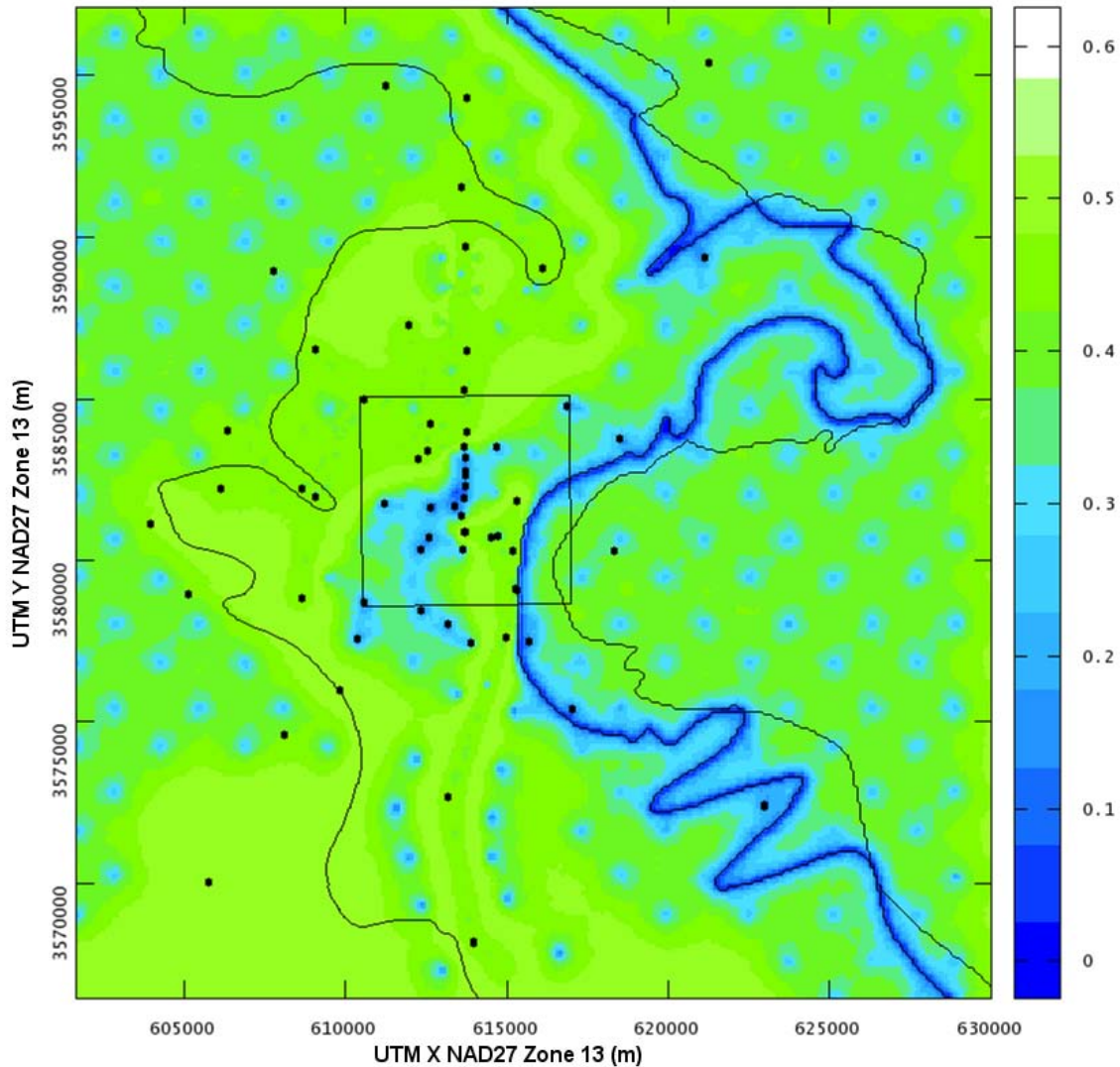


Figure TFIELD 4-9. Standard deviation of indicator values across all 1000 base realizations.

### ***TFIELD-4.5 Step 5 – Construction of Transmissivity Fields***

Once the indicator fields are created, the transmissivity values can be assigned by using regression Equation TFIELD 4.1. A Perl script was written to accomplish this step. This script reads in GEO-EAS formatted data files and produces transmissivity values as output. Following the inputs of these files, **a** and **b** values are required for each zone. These are used as shown in Equation TFIELD 4.3 to calculate the transmissivity value at each cell.

$$\log_{10}[T(x,y)] = \mathbf{b}[Z(x,y)] + \mathbf{a}[Z(x,y)] \cdot d(x,y) \quad (\text{TFIELD 4.3})$$

The **b** and **a** values represent combinations of the  $\beta$ -values based on the zone the cell is located in,  $Z(x,y)$ . Table TFIELD 4-5 shows how the variables in the original linear regression equation (Equation TFIELD 4.1) were related to the variables used in the Perl script that actually executed

the operation (Equation TFIELD 4.3). The map of the indicator zones was shown previously in Figure TFIELD 3-5.

**Table TFIELD 4-5. Correlation of  $\beta$  and  $I$  values from Equation TFIELD 4.1 to the  $a$  and  $b$  values in Equation TFIELD 4.3.**

	<b>Zone 0</b> <i>Salado</i>	<b>Zone 1</b> <i>Halite 2</i>	<b>Zone 2</b> <i>Halite</i>	<b>Zone 3</b> <i>Central low T</i>	<b>Zone 4</b> <i>Central high T</i>
$I_f$	1	0	0	0	1
$I_D$	1	0	0	0	0
$I_H$	0	1	0	0	0
$I_h$	0	1	1	0	0
<b><math>b</math></b>	$\beta_1 + \beta_3 + \beta_4$	$\beta_1 + \beta_5$	$\beta_1$	$\beta_1$	$\beta_1 + \beta_3$
<b><math>a</math></b>	$\beta_2$	$\beta_2$	$\beta_2$	$\beta_2$	$\beta_2$

The Perl script was executed on all realizations. A sample final base transmissivity field is presented in Figure TFIELD 4-10. This is field number r123. The mean  $\log_{10} T$ -field is presented in Figure TFIELD 4-11. The standard deviation of  $\log_{10} T$  is presented in Figure TFIELD 4-12.

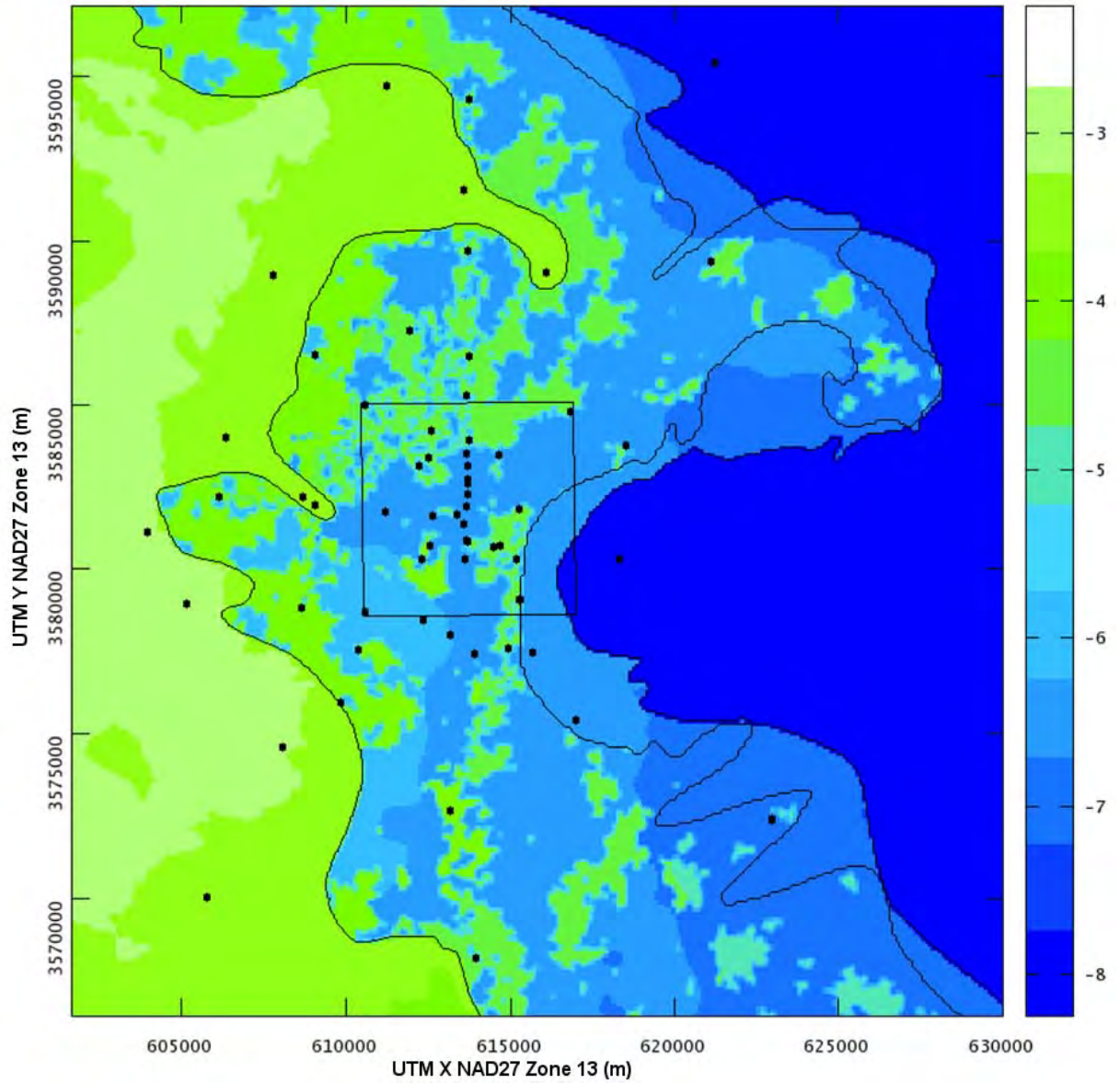


Figure TFIELD 4-10. Sample  $\log_{10}$  T base field realization: r123.

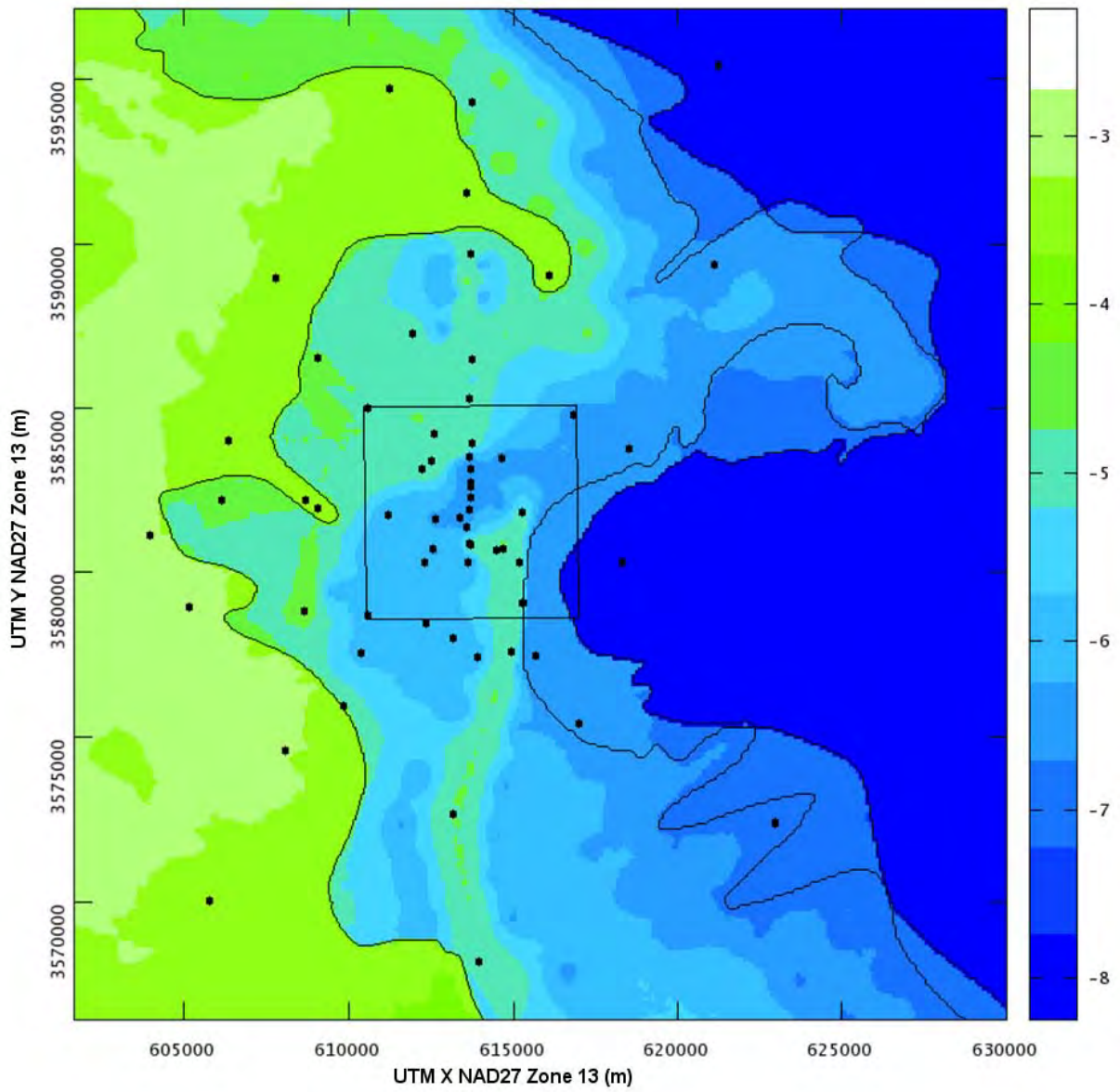


Figure TFIELD 4-11. Mean  $\log_{10} T$  values across all 1000 base realizations.



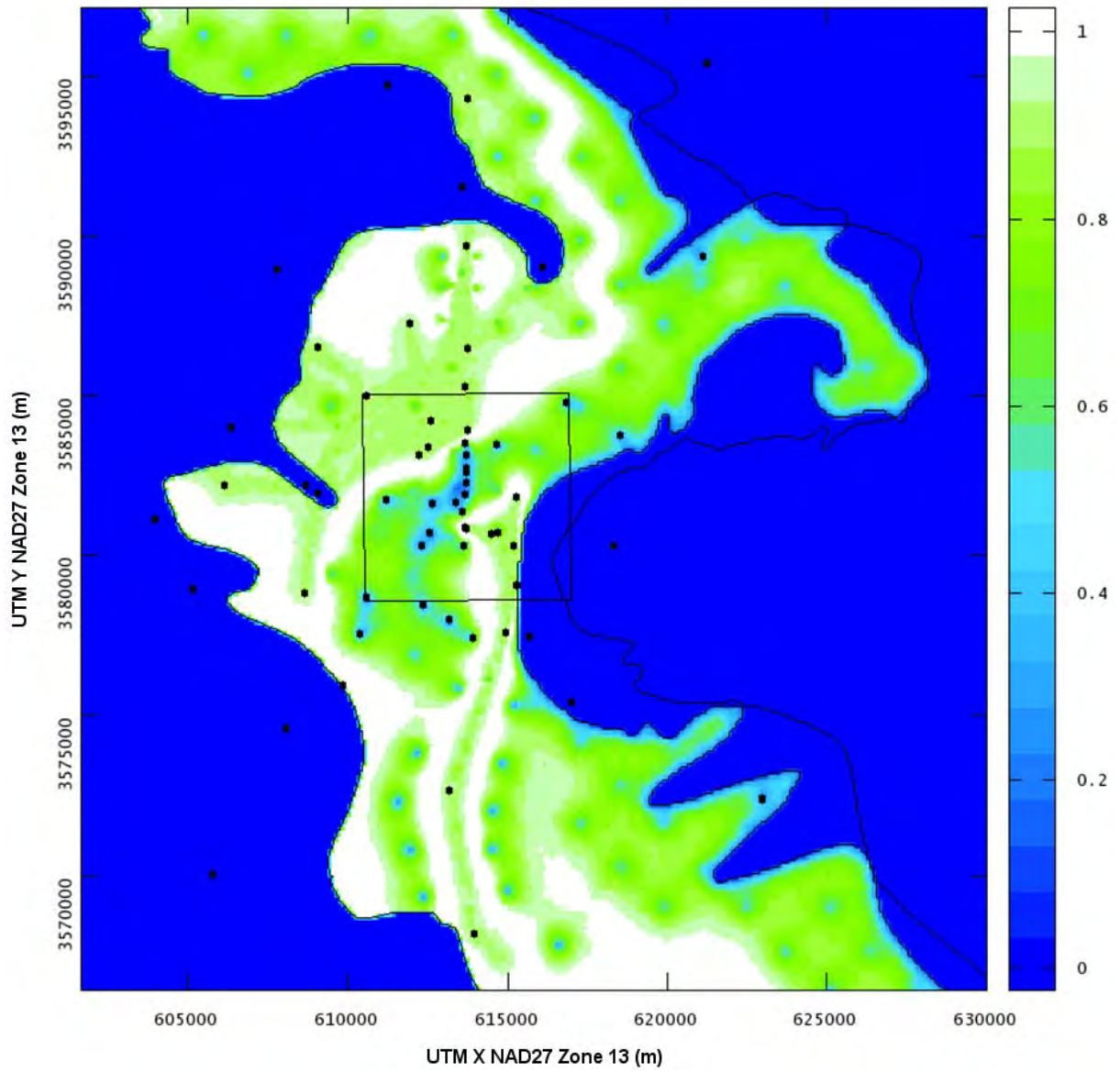


Figure TFIELD 4-12. Standard deviation of  $\log_{10} T$  values across all 1000 base realizations.

## TFIELD-5 T-Field Calibration

The work outlined in section TFIELD-5 was performed under AP-114, Analysis Plan for Evaluation and Recalibration of Culebra Transmissivity Fields (Beauheim, 2004). The calibration of the T-fields was started by taking the 1,000 base fields from the results of AP-114 Task 5 (Hart et al., 2008), and selecting a set of pilot points to use for calibrating T. The initial values for T at these points were taken from the base fields. In addition to transmissivity, the horizontal anisotropy (A) for transmissivity, the storativity (S), and a section of recharge (R) were also calibrated. The same zones used for including soft data (see Figure TFIELD 3-5) were used for transmissivity pilot points, and corresponding zones were used for anisotropy. Zones for storativity and recharge were based on other analyses completed in the area surrounding the WIPP site (see Section TFIELD-5.2.1). Pilot points were selected for each parameter and initial values were selected that were consistent with the conceptual model used to create the base fields (see Section TFIELD-5.2.2 and Section TFIELD-5.2.7).

A model variogram for transmissivity was created using the field values calculated from pumping and other well tests. This variogram was also used for all parameters, as it was the only one that could be created from field data (see Section TFIELD-5.2.8). This variogram was used to create kriging factors that were used to create continuous fields from pilot point values. The T, A, S, and R fields were then ready for use in the MODFLOW numerical model to produce simulated head and drawdown results (see Section TFIELD-5.2.10).

Once the MODFLOW models produced simulated drawdown and head results, the modeled results were compared to the field data for the tests that were modeled. The residual of an observation is calculated in PEST as the weighted difference between measured and modeled data. The observation weights were selected in order to make the sum of the weighted steady-state head errors approximately equal to the sum of errors of four observation wells in a transient pumping test, provided that all error values were equal in magnitude. Because the weights are constant throughout, the weights provide a counterbalance to bring the calibration back into balance if one type of test (steady-state or transient) starts to overwhelm the calibration. In this document, as in the PEST documentation (Doherty, 2000), the term "observation" defines a field measurement, but it does not define the value of that measurement; an observation is a measurement at a specific time and location. The residuals were then used by PEST to construct a finite-difference approximation of the Jacobian matrix used to optimize the pilot point parameter values. The goal of the optimization is to minimize the objective function value, a measure of the misfit between model predictions and observed data (see Section TFIELD-5.2.9).

Because traditional construction of the Jacobian matrix requires at least  $N_p + 1$  forward model calls ( $N_p$  parameters estimated in the calibration), using 1,100-plus parameters would be impossible without additional efficiency in the optimization. The PEST singular value decomposition (SVD) assist approach reduces the size of the Jacobian matrix by only using the most significant "super-parameters" that correspond to the eigenvectors with the largest singular values, estimated using the SVD of the Jacobian. The SVD process required initial calculation of a full Jacobian matrix, but then reduced the subsequent number of required forward calls by a factor of four to six. The result was that three calls to PEST were required to calibrate the fields (see Section TFIELD-5.3.1)

1. a single full Jacobian calculation, which required 1,100+ forward model calls;

2. an SVD calibration using the reduced parameter set that ran up to 50 iterations, requiring between 100 and 400 forward model calls per iteration;
3. a final PEST run with the best parameter results to create the final fields corresponding to the best parameter values calculated during the SVD-assisted calibration.

Total calibration time for a single base field was approximately 7 days using 6 processors (1 master node and 5 slave nodes).

After approximately 140 fields had been calibrated, it was found that a few of the steady-state calibration targets were incorrect by several meters. A total of 150 fields were calibrated using the incorrect targets, and an additional 50 fields were started using the corrected heads (Beauheim, 2009; Johnson, 2009). To deal with the incorrect values, a limited re-calibration was performed on the results of the first 150 calibrations (see Section TFIELD-5.3.2). The same process that has been described was followed for the limited secondary calibration, but the initial parameter values were taken from the calibrated results, only the necessary pilot point locations near the updated steady-state head values were allowed to be changed, and the SVD portion of the PEST re-calibration was limited to 10 iterations. The end result was 200 fields, with 150 of these fields having undergone a secondary calibration to incorporate corrected field observation data. The impact of this change is discussed in Section TFIELD-5.3.3.

The end result of the calibration was 200 field sets (transmissivity, anisotropy, storativity, and recharge) calibrated to one set of steady-state heads and nine transient, multi-observation well pumping tests. The 100 best-calibrated fields (those with the smallest residuals) were selected as the final results from this task (see Section TFIELD-5.3.4). Several statistical analyses were performed on the fields themselves to generate average values and variances in the field results (TFIELD-5.4.1).

The complete calibrations were performed under quality-assurance (QA) run control (RC) with inputs and outputs stored in a concurrent versions system (CVS) repository on a central server. The calibrations required approximately six months of continuous runtime on a total of 80 processors; see Hart et al. (2009) for details.

### ***TFIELD-5.1 Model Calibration Targets***

Two sets of head values were used for calibration of the Culebra flow model. The first dataset consists of 42 freshwater head values measured in May 2007, which were used as a steady-state calibration targets (see Table TFIELD 5-1 for values used and see Johnson (2009) for details). The second dataset consists of drawdown data collected during nine independent multi-well pumping tests over more than twenty years (see Table TFIELD 5-2 for lists of observation wells and relevant references).

SNL-6 and SNL-15 are listed as steady-state targets in Table TFIELD 5-1, but they are located in the constant-head portion of the model domain and therefore their corresponding model-predicted values are not adjustable through changes in the transmissivity field.

**Table TFIELD 5-1. Steady-state freshwater head observations used as calibration targets**

Well Name	May 2007 head target (m AMSL)
C-2737	921.23
ERDA-9	924.88
H-2b2	929.62
H-3b2	918.68
H-4b	916.34
H-5b	939.12
H-6b	936.44
H-7b1	914.58
H-9c	912.8
H-10c	922.02
H-11b4	917.09
H-12	916.53
H-15	920.32
H-17	916.24
H-19b0	918.84
IMC-461	928.95
SNL-1	941.86
SNL-2	937.65
SNL-3	939.81
SNL-5	938.59
SNL-6	1110
SNL-8	929.94
SNL-9	932.05
SNL-10	931.54
SNL-12	915.24
SNL-13	918.19
SNL-14	916.33
SNL-15	1060
SNL-16	918.68
SNL-17A	916.78
SNL-18	939.87
SNL-19	937.58
USGS-4	911.11
WIPP-11	940.65
WIPP-13	939.78
WIPP-19	933.66
WIPP-25	937.57
WIPP-30	939.37
WQSP-1	938.28
WQSP-2	939.87
WQSP-3	936.43
WQSP-4	919.5
WQSP-5	918.18
WQSP-6	921.96

**Table TFIELD 5-2. Summary of transient observations used as calibration targets**

Pumping Well(s)	Observation Wells <sup>1</sup>	Total # obs.	Reference
WQSP-2	H-18, DOE-2, WQSP-1, WIPP-13	77	(Beauheim and Ruskauff, 1998)
H-19 and H-11	WQSP-5, H-1, H-15, DOE-1, ERDA-9, WIPP-21, H-3b2	143	(Beauheim and Ruskauff, 1998)
WQSP-1	H-18, WIPP-13	36	(Beauheim and Ruskauff, 1998)
WIPP-11	WQSP-2, WQSP-3, WIPP-12, SNL-9, SNL-5, H-6b, SNL-3, SNL-2, SNL-1, WIPP-30, WQSP-1, WIPP-13	250	(Toll and Johnson, 2006b; Roberts, 2006)
H-11	H-4b, H-12, H-14, H-15, H-17, DOE-1, CB-1, P-15, P-17, H-3b2	130	(Beauheim, 1989)
WIPP-13	WIPP-19, WIPP-18, H-2b2, H-6b, WIPP-12, WIPP-25, DOE-2, WIPP-30, P-14	167	(Beauheim, 1987b)
SNL-14	H-9c, H-4b, SNL-13, SNL-12, H-15, H-17, C-2737, ERDA-9, H-19b0, H-3b2, H-7, H-11b4	252	(Toll and Johnson, 2006a; Roberts, 2006)
P-14	D-268, H-18, WIPP-26, H-6b, WIPP-25	82	(Beauheim and Ruskauff, 1998)
H-3	DOE-1, H-2b2, H-1, H-11b2	69	(Beauheim, 1987a)

1. See Figure TFIELD 4-4 for locations of pumping and observation wells and diffusivity values estimated from pumping tests

## ***TFIELD-5.2 Step 1 – Calibration Setup and Configuration***

This step comprised the setup and configuration processes that were the same for every base field that was calibrated. Step 1 included the creation and definition of zones for each of the parameters and the selection of pilot point locations and initial values. Because of the stochastic nature of the transmissivity fields, unique zones are associated with each field, as defined in Hart et al. (2008). The process to set up each field was the same, but certain elements, such as the exact number of pilot point locations used, were unique to each field.

The model domain and extent are identical to the domain defined in Section TFIELD-3.1. The base T-fields were taken from the results of Section TFIELD-4.5. Some elements were created statically, and were used for every calibration. Some elements were created dynamically for each calibration, but used the same variables and parameters in their creation.

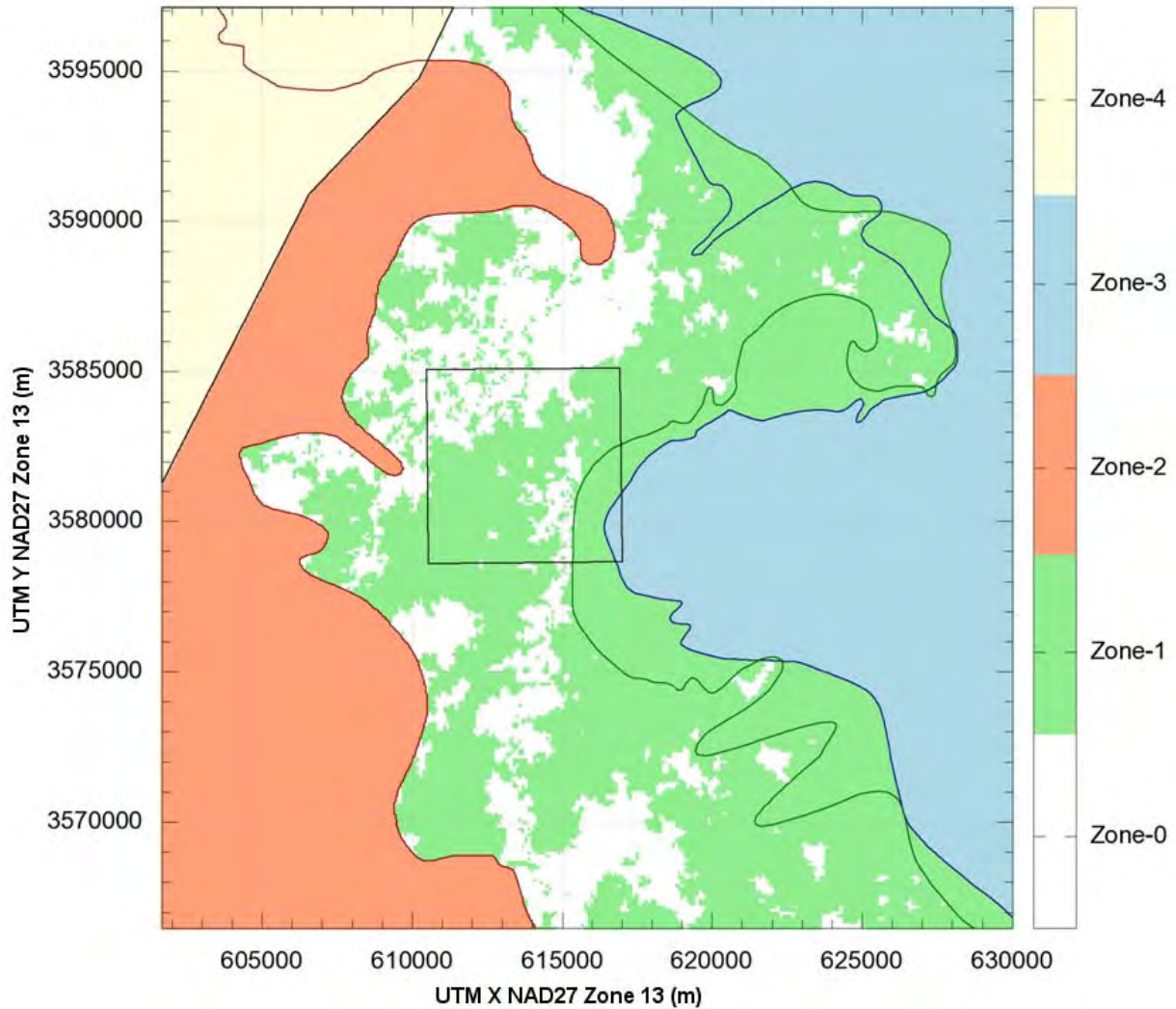
### **TFIELD-5.2.1 Creation of Parameter Zones**

Parameter zones were defined for each of the parameters to be calibrated. These zonations were defined to be consistent with the conceptual model of the Culebra flow defined in Hart et al. (2008) and summarized in Section TFIELD-3. Figure TFIELD 3-2 shows the different margins that define

geologic zones and the locations of the Culebra wells that have been drilled in the vicinity of the WIPP.

### **TFIELD-5.2.1.1 Transmissivity Zones**

The transmissivity zones were defined to be consistent with the zones used in the geologic model and soft data analysis (Section TFIELD-4.2). As shown in Figure TFIELD 5-1, a high-transmissivity zone exists to the west (zone 2), corresponding to the area of Salado dissolution, and a mixture of higher and lower transmissivity values corresponding to the stochastic zones (zone 0 and 1) provided in the base fields defined the center of the model domain. Unlike AP-114 Task 5 (Section TFIELD-4.5), where it was a separate zone, the area between the H2/M2 and H3/M3 margins (green in Figure TFIELD 5-1) was included in the same zone (zone 1) as the lower T stochastic areas provided by the base fields. The area east of both the H2/M2 and H3/M3 margins – where the Culebra is bounded both above and below by halite-cemented elements – was defined to be its own zone (zone 3), as was done in AP-114 Task 5. A no-flow boundary that roughly follows the center of Nash Draw is the final zone (zone 4) defined for transmissivity, and the only zone that applies to all parameters.



**Figure TFIELD 5-1. Transmissivity zone map for a single realization. Zones 0 and 1 are the stochastic zones created in (Hart et al., 2008); Zone 2 is the high-T Salado dissolution area; Zone 3 is the very low-T halite-bounded area; Zone4 is inactive (no flow).**

### **TFIELD-5.2.1.2 Horizontal Anisotropy Zones**

Because the anisotropy fields contain cell-by-cell anisotropy values for transmissivity (and only transmissivity), the exact same zones defined for transmissivity were reused as the zones for anisotropy. The transmissivity values in the north-south ( $y$ ) direction were calculated by multiplying the transmissivity value for the east-west ( $x$ ) direction (given in the T-field) by the anisotropy value ( $A$ ) at a given cell:

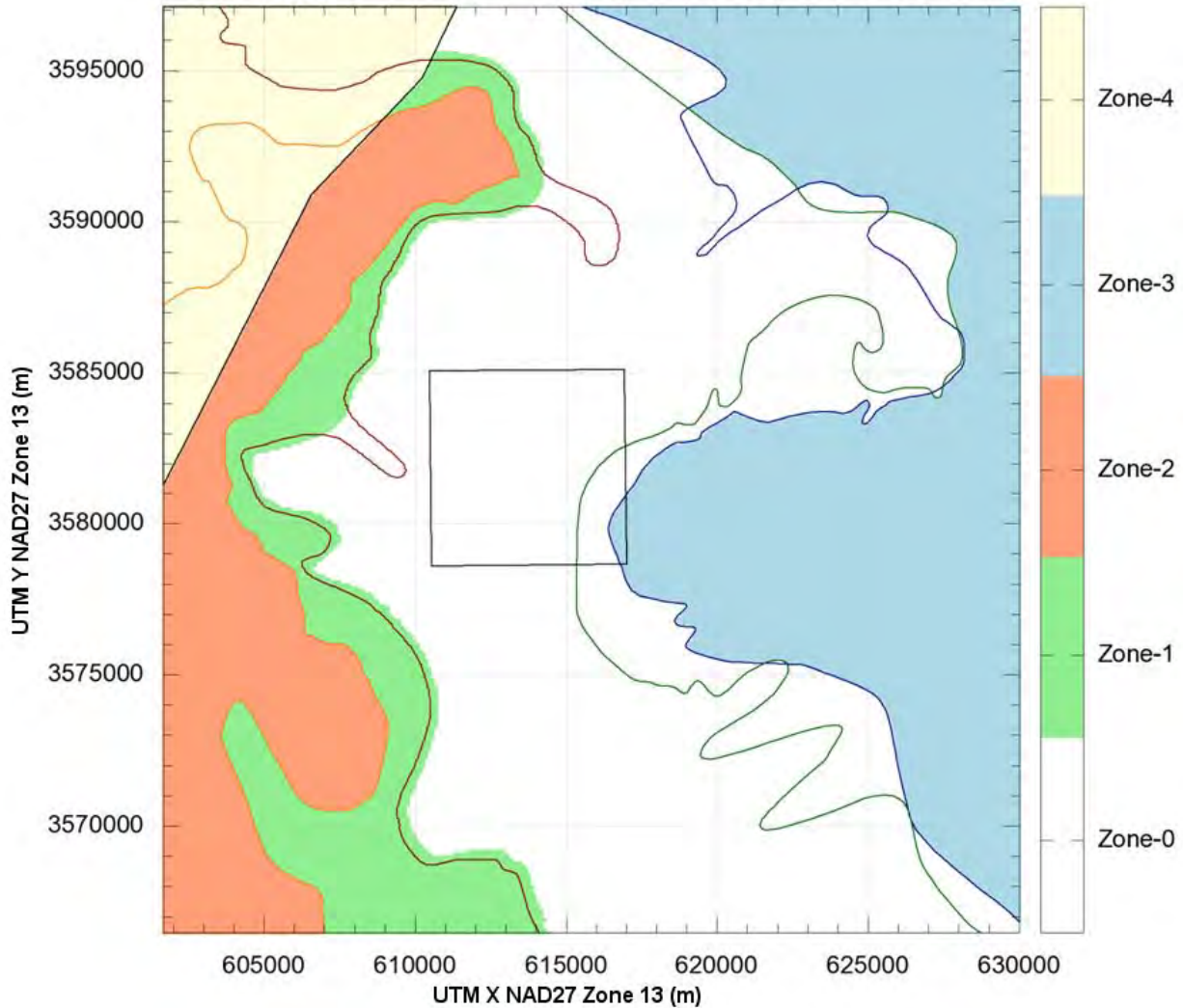
$$T_{NS} = T_{EW}A \quad (\text{TFIELD 5.1})$$

The map shown in Figure TFIELD 5-1 represents the zonation for both  $A$  and  $T$ .

### **TFIELD-5.2.1.3 Storativity Zones**

Besides the no-flow zone (zone 4), four zones were defined for storativity. The westernmost zone (zone 2) is the unconfined zone, as described in Powers et al. (2006) (summarized in Section TFIELD-2.2.2). The largest zone (zone 0), with its western boundary roughly following the Salado dissolution margin, is the area considered to be fully confined. The area between these two zones (zone 1) is the transition zone, where the Culebra is uncertainly confined. As with the T and A zones, the area east of both the H2/M2 and H3/M3 margins is a separate zone (zone 3), but in this case storativity is simply held constant at the initial confined-zone value. The main purpose in defining an "unconfined" zone as a storativity zone is to simplify the model by approximating the non-linear unconfined problem with a linear storativity model. By defining a much higher storativity value in the "unconfined" part of the domain, unconfined behavior can be approximately modeled using a confined and quicker executing numerical model. A map of the storativity zones is shown in Figure TFIELD 5-2.





**Figure TFIELD 5-2. Storativity zones; Zone 0 is confined; Zone 1 is transition between confined and unconfined; Zone 2 is unconfined; Zone 3 is confined and held static at the initial confined value; Zone 4 is inactive (no flow)**

#### **TFIELD-5.2.1.4 Recharge Zones**

The conceptual model presented in Holt (1997) and Hart et al. (2008) indicates that a groundwater divide exists somewhere southwest of the WIPP site. Previously, this groundwater divide was represented by extending the no-flow zone all the way to the southern boundary (McKenna and Hart, 2003). Because the model used in this current task included the unconfined zone, it was decided to model the groundwater divide using recharge instead of a no-flow boundary. The areas of possible recharge were defined in AP-114 Task 1B (Powers, 2006), summarized in Section TFIELD-2.2.1. Recharge values had to be extremely small (on the order of  $10^{-11}$  m/s) so steady-state MODFLOW simulations would converge. Rather than try to determine which of the configurations presented in Task 1B was the "best" approximation, a similar simple approximation to the older no-flow approach was used. A recharge zone consisting of a line of cells extending NW to SE along the axis of the largest topographic feature (and roughly following the old no-flow

boundary from (McKenna and Hart, 2003)) was used as the recharge zone; see Figure TFIELD 5-3 for a map of the recharge zone.

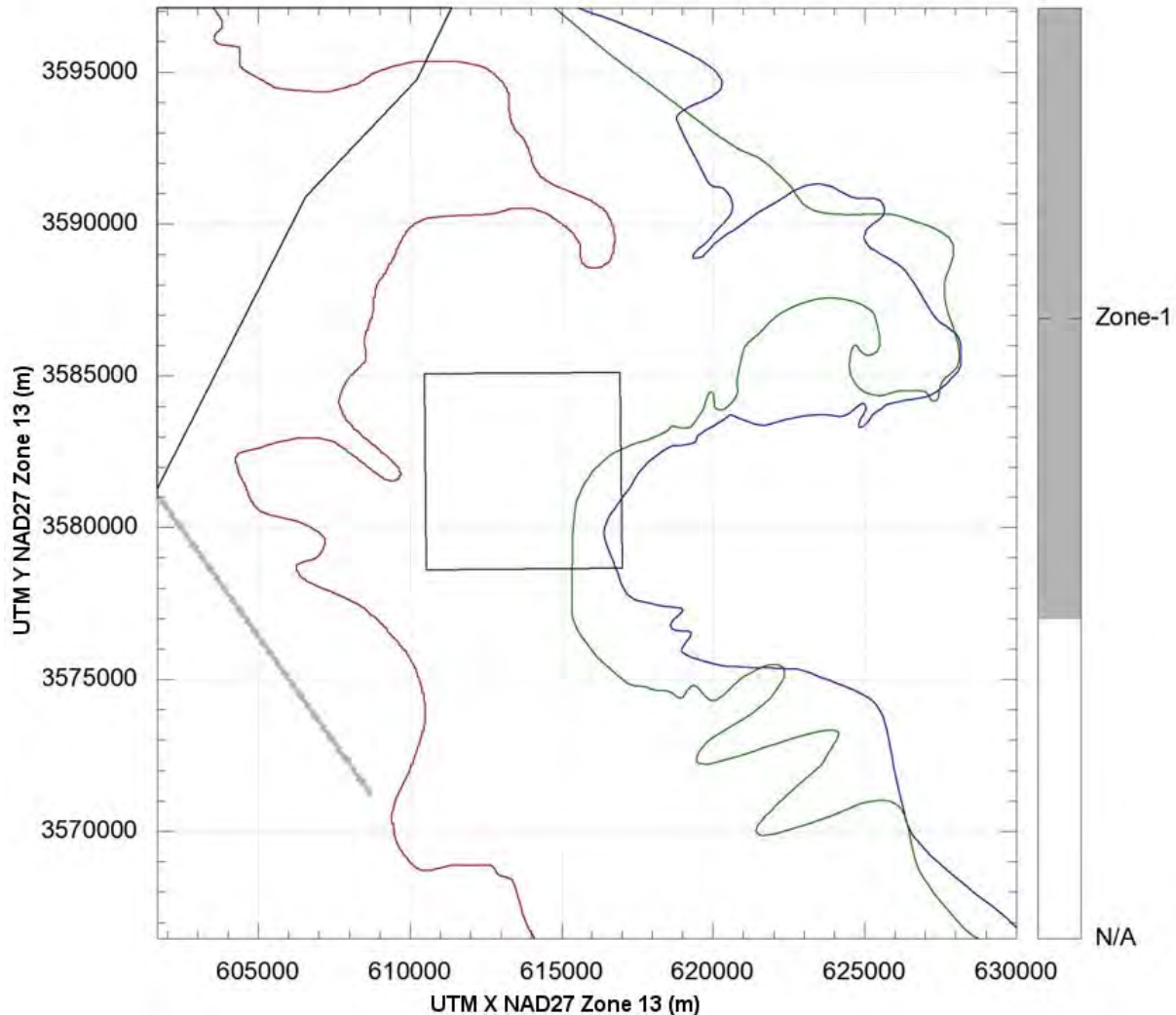


Figure TFIELD 5-3. Zone 1 is the area of recharge; the remaining area had no recharge.

### TFIELD-5.2.1.5 Flow, No-Flow, and Fixed-Head Zones

While the boundary conditions were not variable parameters in the calibration, the definition of the specified-head boundary conditions was an important part of the setup and configuration step. The no-flow zone in the northwest was defined to be the same as was used in AP-088. Though the transmissivity in this area is extremely low ( $10^{-13}$  to  $10^{-11}$  m<sup>2</sup>/s), there should be some flow exiting along the zone margin, however minute. Testing at SNL-6 and SNL-15 indicates that the hydraulic heads in this area are at or above ground level (Roberts, 2007; Bowman and Roberts, 2008). The "halite-sandwiched" zone east of either M2/H2 or M3/H3 was simultaneously made extremely low T and set to fixed-head values at the ground surface elevation. While this meant that the head values at SNL-6 and SNL-15 were no longer estimable, it was considered the simplest way to

model the nearly stationary nature of the water in this zone using MODFLOW-2000. The flow zones are shown in Figure TFIELD 5-4, and the selection of the initial values is discussed in Section TFIELD-5.2.7. The northern, western, and southern flow boundaries were all fixed-head boundaries.

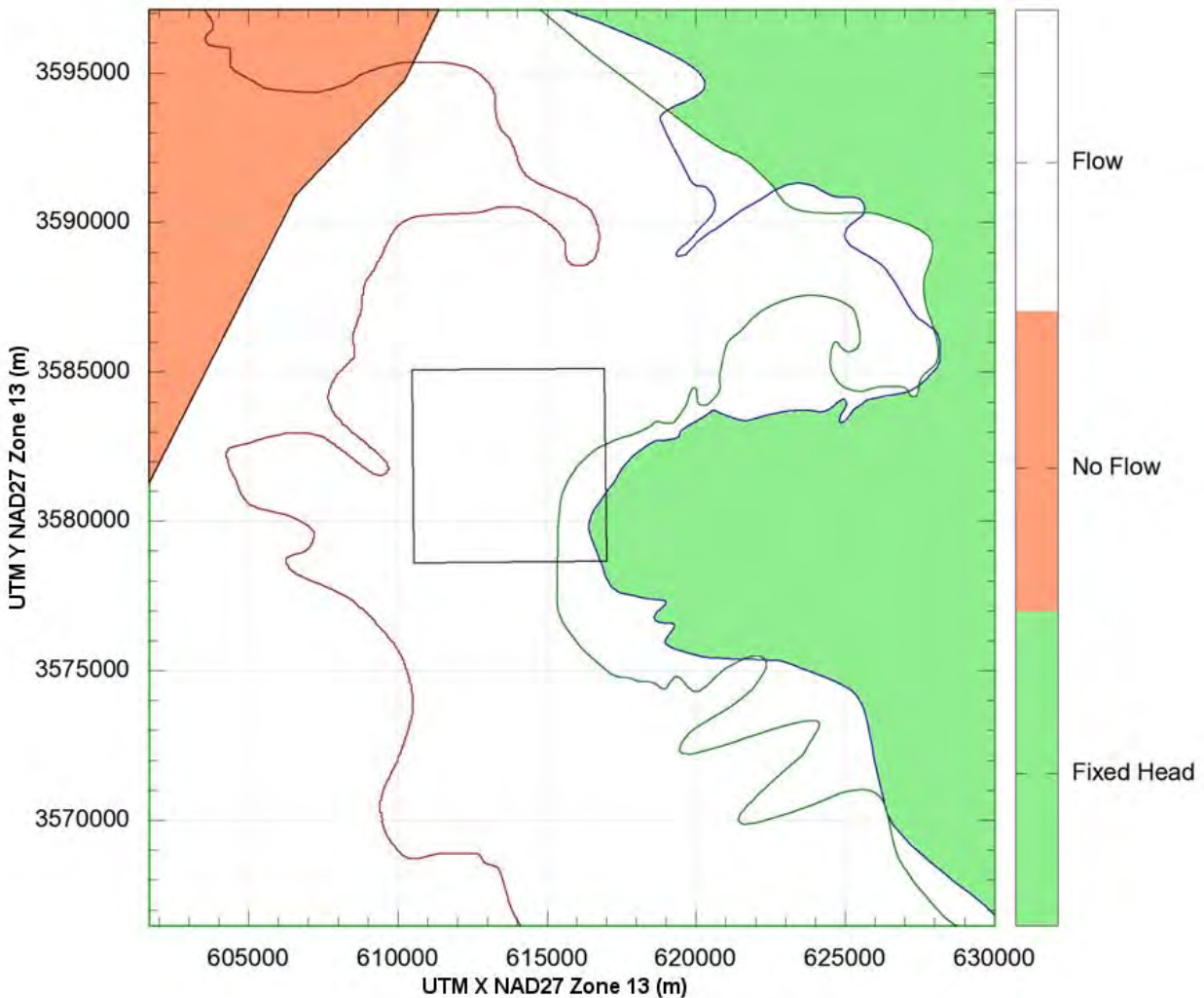


Figure TFIELD 5-4. Flow zones: the fixed-head zone is green; the no-flow zone is salmon; the white area is normal flow. The fixed-head zone includes one cell along the boundaries.

### TFIELD-5.2.2 Selection of Pilot Point Locations

Once the zones were defined, pilot point locations were selected. There were two types of pilot points, fixed and variable, and two placement approaches, gridded and linear. Selection of the points for each parameter required a combination of both types and approaches. The exact algorithm used to calculate placement is detailed in Hart et al. (2009), and resulted in the pilot point locations used.

Because the zones are unique for each base field, this process was done for each field to be calibrated. The pilot point locations are the same for all fields, but some points may belong to two

zones in one field and only to one zone in another. As a result, the pilot point identifiers are not necessarily the same between realizations.

### TFIELD-5.2.3 Transmissivity-Specific Pilot Point Settings

In addition to the pumping test wells, extra pilot points were placed in the transmissivity fields. These were included along the northern and southern boundaries to try to limit the effects that the fixed-head boundaries would have on transient pumping and the steady-state model results. The measured transmissivity values from single-well pumping and slug tests were used as fixed transmissivity points at their corresponding wells (see

Table TFIELD 4-2. Listing of coordinates, depth and  $\log_{10}$  transmissivity values used in regression model Table TFIELD 4-3 for test-derived transmissivity values) – see Table TFIELD 5-3 for the ranges of pilot point values used, and see Figure TFIELD 5-5 for the locations of all the pilot points.

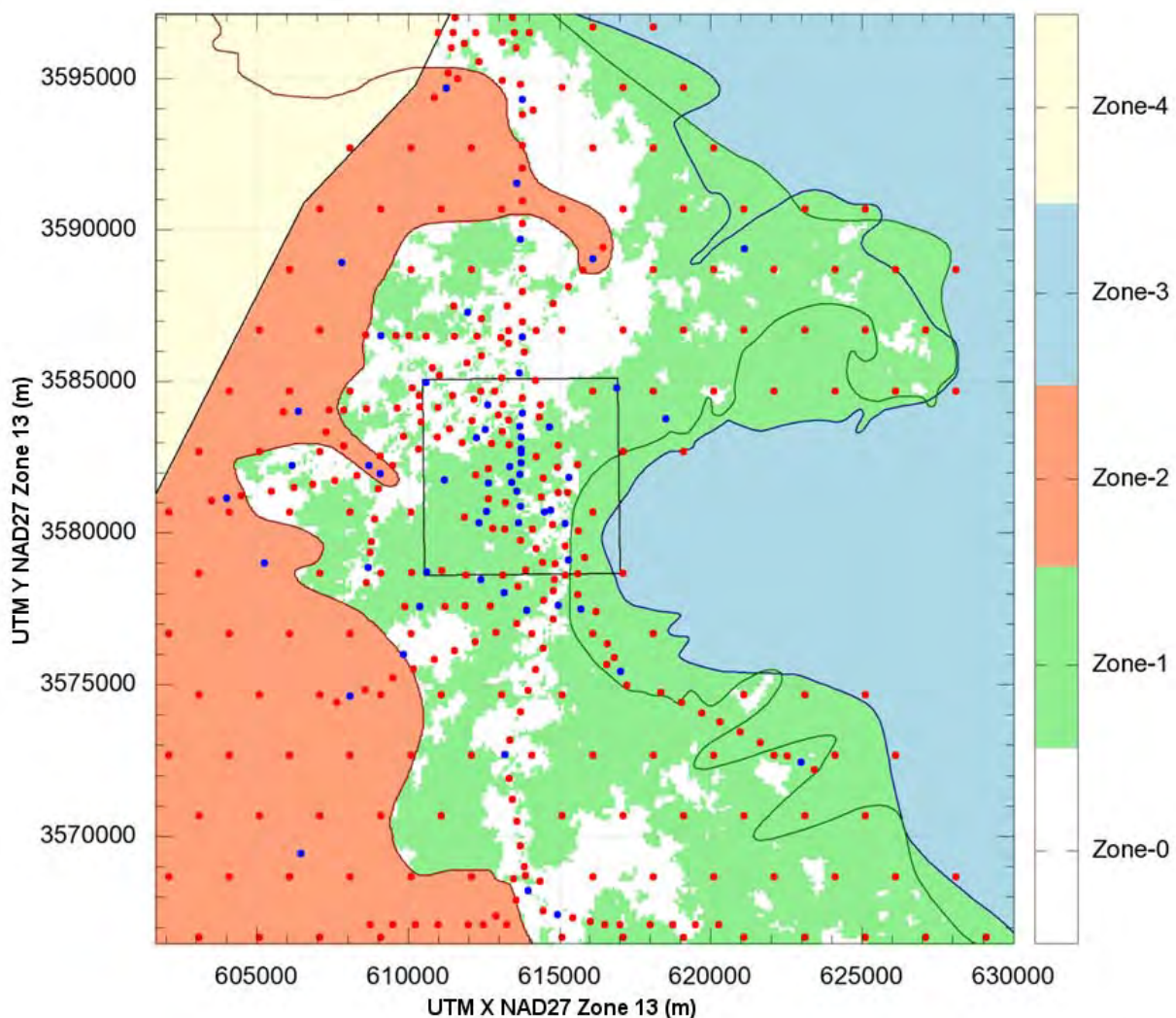


Figure TFIELD 5-5. Transmissivity pilot point locations. Blue points are fixed values and red points are variable parameters.

### TFIELD-5.2.4 Anisotropy-Specific Pilot Point Settings

Anisotropy was unique because no fixed values and therefore no fixed pilot points were used. This result is due to the single-well tests not providing any estimate of anisotropy, and the multi-well tests providing too localized an estimate of anisotropy (only valid for a single cell or two in the model). See Figure TFIELD 5-6 for the locations of anisotropy pilot points.

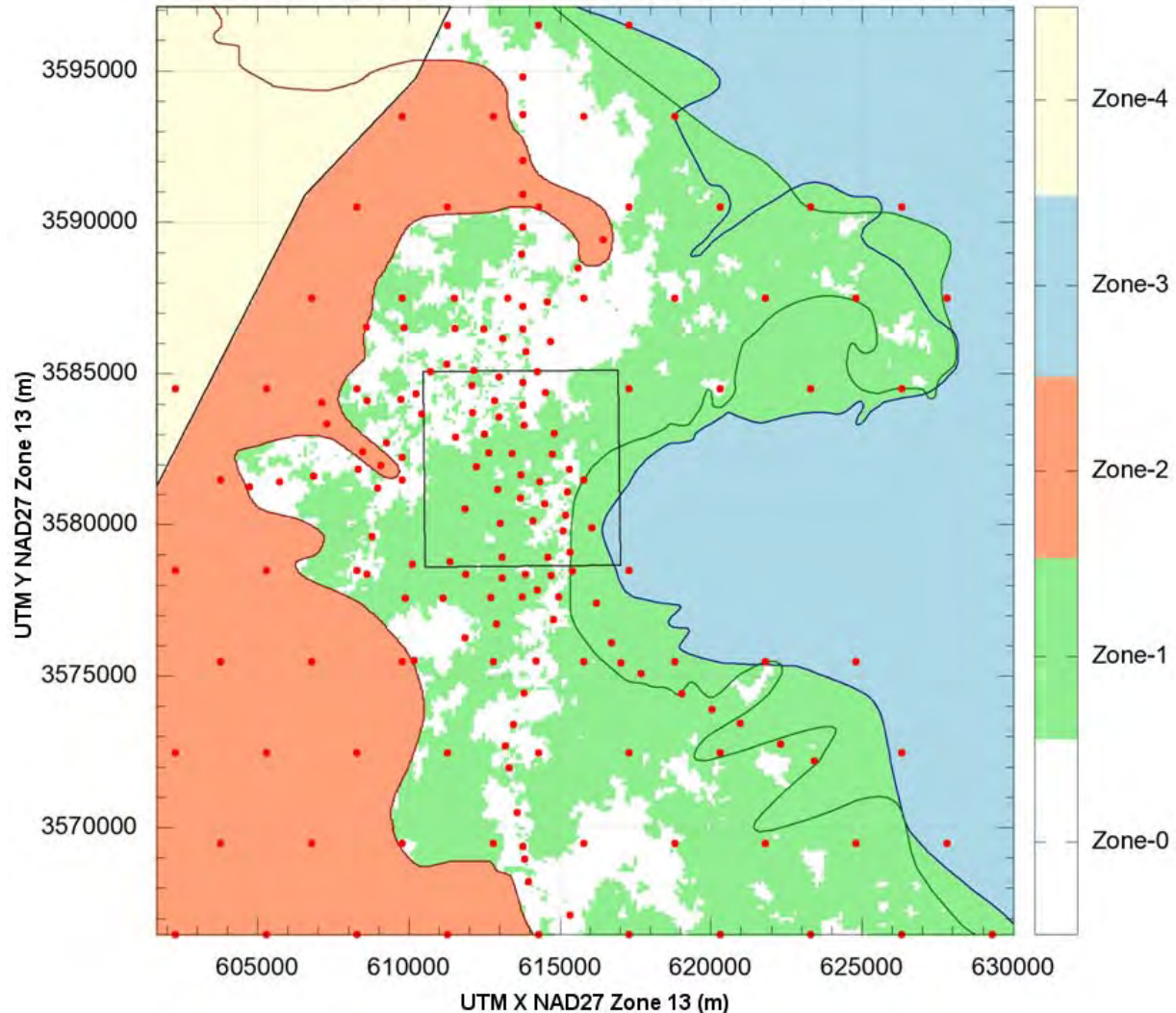
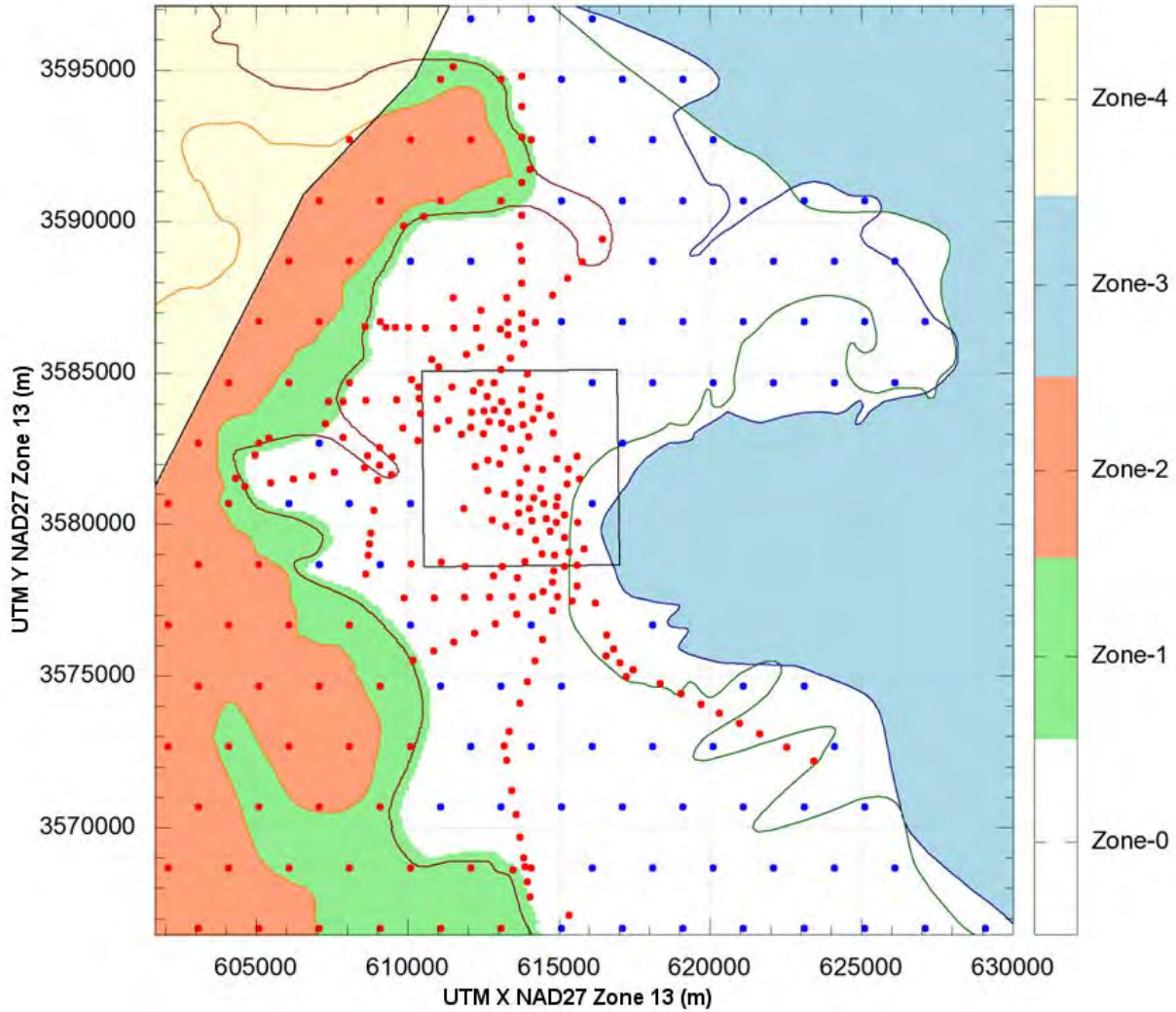


Figure TFIELD 5-6. Anisotropy pilot point locations. All anisotropy pilot points were variable parameters.

### TFIELD-5.2.5 Storativity-Specific Pilot Point Settings

The only variable storativity pilot points in the confined zone were along transient pumping test connectivity axes. The gridded points were set as fixed values, since there was no information that would allow effective calculation of storativity outside the transient tests. All pilot points located within the unconfined and transition zones were defined as variable. See Figure TFIELD 5-7 for the location of storativity pilot points.



**Figure TFIELD 5-7. Storativity pilot point locations. Only pilot points along transient pumping test connections and points in the unconfined zones (zones 1 and 2) were variable (red dots), the remaining points were fixed at the initial storativity value (blue dots).**

### **TFIELD-5.2.6 Recharge-Specific Pilot Point Settings**

Because the recharge zone was a line, only four pilot points were needed in the entire zone. In this case, the pilot point nearest the western domain boundary was set as a fixed value of  $10^{-30}$   $10^{-30}$  m/s, which was interpreted as 0 by the pre-processors to MODFLOW, and the other three were variable. See Figure TFIELD 5-8 for the location of the recharge pilot points.

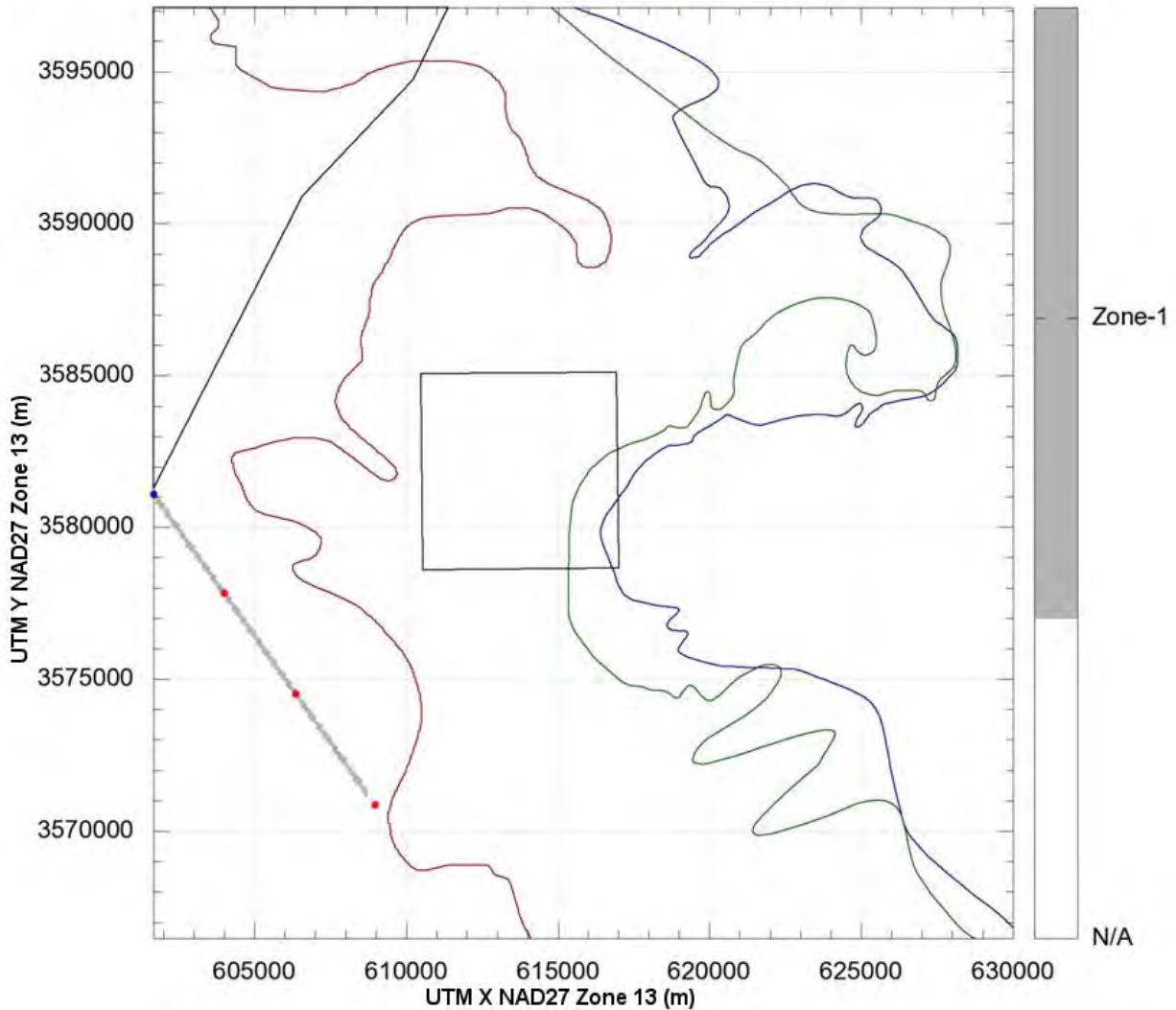


Figure TFIELD 5-8. Recharge pilot point locations.

## TFIELD-5.2.7 Selection of Initial Values

### TFIELD-5.2.7.1 Parameter Initial Values

The initial values for each of the pilot points were defined according to the conceptual model and the values presented in Hart et al. (2008), and summarized in Section TFIELD-3. For transmissivity, this meant that the same equation used to create the base transmissivity fields was used to define the initial values for the pilot points, based on their zone. Anisotropy was set to isotropic conditions ( $A = 1.0$ ) for all points. Storativity was defined to start at  $10^{-5}$  for the confined zone (the same value that was used for storativity in AP-088), at  $10^{-4}$  in the transition zone, and at  $10^{-1.5}$  in the unconfined zone. Recharge was initialized as  $10^{-11}$  m/s, which was a value that was found to be sufficiently small to allow MODFLOW to perform an initial run prior to PEST calibration. The zone-by-zone initial values for each parameter, and the limits placed on the range the values could take in calibration, are presented in Table TFIELD 5-3.

Table TFIELD 5-3. Initial values of parameters at pilot points. See

**Table TFIELD 4-2. Listing of coordinates, depth and  $\log_{10}$  transmissivity values used in regression model**  
**Table TFIELD 4-3 for T values.**

Parameter	Zone	$\log_{10}$ Value <sup>1</sup>	Pilot Point $\log_{10}$ Calibration Limits
Transmissivity	Zone 0	$-0.003484 \cdot d(x, y) - 3.6322$	[-19.0, -1.0]
	Zone 1	$-0.003484 \cdot d(x, y) - 5.6981$	[-19.0, -1.0]
	Zone 2	$-0.003484 \cdot d(x, y) - 2.9463$	[-19.0, -1.0]
	Zone 3	$-0.003484 \cdot d(x, y) - 10.4490$	[-19.0, -1.0]
Anisotropy	All Zones	0.0	[-0.5, 0.5]
Storativity	Zone 0	-5.0	[-5.5, -4.5]
	Zone 1	-4.0	[-6.0, -0.5]
	Zone 2	-1.5	[-2.5, -0.5]
	Zone 3	-5.0	Fixed
Recharge	Zone 1	-11.0	[-19.0, -1.0]

1.  $d(x, y)$  is Culebra overburden thickness

### TFIELD-5.2.7.2 Initial Head Field

Initial head values were created using a multivariate equation based on normalized  $x$  and  $y$  coordinates ( $-1 \leq \{x, y\} \leq +1$ ). The equation was designed to keep head along the northern boundary just above the measured head at SNL-1 and head along the southern boundary below the level measured at H-9c, and these constraints were the defining factors on the constants in the equation that follows. This process was done only once, and the result was used as a static input file for all calibrations. The creation of the field was done in MATLAB, using the following equations:

$$Z_{x,y} = 928.0 + 8.0 \left( y + \text{sign}(y) \sqrt{|y|} \right) + 1.2 \left( x^3 - x^2 - x \right) \quad (\text{TFIELD 5.2})$$

For values east of both the H2/M2 and H3/M3 boundaries, the ground-surface elevation was used as the initial head value. See Appendix A of Hart et al. (2009) for details. The resulting initial head field is shown in Figure TFIELD 5-9.



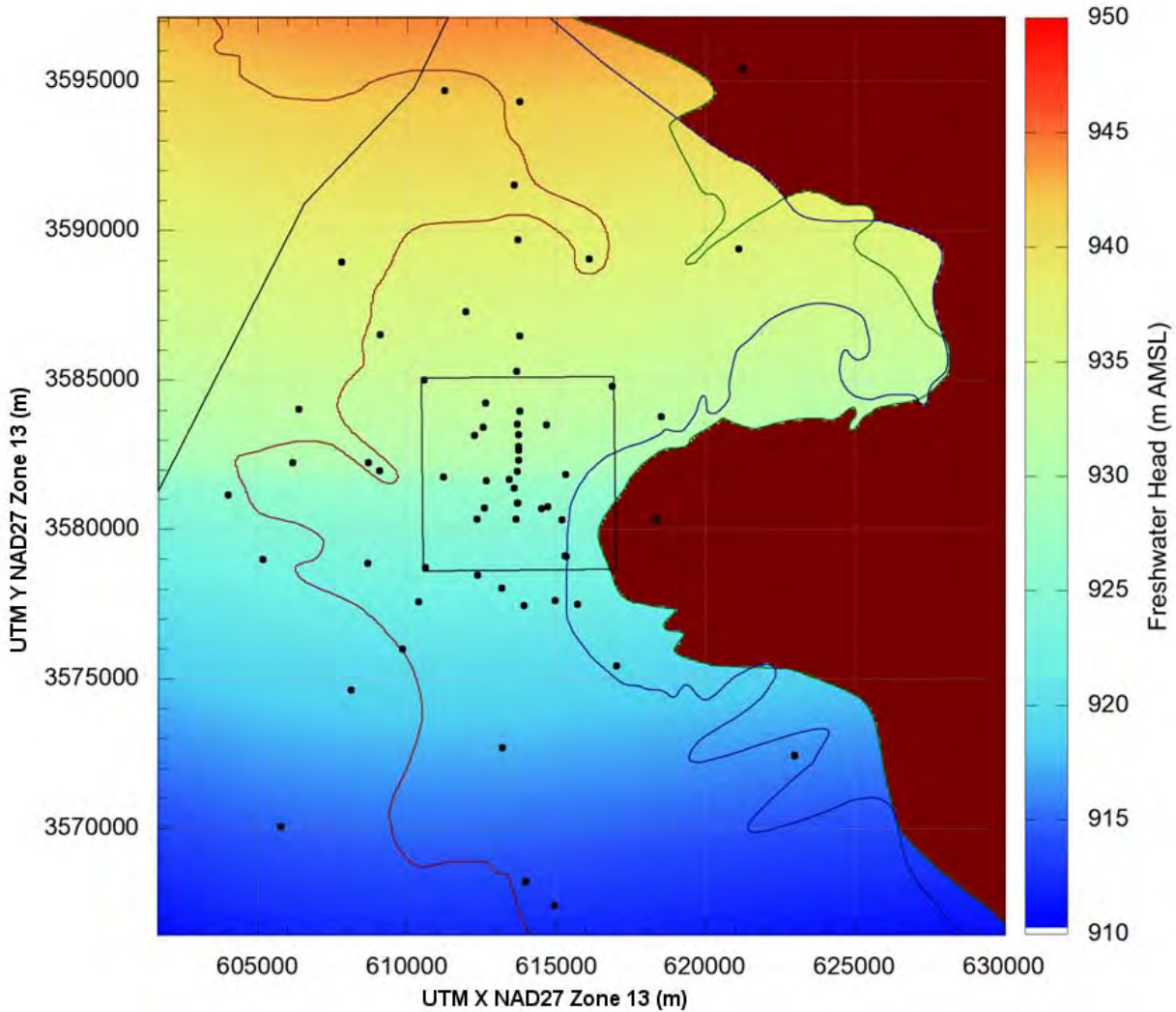


Figure TFIELD 5-9. Initial head values for use in MODFLOW steady-state solution. Brick red head values were fixed at the ground surface elevation (>1,000 m AMSL).

### TFIELD-5.2.8 Creation of Transmissivity Fields

Transmissivity fields are created from pilot points using kriging. Some pilot points are adjusted using PEST, while other pilot points are held fixed, because they correspond to estimated T values at wells with pumping tests. A variogram is needed to interpolate and extrapolate from the pilot points onto every element of the MODFLOW grid.

The transmissivity variogram (not an indicator kriging variogram, as was discussed in Section TFIELD-4.3) was created using transmissivity values estimated from well tests at 62 of the wells around the WIPP site. Wells outside the model domain and values at SNL-6 and SNL-15 were excluded from the calculation. The values at SNL-6 and SNL-15 are both several orders of magnitude lower than at the other wells, and are in a geologically distinct zone. While initial calculations showed that there was some statistical anisotropy, there were not sufficient measurements to create an anisotropic variogram. The complete steps for creating the variogram

are presented in Hart et al. (2009) Appendix B. The final parameters used are shown in Table TFIELD 5-4.

**Table TFIELD 5-4. Parameters for T model variogram, fitted to transmissivity data using an omnidirectional variogram with lag spacing of 1,500 m.**

Parameter	Value
Model Type	Exponential
Nugget	$0.02 (\log_{10} T)^2$
Sill	$1.95 (\log_{10} T)^2$
Range	9,500 meters

### TFIELD-5.2.9 Observations and Residuals

The observations (steady-state freshwater heads and pumping test drawdowns) used as calibration targets for PEST are summarized in Section TFIELD-5.1; residuals are calculated as the difference between measured and model-generated freshwater heads or drawdowns. The PEST utility program MOD2OBS is used to extract the observations from model output at times and locations associated with each steady and transient observation.

### TFIELD-5.2.10 MODFLOW Numerical Model

Inverse calibration requires a numerical model which generates results to compare against observed information. In this task, a MODFLOW 2000 (Harbaugh et al., 2000) flow model was developed for the Culebra that could use the base fields generated in Hart et al. (2008) as inputs. As was done in McKenna and Hart (2003), the Link Algebraic Multi-Grid (AMG) (Mehl, 2001) solver was used to increase speed and performance compared to other available solvers. In addition to transmissivity, it was decided to calibrate the local anisotropy, storativity, and some recharge as parameters in the calibration. Having these four parameters – T, A, S, and R – required a slightly more complex MODFLOW model implementation than was used in AP-088 (McKenna and Hart, 2003). Specifically, both storativity and anisotropy were single values previously, and changing these to cell-by-cell values required the use of the Layer Property Flow (LPF) package instead of the Block Centered Flow (BCF) package used previously. Using recharge also required the addition of the recharge package. For the known information, steady-state heads from 2007 and drawdown results from nine different pumping tests performed between 1985 and 2008 were used as the measured data. A conceptual diagram of the MODFLOW model with its inputs and outputs is shown in Figure TFIELD 5-10.

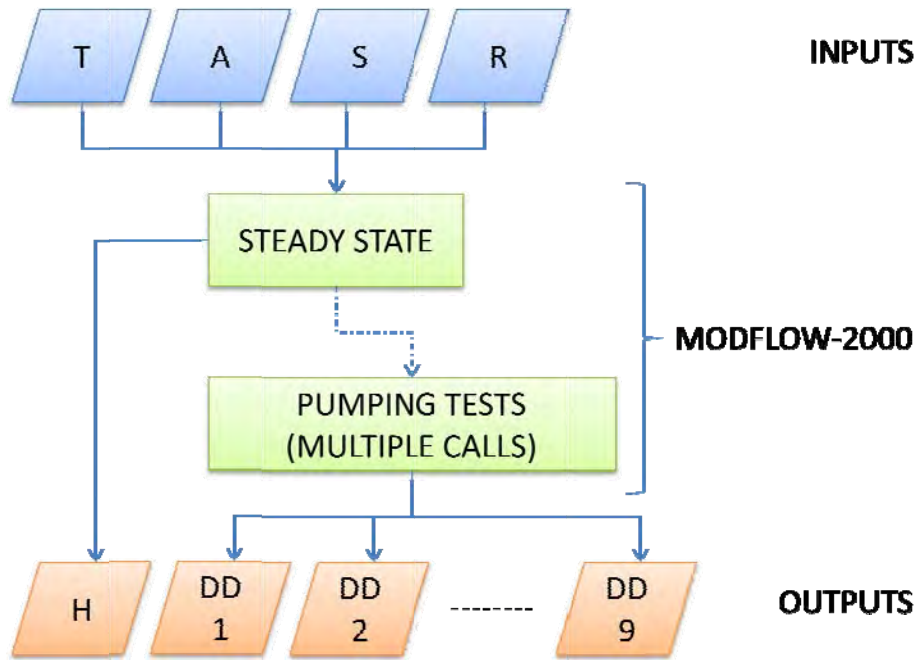


Figure TFIELD 5-10. Flow chart showing the numerical model used in the inverse calibration.

### ***TFIELD-5.3 Step 2 – Inverse Calibration Process***

The inverse calibration process used multiple forward calls to evaluate the impact that perturbing an input parameter has on model predictions at locations and times corresponding to observations. This process was computationally intensive, and involved 80 processors on two different computing clusters running for six months to calibrate 200 fields.

#### **TFIELD-5.3.1 PEST Calibration Process**

The inverse calibration process was done using the PEST inverse software suite and its groundwater utilities. The steps involved in each forward model run during the PEST calibration are illustrated in Figure TFIELD 5-11; the complete calibration process is shown in Figure TFIELD 5-12.

The completed PEST "model" that was calibrated included the creation of the fields from the kriging factors and pilot points (PPK2FAC, FAC2REAL, REAL2MOD), the MODFLOW calls, and finally the observation extraction utilities (MOD2OBS and OBS2REAL) which extract modeled cell head or drawdown values from a binary MODFLOW output file. For SVD iterations, another preprocessor, PARCALC, is used to create the pilot point values from the super parameters. The model script, `model.sh`, the REAL2MOD script and the OBS2REAL script were written for this task, and are included in Appendix G of Hart et al. (2009). PPK2FAC, FAC2REAL, and MOD2OBS are utilities in the PEST program suite.

The first call to the PEST program was a single iteration to estimate the Jacobian matrix. This required over 1,100 forward model calls, one for each variable parameter value. Once the Jacobian matrix was calculated, the SVDAPREP program decomposed the Jacobian matrix into eigenvectors and kept these super parameters that corresponded to the largest singular values. The result was a set of 100 to 300 super parameters that were then used with a 50-iteration PEST calibration. The termination criteria were: a maximum of 50 iterations, 3 successive iterations without an improvement in the objective function, or a relative decrease of less than 0.001 in the objective function for 3 iterations. Once termination criteria had been reached, the PEST program would output the best parameters to a file. This file was then used to create one final PEST control file which issued a single model run with the best parameters as input. The results of this final call were then used to calculate the measures of fit and the final fields.

The run control details regarding the calibration process are presented in Appendix G of Hart et al. (2009). Using the ReadScript.py run control system allowed automatic check-out of input files, execution, and check-in of the results to CVS following calibration.

**Figure TFIELD 5-11. The PEST calibration process.**

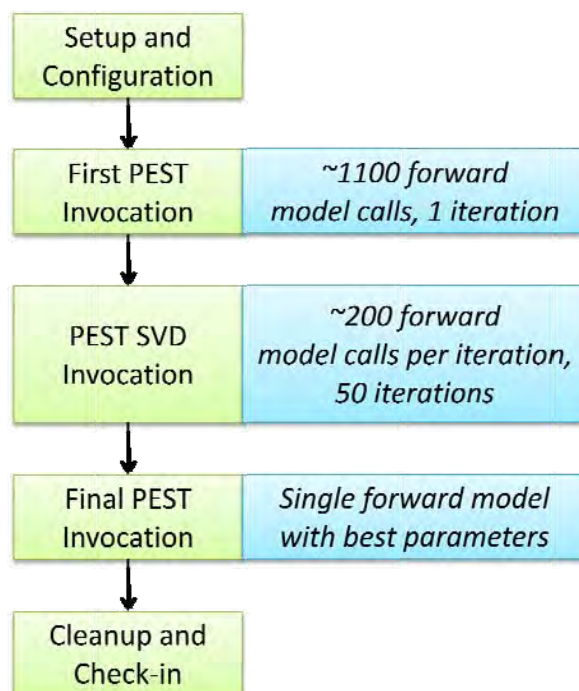


Figure TFIELD 5-12. Complete calibration process for a single field.

### TFIELD-5.3.2 Calibrated Correction of Steady-State Head Values

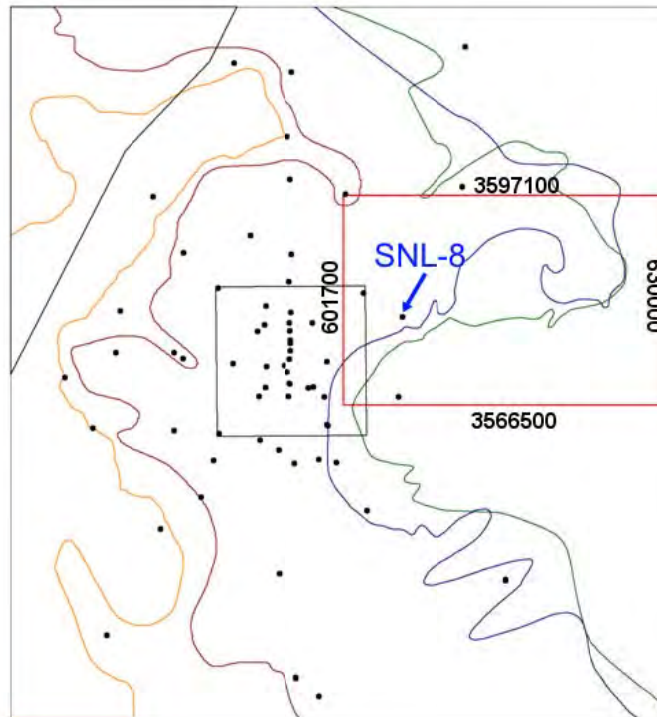
Because some of the original steady-state calibration targets were incorrect, the fields that had already been calibrated to the incorrect data needed to be re-calibrated to the new data. The two wells with the most significant changes, ERDA-9 and SNL-8, had more than one meter change from the old to new values. The ERDA-9 head was in some ways an expected change, because the calibrations had consistently been unable to match the old head value, which was too low compared to the higher corrected value. Without any re-calibration, correcting the value for ERDA-9 produced better model fits.

#### TFIELD-5.3.2.1 Localized Recalibration in the Vicinity of SNL-8

The new calibration target for SNL-8 was based on a recalculation of the freshwater head (Johnson, 2009). Because SNL-8 was not an observation well in any of the transient pumping tests, and because it was to the east and up-gradient from the WIPP LWB, only a section of the fields were recalibrated to correct for the change in the calibration target at SNL-8. It was hoped that this would allow the T, S, A and R fields to change to match the SNL-8 head without requiring the week-long re-calibration for each of the affected fields if the entire domain was recalibrated.

The recalibration process involved fixing all the parameters that had previously been calibrated, except for those parameters in a rectangular area around and up-gradient from SNL-8. The complete area definition was 14 km east-west by 9 km north-south with the southwest corner at 616000 m Easting, 3580000 m Northing UTM NAD27 and is shown in red on Figure TFIELD 5-13. All other aspects of the inverse calibration, including the forward model and the SVD assist

process, were left the same. The resulting fields had significantly better fits to the steady-state heads, and little impact was seen on the transient test results.



**Figure TFIELD 5-13. Recalibration boundary shown in red to the northeast of the WIPP site. Recalibration boundary limits are UTM X and Y NAD27 Zone 13 (m).**

### **TFIELD-5.3.2.2 Continued Recalibration Activity**

After examination of the acceptance criteria (discussed in the next section), some fields were recalibrated again, using the same recalibration process but holding none of the parameter values fixed at previously calculated values. This process essentially added some additional calibration iterations to these fields. This was only done on a few fields that were now completely within the acceptance criteria for steady-state heads, and just outside the acceptance criteria for transient tests. The intent of this additional calibration was to increase the quality of the transient fits to get a total of 100 fields that met both the steady-state and transient calibration requirements. This secondary re-calibration process was continued until 100 fields were obtained that met the requirements, and it did not always improve fits (i.e., in some cases the fields were already as fully calibrated as was possible given the number of pilot points and observations and initial conditions).

### **TFIELD-5.3.3 Evaluation of Impact of Multiple Calibration Processes**

Because some fields were calibrated only once (set B: 50 fields following correction of the steady-state values), some fields were calibrated once and then underwent a localized recalibration (set A: the 150 first fields calibrated), and some fields even underwent a second round of calibration (set

C: 15 fields), we evaluated the impact this may have had on the final selection of fields. The list of fields, and the set they belong to, is presented in Appendix E of Hart et al. (2009).

Because the final selection process did not look at which set of fields the results were taken from, the mix of fields should be similar to a random selection if the calibration processes were producing equivalent results. The random selection of fields from set B can be modeled as a binomial distribution with the  $p$ -value of 0.25 and  $n = 100$ . If the results are within the 95% confidence interval for a random selection of fields, then there should be between 17 and 33 fields selected from the set B. The final results used 83 fields from the set A and C, and the remaining 17 were selected from set B. This is within the confidence interval, so it is concluded that the different processes had no impact on the selection of the final fields. The selection of fields from set C versus those from set A can be modeled the same way, with a  $p$ -value of 0.10 and  $n = 83$ . The final selection included 10 from set C which is within the confidence interval of 3 to 13 fields, and again the calibration process did not impact the field selection.

Because this mix of final fields is acceptable and came strictly from the cutoff values, and not from any deliberate attempt to select from one group or another, all 100 fields meeting the acceptance criteria are equally good and equally probable representations of the Culebra. Furthermore, no one calibration procedure is inherently better than any other, provided that the same acceptance criteria are met, so the use of different procedures may actually improve the representation of uncertainty in the final results.

#### **TFIELD-5.3.4 Selection of Best-Calibrated Fields**

The selection criteria for the "best" calibrated fields consisted of comparing the absolute average error of the modeled steady-state heads to a cutoff value, and comparing the absolute average error of the modeled transient responses to a cutoff value. The steady-state and transient criteria were evaluated separately, and only fields that were less than the cutoff value for both sets of tests were selected as the final fields. The final cutoff values used were the mean value of the errors taken across all 200 fields, and they are presented in Table TFIELD 5-5. Using the mean values resulted in a set of 102 fields, so the two fields with the largest sum of the two metrics were discarded. In Figure TFIELD 5-14, the sum of the steady-state average errors was graphed against the sum of the transient pumping tests' average errors, and the selected and unselected fields are shown. The trend line shows graphically how PEST allows tradeoffs while keeping the improvement in errors as balanced as possible. The final fields IDs are presented in Table TFIELD 5-6.

**Table TFIELD 5-5. Cutoff values for final field selection.**

<b>Test Type</b>	<b>Average Error Selection Cutoff</b>
Steady State	0.699 m
Transient Pumping Response	0.164 m

**Table TFIELD 5-6. Final selected field identifiers.**

r001	r055	r207	r652
r002	r058	r256	r655
r004	r059	r260	r657
r006	r060	r273	r664
r007	r061	r276	r669
r009	r064	r279	r694
r010	r070	r298	r707
r012	r073	r327	r727
r013	r074	r328	r752
r017	r076	r361	r791
r024	r078	r431	r806
r027	r082	r440	r808
r028	r083	r465	r809
r029	r084	r486	r814
r032	r090	r489	r823
r034	r092	r506	r861
r037	r095	r508	r883
r038	r097	r511	r902
r040	r098	r515	r910
r041	r102	r522	r921
r045	r104	r568	r922
r051	r137	r571	r940
r052	r142	r631	r981
r053	r191	r634	r982
r054	r203	r640	r984



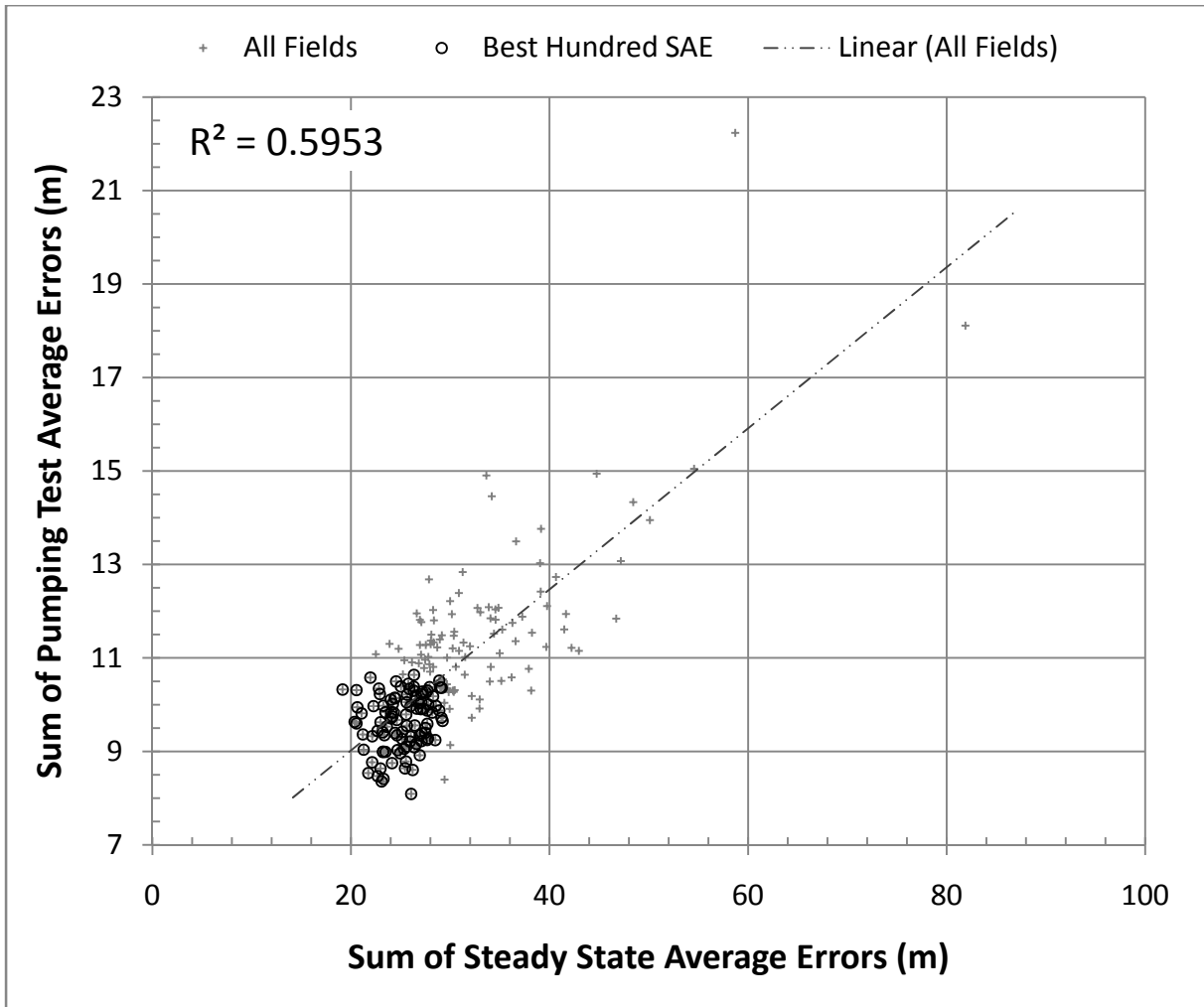


Figure TFIELD 5-14. Selection of best fields from all fields - graph of steady-state errors vs. pumping test errors.

### ***TFIELD-5.4 Step 3 – Post-Calibration Analysis***

The post-calibration analysis consisted of performing analyses on the selected fields, and examining the calibrated forward model outputs. The full results of the steady-state forward model outputs are presented in Appendix C of AP-114 Task 7 (Hart et al., 2009), pumping test results are presented in Appendix D and tabular results are presented in Appendix E of the same report.

#### **TFIELD-5.4.1 Statistical Analysis of Resulting T, A, and S Fields**

Plots of mean and standard deviations of the final 100 fields are given in Section TFIELD-5.4.1.1. The bulk transmissivity of the final calibrated fields are also compared to the bulk transmissivity of the base fields, using membership in the high or low T categories. Similarly, Section TFIELD-5.4.1.2 and TFIELD-5.4.1.3 show summary statistics regarding the calibrated storativity and recharge fields, respectively.

### TFIELD-5.4.1.1 Final Transmissivity and Anisotropy Fields

The transmissivity values presented in this section are the effective transmissivity values, which include the effects of anisotropy. Effective transmissivity was calculated as

$$\log_{10} T_e = \log_{10} T_{EW} + \frac{1}{2} \log_{10} A \quad (\text{TFIELD 5.3})$$

which is the average of  $\log_{10}T$  in the north-south and east-west directions. See Equation TFIELD 5.1 in Section TFIELD-5.2.1.2. The bulk transmissivity, which is the average  $\log_{10}$  transmissivity value of all cells in a given zone or zones, was calculated for the central and Salado dissolution zones (zones 0-2) and compared to the bulk transmissivity of the same zones from the base fields. The eastern, very low transmissivity zone (zone 3) was compared separately. The bulk transmissivity values are shown in Table TFIELD 5-7. The mean effective transmissivity and the standard deviation of transmissivity are presented in map form in Figure TFIELD 5-15 and Figure TFIELD 5-16. The mean effective transmissivity map does not show the very low T zone east of the halite margins in order to keep the figure colormap sufficiently distinct for the area around the WIPP site.

Because pilot point parameter values were essentially unconstrained for T, some areas in zones 0 and 1 could change from a low-T zone into the range generally considered high-T and vice versa. The defining value for high-T was set in AP-114 Task 5 (Hart et al., 2008) to be the bulk transmissivity value of the base fields:  $-5.41 \log_{10} m^2/s$ . At each cell, the number of fields whose initial and final T values were in the high-T zone was calculated, and the maps of those numbers for the base and calibrated fields are presented in Figure TFIELD 5-17 and Figure TFIELD 5-18, respectively. The total number of fields where transmissivity "changed zones" is represented graphically in Figure TFIELD 5-19 and Figure TFIELD 5-20. In Figure TFIELD 5-19 and Figure TFIELD 5-20, the white regions define the areas where the original T values were "low" or "high," respectively, and could not or did not make the specified change. The two measures shown in these sets of maps provide an indication of how the geologically based conceptual model used to create the base fields was altered by the steady-state and transient hydraulic information.

**Table TFIELD 5-7. Bulk  $\log_{10}$  transmissivity values comparison.**

Base field bulk $\log_{10}$ transmissivity (Zones 0-2)	$-5.41 \log_{10}(m^2/s)$
Calibrated field bulk $\log_{10}$ transmissivity (Zones 0-2)	$-5.02 \log_{10}(m^2/s)$
Base field bulk $\log_{10}$ transmissivity (Zone 3)	$-11.74 \log_{10}(m^2/s)$
Calibrated field bulk $\log_{10}$ transmissivity (Zone 3)	$-10.47 \log_{10}(m^2/s)$

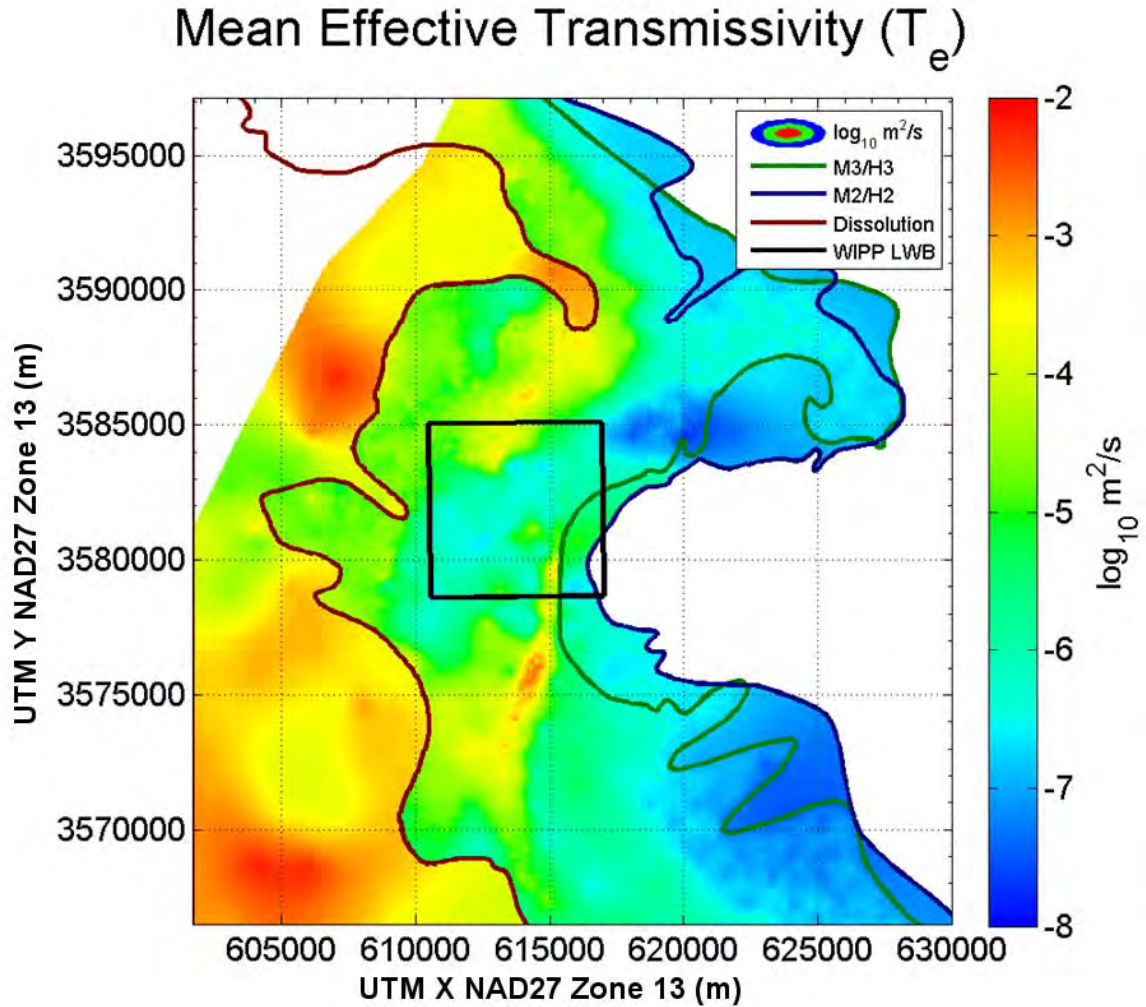


Figure TFIELD 5-15. Mean effective transmissivity for zones 0-2 across the 100 final selected fields.

# Standard Deviation of Effective Transmissivity ( $T_e$ )

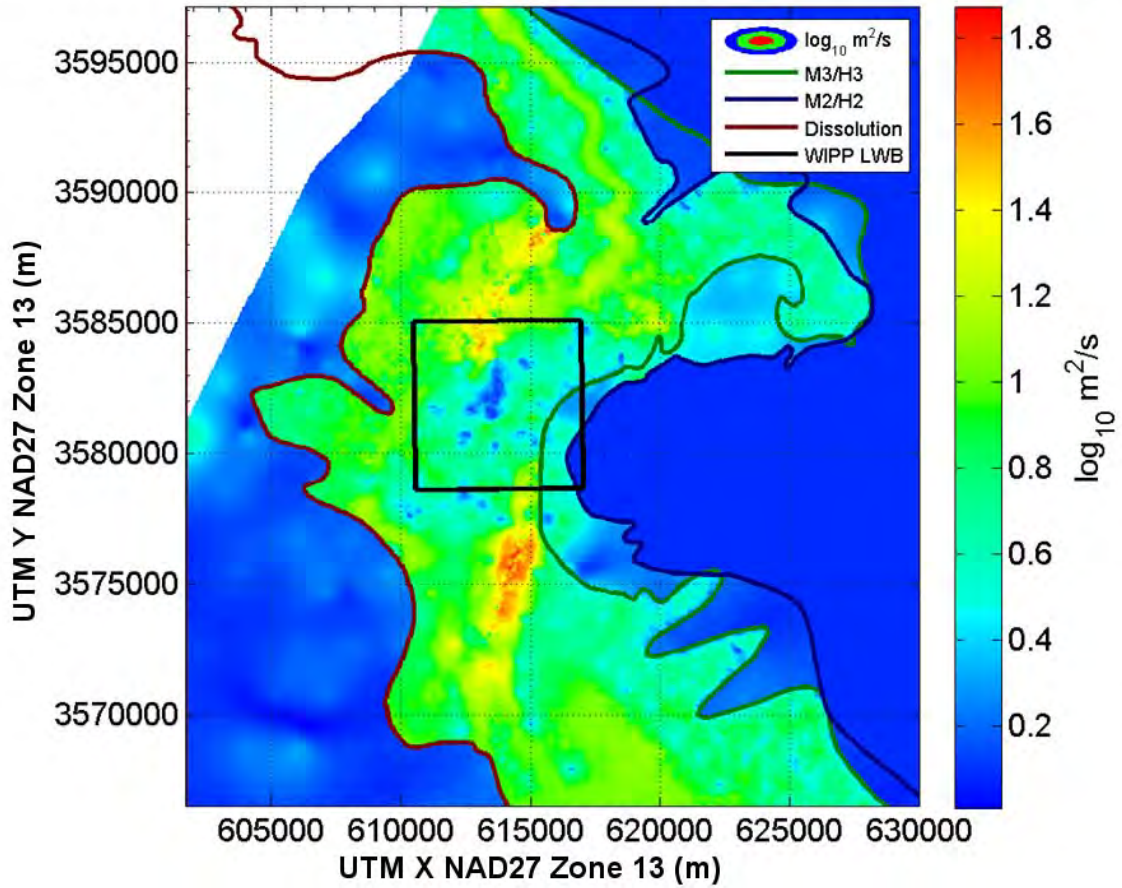


Figure TFIELD 5-16. Standard deviation of effective transmissivity for all zones across the 100 final selected fields.

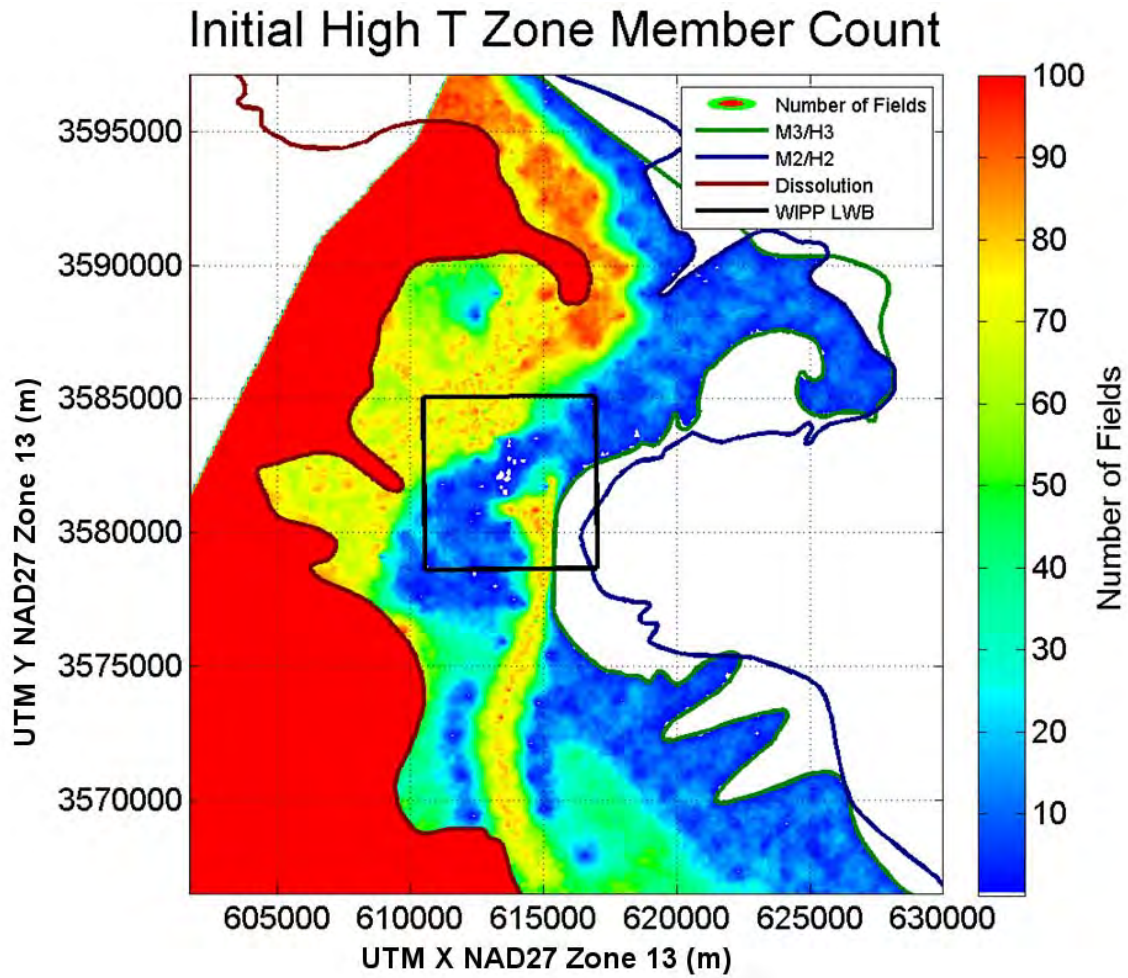


Figure TFIELD 5-17. High-T zone membership calculated for the base T values.

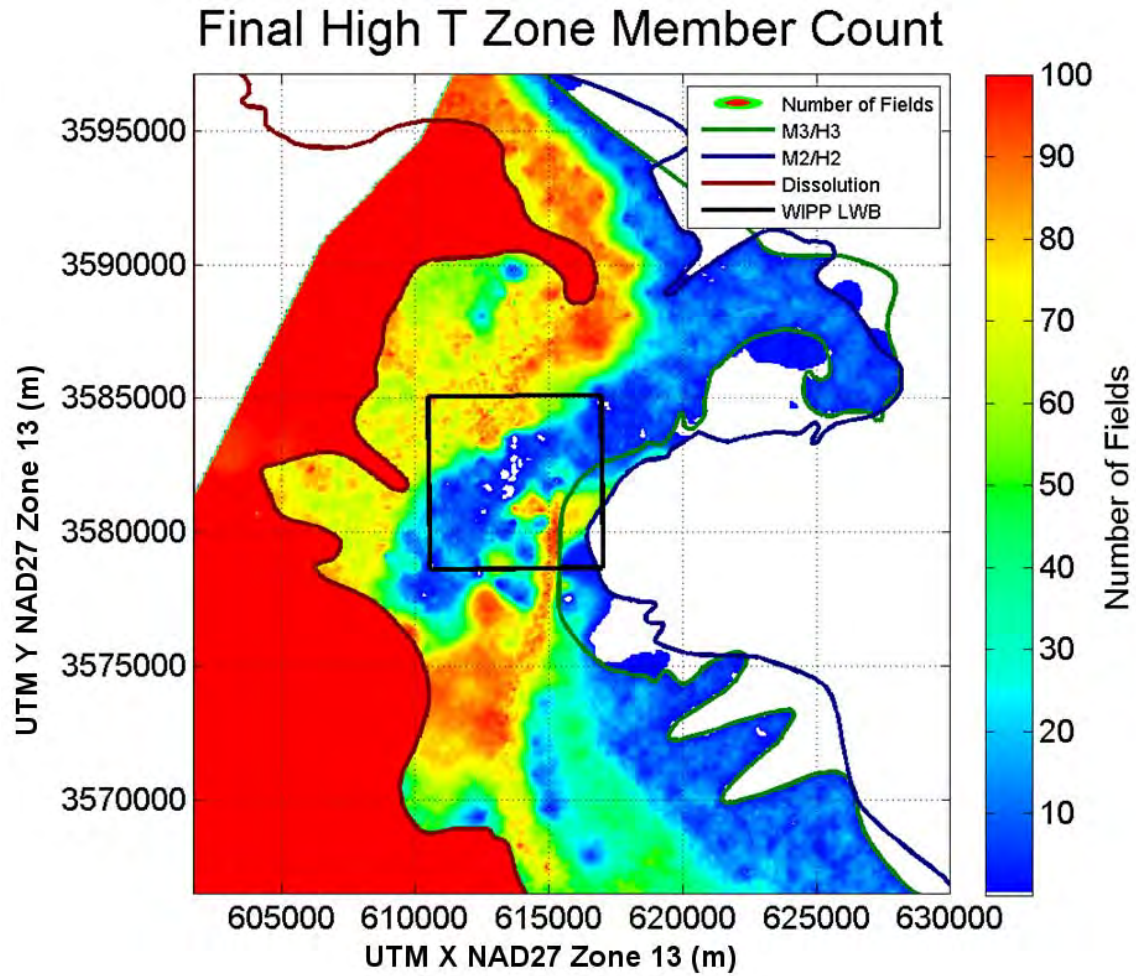


Figure TFIELD 5-18. High-T zone membership, calculated for the calibrated T values.

### Cell Changed from Low T to High T

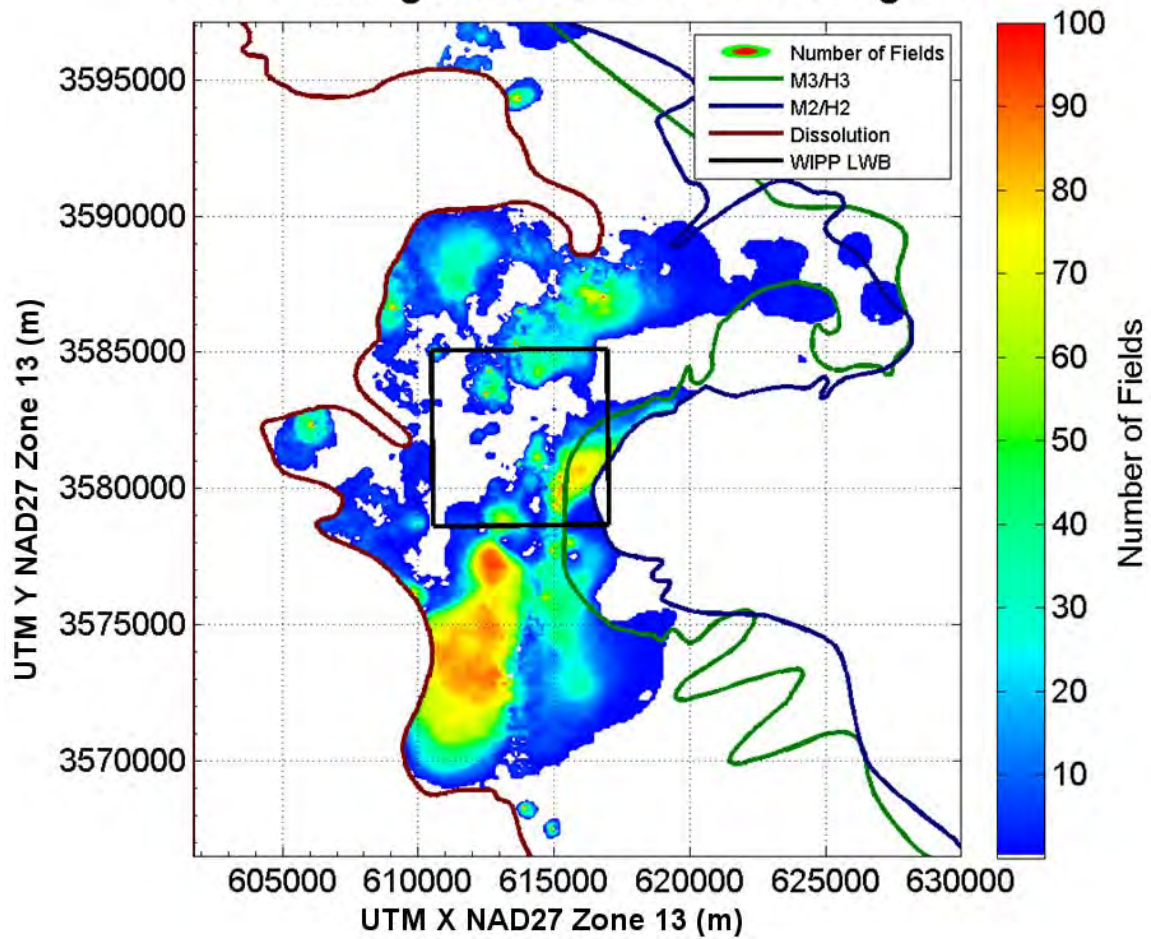


Figure TFIELD 5-19. Number of fields where low-T became high-T.

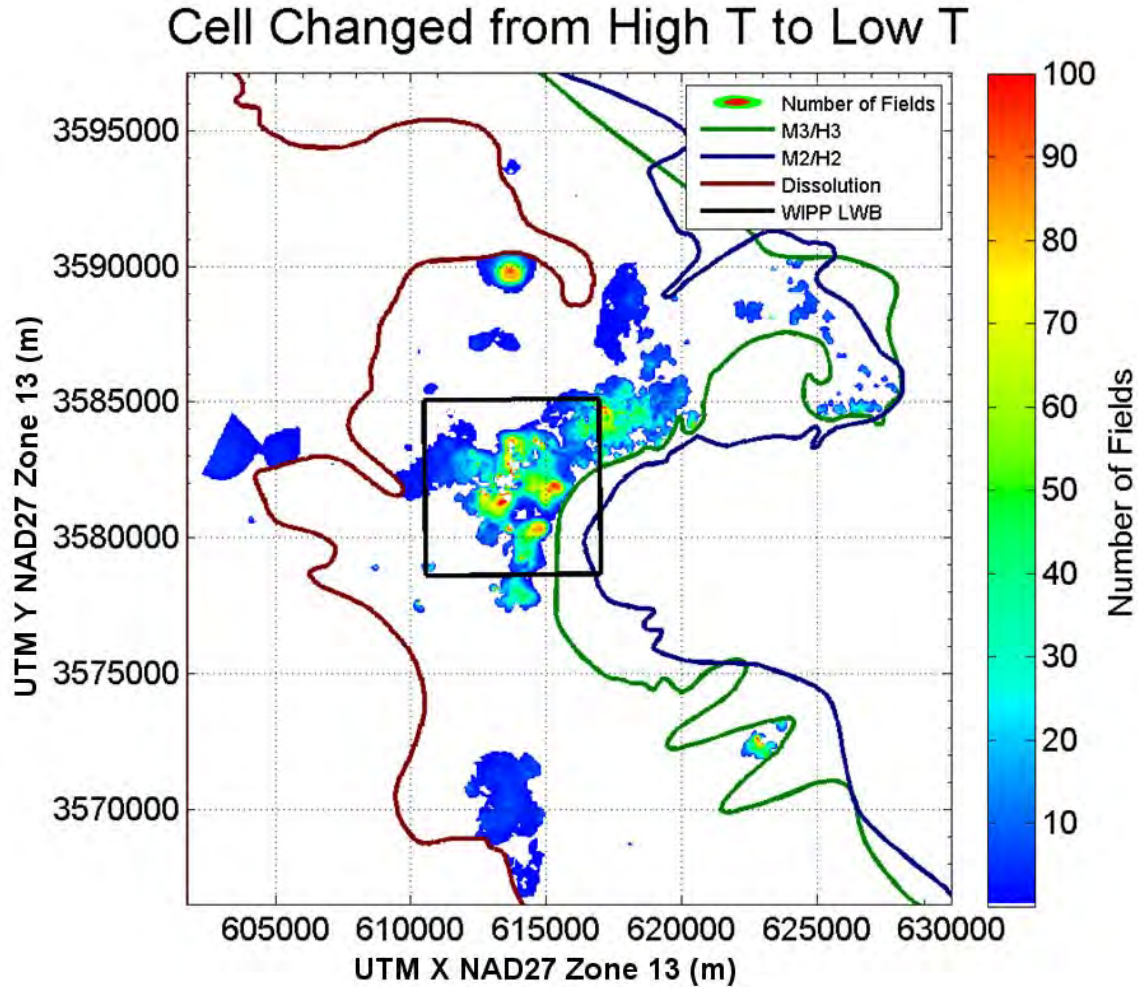


Figure TFIELD 5-20. Number of fields where high T became low T.

#### TFIELD-5.4.1.2 Final Storativity Values

The mean and standard deviation of the final storativity values are presented in Figure TFIELD 5-21 and Figure TFIELD 5-22. The mean storativity values indicate that the overall storativity values in the confined and transitional zones did not change much from their initial values, however the area northwest of P-14 shows high variability in the storativity values used in individual solutions Figure TFIELD 5-22. This may have some relation to the relatively poorer fits of the transient data for the WIPP-25 response to the P-14 pumping test in the model.



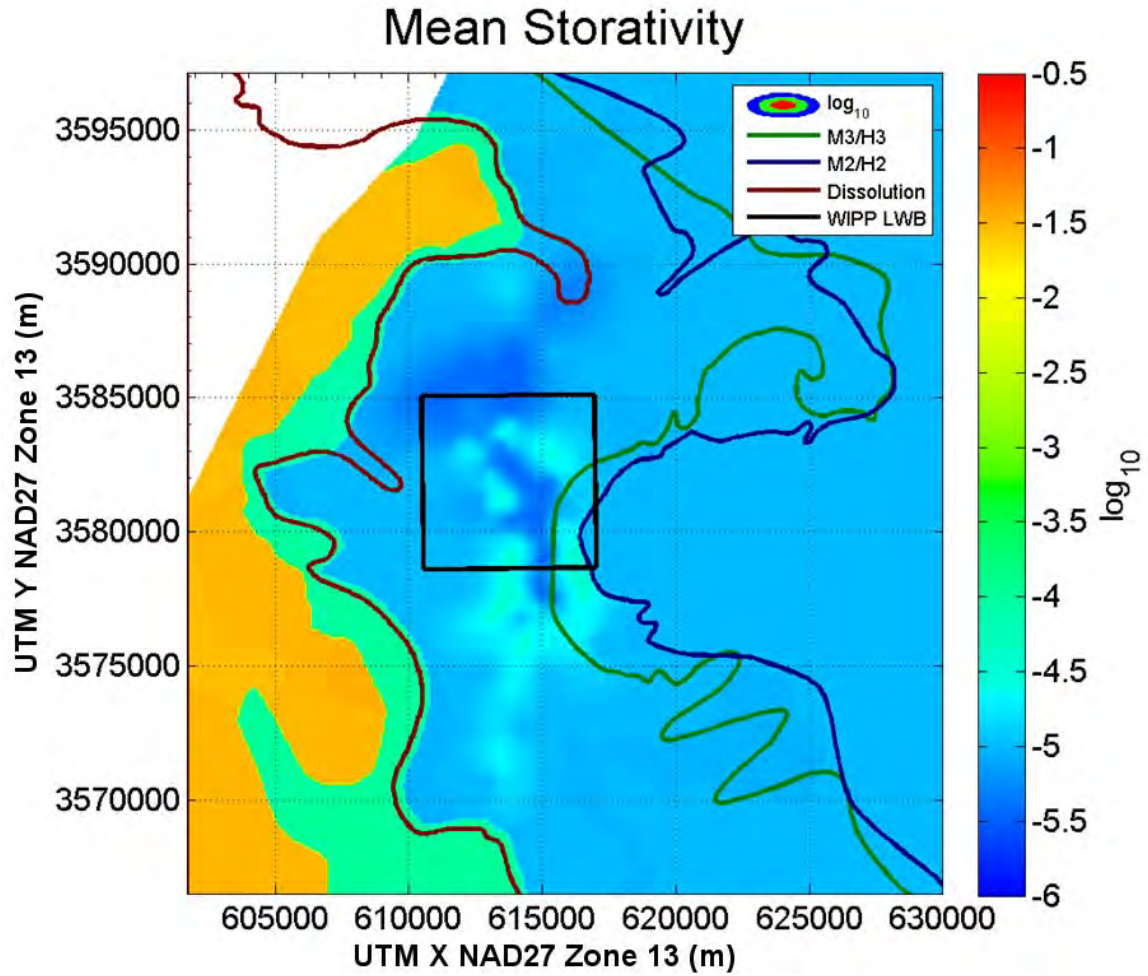


Figure TFIELD 5-21. Mean storativity values across the 100 final calibrated fields. Values in zone 3 (halite-bounded) are non-zero due to an applied shifting term.

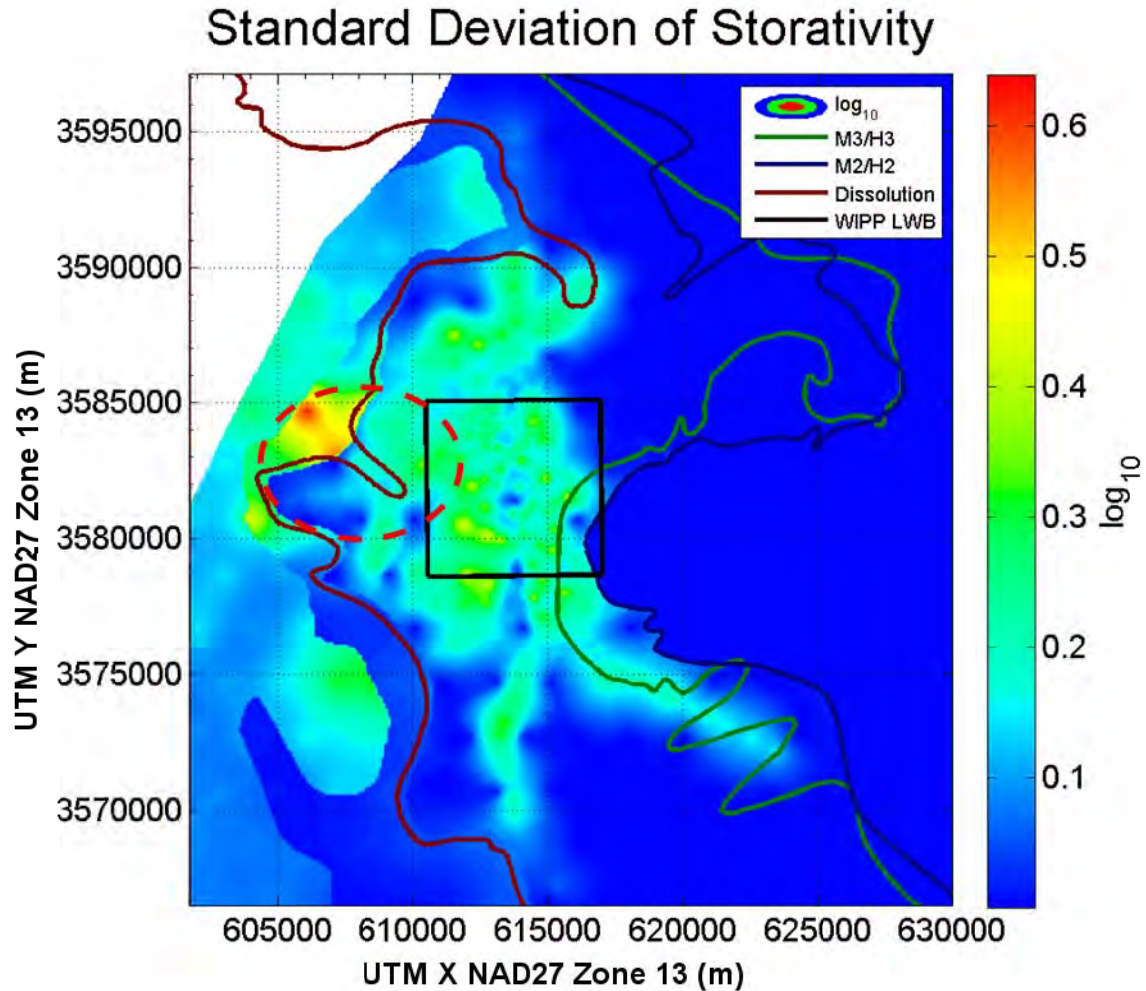


Figure TFIELD 5-22. Standard deviation of storativity values across the 100 final calibrated fields. Red oval shows P-14 to WIPP-25 area of influence. Values in zone 3 (halite-bounded) are non-zero due to an applied shifting term.

### TFIELD-5.4.1.3 Final Recharge Values

The final recharge values were all less than the initial values of  $10^{-11}$  m/s ( $3.2 \times 10^{-4}$  m/yr). Compared to the other parameters, there was very little change in recharge. Because the recharge zone was linear, in addition to the cell-by-cell mapping, a view of the average, minimum and maximum recharge values, in meters per year, is shown as a cross section in the cross-direction (across a row) as if looking from the south to the north through the domain in Figure TFIELD 5-23.

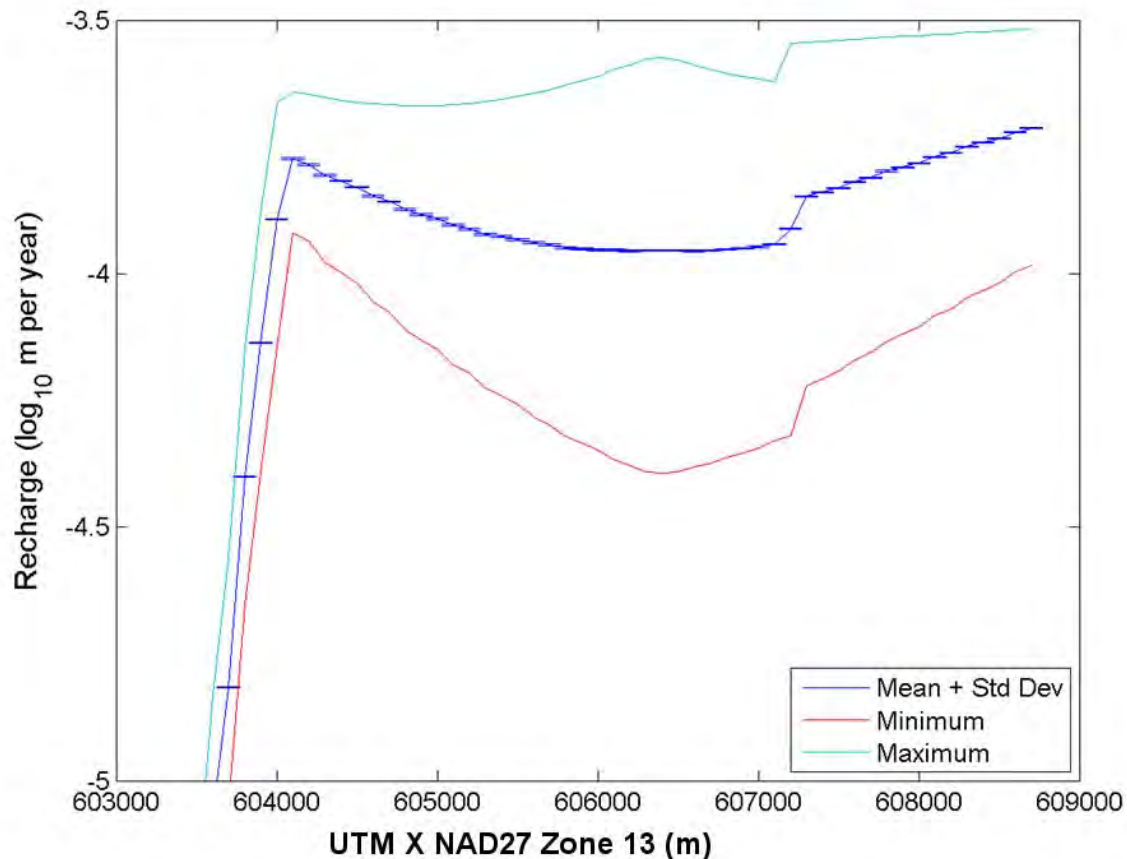


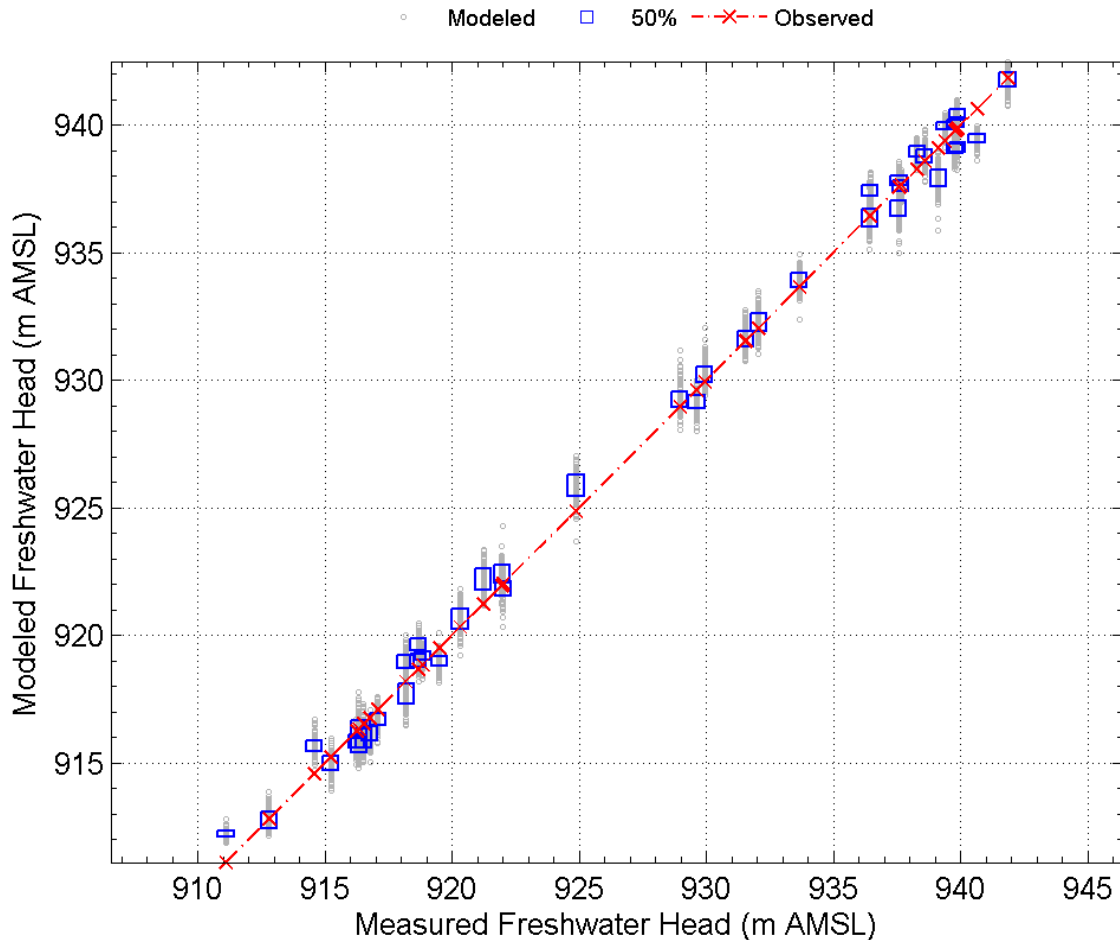
Figure TFIELD 5-23. Recharge as viewed through columns from the south. The initial value was set at  $10^{-3.5}$  m/year. The sharp dropoff to the west is the transition to the single fixed-recharge point of  $10^{-11.5}$  m/year (interpreted as zero by REAL2MOD).

#### TFIELD-5.4.2 Forward Model Results using the Calibrated Fields

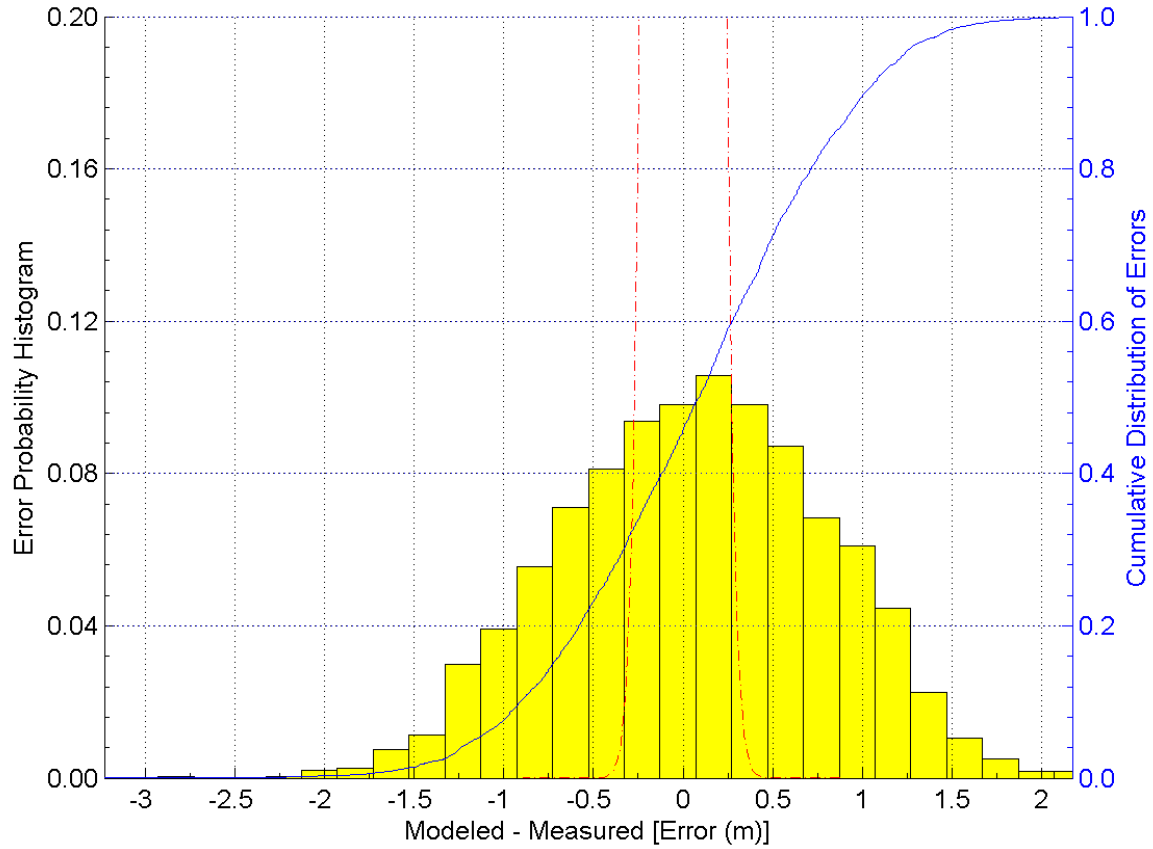
The two main divisions of the results are the steady-state head results and the pumping test results. The results presented here only represent the 100 final selected fields, and therefore the maximum error is limited by the selection criteria described in Section TFIELD-5.3.4: an average steady-state error of less than 0.700 m and an average pumping test observation error of less than 0.164 m.

Figure TFIELD 5-24 shows the modeled steady-state head values plotted against the measured head values. The one-to-one correspondence line shows the ideal match, and the modeled results are presented as box-and-whisker plots at each observation well. Figure TFIELD 5-25 shows all the head errors for all 100 fields as a histogram of error values for steady-state head. Additional figures and tables are presented in Appendix C of (Hart et al., 2009). The estimated measurement error can be modeled as a zero-mean Gaussian distribution with a standard deviation of 0.10 m (McKenna and Wahi, 2006). The measurement error distribution curve is included in Figure TFIELD 5-25.

Graphs for each of the transient pumping test results are presented in Appendix D of (Hart et al., 2009). The average error of the final fields ranged from 0.12 m to 0.164 m across all tests, with an average error of 0.15 m. The maximum error for a single observation well ranged from 0.005 m to 2.5 m, with an average of 0.36 m as the maximum error at a given observation well.



**Figure TFIELD 5-24. Results for 42 of the 44 total steady-state head measurements for the 100 selected fields. Observed heads are red X's along the diagonal line. Wells SNL-6 and SNL-15 are not included because they are located in the fixed-head region of the model.**



**Figure TFIELD 5-25. Histogram of steady-state head errors for the 100 selected fields (not including wells SNL-6 and SNL-15). Red dashed line is the  $\pm 3\sigma$  section of the measurement error PDF. The slight skew to right is an artifact of the binning.**

## **TFIELD-6 Culebra T-Field Mining Modifications**

The work described in section TFIELD-6 was completed under AP-144 Analysis Plan for the Calculation of Culebra Flow and Transport for CRA2009PABC (Kuhlman, 2009).

### ***TFIELD-6.1 Overview***

The PABC-2009 Culebra T-field mining modifications flow-field calculations largely follow the procedure used in the PABC-2004 (Lowry and Kanney, 2005), with two exceptions: 1) a new definition of the region containing minable potash is used, and 2) the new T-fields in Sections TFIELD-3 through TFIELD-5 are used as inputs. The procedure for the mining modification portion of the analysis is summarized below:

1. Obtain the sampled values for the random mining modification factor (100 vectors  $\times$  3 replicates);
2. Map potential areas of future potash mining onto the groundwater modeling domain for both full- and partial-mining scenarios;
3. Apply the mining modification factor to the 100 stochastically calibrated T-fields from AP-114 Task 7 (Hart et al., 2009), producing 600 mining-modified T-fields (100 vectors  $\times$  2 mining scenarios  $\times$  3 replicates);
4. Perform steady-state flow simulations for each of the 600 mining-modified T-fields using MODFLOW-2000 (also known as MODFLOW or MF2K); and
5. Perform particle tracking using the new mining-affected flow-fields to determine advective travel times to the LWB.

This analysis report represents the latest effort in characterizing mining effects in the Culebra and highlights the differences and additions relative to past calculations (Ramsey and Wallace, 1996; Lowry, 2003a; 2003b; Lowry, 2004). The reader is encouraged to review the past documents for further background information.

The PABC-2004 models two categories of mining-impacted transmissivity fields: partial mining with only mining outside the LWB and full mining with regions both inside and outside the LWB mined.

Starting with the 100 stochastically calibrated T-fields from Section TFIELD-5, T-fields are modified to reflect the effects of mining by multiplying the transmissivity value in cells that lie within designated mining zones by a random factor uniformly sampled between 1 and 1000. The range of this factor is set by the EPA in regulation 40 CFR 194.32(b) (U.S. EPA, 1996). The scaling factor for each T-field is provided from Latin Hypercube Sampling (LHS), (Kirchner, 2010).

A forward steady-state flow simulation is run for each new T-field under each mining scenario (full and partial) across three replicates of mining factors, resulting in 600 simulations. Particle tracking is performed on both the 100 original and 600 modified flow-fields to compare the flow path and

groundwater travel time from a point above the center of the WIPP disposal panels to the LWB. CDFs are produced for each mining scenario and compared to the undisturbed scenario. The CDFs describe the probability of a conservative tracer (i.e., a marked water particle) reaching the LWB at a given time. In addition to comparing travel times, particle-tracking directions are also examined to determine the effect on the regional flow direction in the WIPP area due to mining.

Potash mining in the region surrounding WIPP involves underground excavation in the McNutt Potash zone of the upper Salado Formation, which is located stratigraphically above the WIPP repository horizon, but below the Culebra Member of the Rustler Formation (see Figure TFIELD 2-2). It is hypothesized that subsidence due to collapse of the underground voids created in the McNutt potash zone during mining will lead to increased permeability in the Rustler Formation, due to increased fracturing. The purpose of the mining scenario calculations is to determine the impact of potash mining on groundwater flow directions and transport velocities in the Culebra. This analysis largely represents a re-application of the methods used in PABC-2004 (Lowry and Kanney, 2005), with a few minor exceptions:

1. The definition of the regions where minable potash is believed to exist, obtained from the Bureau of Land Management (BLM) (Cranston, 2009), has been updated.
2. The configuration of the MODFLOW model that mining modifications are being applied to has changed (see Sections TFIELD-3 through TFIELD-5).
3. The way the mining-modified areas interact with internal boundary conditions of the flow model has changed, due to the change in the boundary conditions (there were no internal boundary conditions in the PABC-2004 MODFLOW model).

## ***TFIELD-6.2 Model Domain, Boundary, and Initial Conditions***

The eastern limit of the MODFLOW model domain used in the PABC-2009 analysis (Hart et al., 2008) is extended eastward, compared to the MODFLOW domain used in the PABC-2004 analysis. This change was made in order to locate the boundary in an area where halite is present in all of the non-dolomite members of the Rustler Formation, simplifying the specification of the eastern model boundary condition. The new extent of the model domain is 601700 m to 630000 m  $x$  and 3566500 m to 3597100 m  $y$ . The MODFLOW flow model domain is aligned with the primary compass directions and is aerially discretized into 100 m square cells, yielding a model that is 284 cells or 28.4 km wide (east-west) by 307 cells or 30.7 km tall (north-south). The Culebra is modeled as a single horizontal layer of uniform 7.75 m vertical thickness.

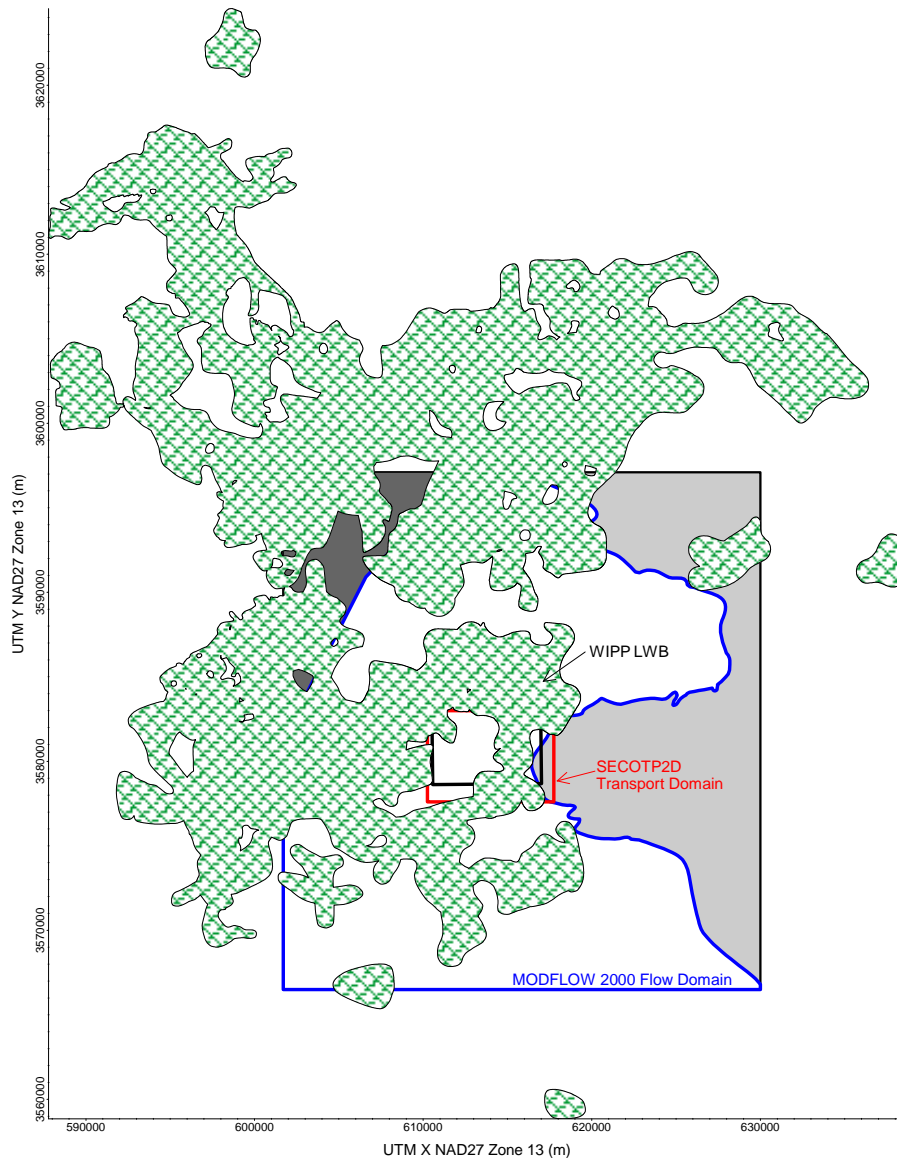
## TFIELD-6.2.1      **Boundary and Initial Conditions**

Like the model domain and discretization, the boundary and initial conditions used in the PABC-2009 are described fully in AP-114 Task 7 (Hart et al., 2009). Regional flow rates within the flow model are controlled by the boundary conditions and the hydraulic conductivity distribution. The regional gradient across the domain is approximately

$$(943.9 \text{ m} - 911.6 \text{ m})/30.7 \text{ km} = 0.00105 \quad (\text{TFIELD 6.1})$$

For the current grid, we average the constant heads along the non-halite-sandwiched portion of the northern boundary (columns 1-140, 943.9 m), subtract the average heads along the entire southern boundary (911.6 m), and then divide by the north-south model domain distance (30.7 km). It is assumed that mining impacts would not significantly change this regional gradient and thus the specified initial conditions for the mining scenarios are identical to those in AP-114 Task 7 (Hart et al., 2009). In addition, the CCA, CRA-2004, and PABC-2004 all used this same conceptualization (keeping the outer boundary conditions fixed between the mining and non-mining scenarios); the same conceptualization is maintained to allow for comparisons between the different models.





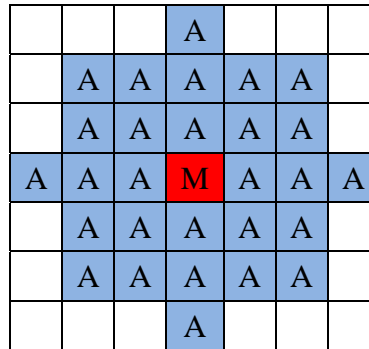
**Figure TFIELD 6-1. Comparison of minable potash to the flow and transport modeling domains; green hatched area from BLM shapefile (Cranston, 2009)**

### **TFIELD-6.2.2 Determination of Potential Mining Areas**

The 2009 version of the Bureau of Land Management (BLM) map indicating the distribution of minable potash ore was obtained from BLM as an ESRI shapefile (Cranston, 2009). The conversion of this shapefile to an integer matrix corresponding to Culebra MODFLOW model cells (indicating whether a model cell was affected by mining or not) is explained in Appendix 1 of Kuhlman (2010).

Since the potash-mining horizon is located in the Salado Formation, below the Culebra, the areas disturbed by mining activities in the Culebra are larger than mined areas in the Salado due to angle-of-draw effects; the subsidence effects do not propagate up vertically, but instead they propagate up

and out at 45° angles between horizontal and vertical. The final conclusion is that a 253-m-wide collar was to be added to the mining-impacted areas (Ramsey and Wallace, 1996; Bertram, 1995). This is considered a conservative estimate of the angle-of-draw effects. To accommodate the angle of draw, the mining zone boundaries, as overlaid on the current model grid, were extended outward three cells (300 m) in the  $x$ - and  $y$ -directions, and two cells (283 m) in the diagonal directions (see Figure TFIELD 6-2 for an illustration of the mining-expansion stencil). The PABC-2009 modeling domain and mining zones for the full-mining case are shown in comparison to the 1996 CCA and the CRA-2004 delineations in Figure TFIELD 6-3. The comparison of the current and previous partial-mining cases is shown in Figure TFIELD 6-4. A close-up of the WIPP site and the distribution of minable potash is shown in Figure TFIELD 6-5; it illustrates how the definition inside the WIPP LWB has changed significantly since CRA 2004 PABC. For the PABC-2004, the closest minable potash was approximately 1,230 m from the center of the WIPP panels in the southeast direction; for PABC-2009, this distance has reduced to approximately 670 m (in a more easterly direction).



**Figure TFIELD 6-2. Stencil used to expand areas of predicted potash (red cell with M) to model cells affected by mining-related subsidence from 45° angle of draw (blue cells with A)**

The output of this mining-area delineation is a file that contains one value for each cell in the grid. A value of 1 means the cell lies within a potential mining-affected zone, and a value of 0 means that it is outside a potential mining-affected zone.

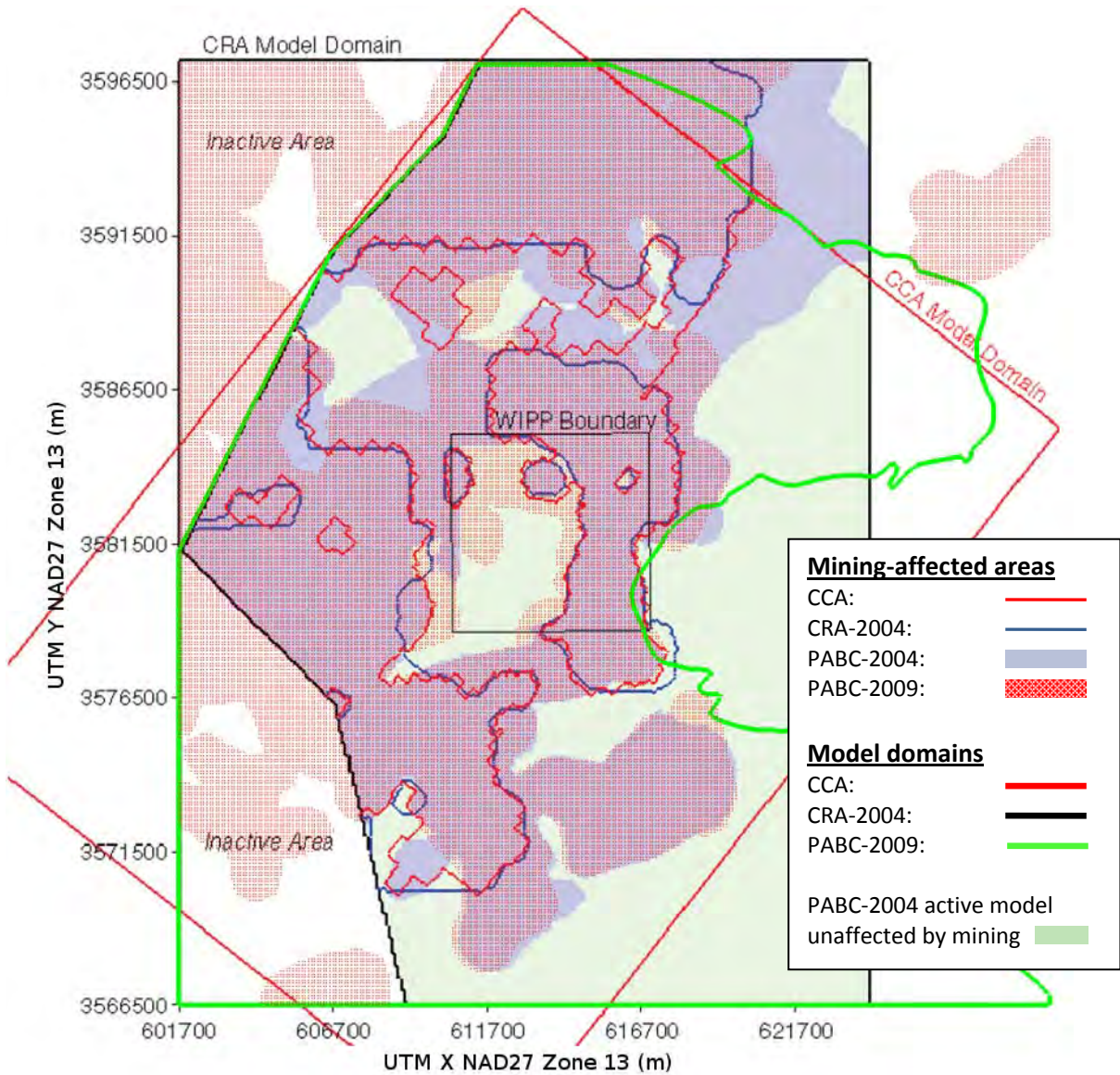


Figure TFIELD 6-3. Definitions of mining-affected areas in full-mining scenario between current and previous models. Base image is Figure 3.2 from Lowry and Kanney (2005).

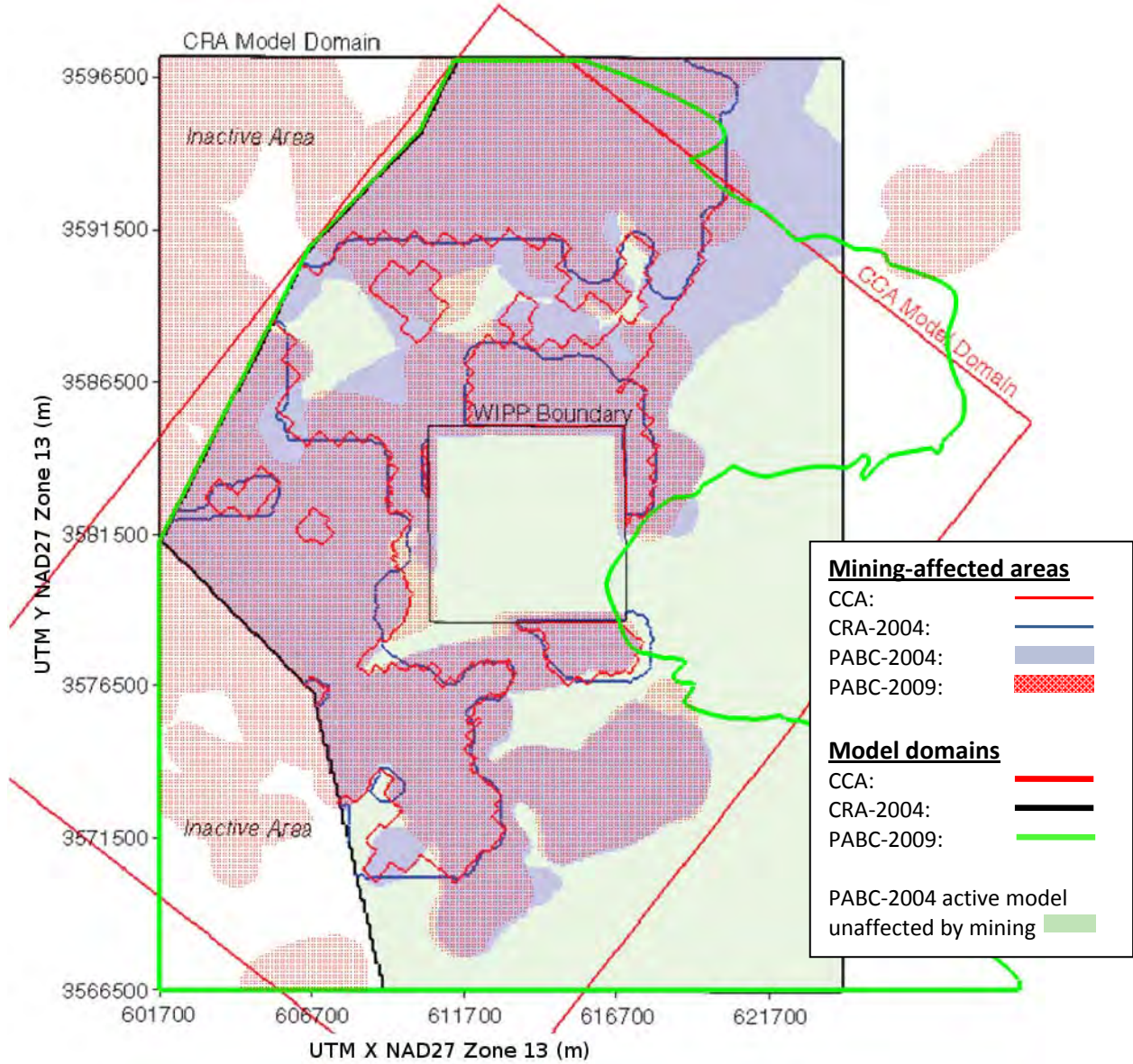
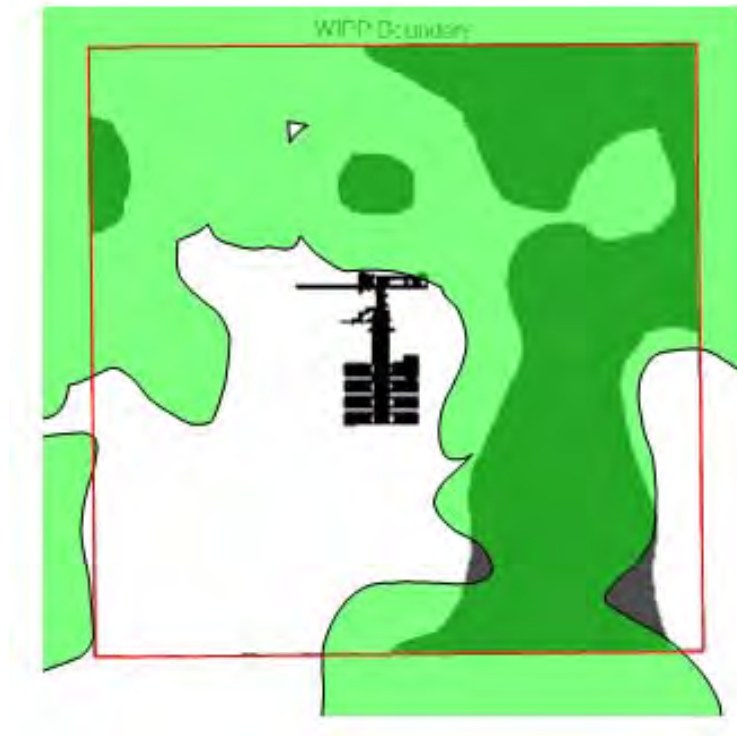


Figure TFIELD 6-4. Definitions of partial-mining-affected areas between current and previous applications; base image is Figure 3.3 from Lowry and Kanney (2005).



**Figure TFIELD 6-5. Comparison of minable potash distribution inside WIPP LWB for PABC-2004 (dark gray) and PABC-2009 (translucent green). The WIPP repository plan is shown for comparison, from Figure 3.6 of Lowry and Kanney (2005)**

### **TFIELD-6.2.3 Use of Mining Zones in Forward Simulations**

The calibration process in Section TFIELD-5 produces 100 sets of transmissivity, horizontal anisotropy, storativity, and areal recharge fields that each minimize the error between observed and model-calculated head distributions. To simulate the effects of mining, each selected T-field is multiplied by its own unique mining scaling factor in areas of potential mining, and MODFLOW is run with these mining-modified T-fields to produce the mining-affected head and flow distributions. The cell-by-cell flow budget files are used in particle tracking and radionuclide transport calculations. To demonstrate stability in mean results, three different sets of mining factors are used, each set forming a replicate (given here as R1, R2, and R3). Thus, for each mining scenario (full and partial), three sets of 100 mining-altered T-fields and related cell-by-cell flow budgets are produced.

### **TFIELD-6.2.4 Particle Tracking Simulations**

In each realization, a single conservative particle is tracked from the UTM NAD27 coordinate  $x = 6135975$  m,  $y = 35813852$  m (i.e., the location of monitoring well C-2737, directly above the center of the WIPP waste panels) to the LWB for each combination of T-field, replicate, and mining scenario using the DTRKMF code. Two main outputs are generated from the suite of particle tracks. First, plots are constructed showing the individual tracks for all 100 T-fields in each scenario for each replicate (six plots total). This allows visual comparison of the prevailing flow

directions for the full- and partial-mining scenarios and the qualitative comparison of the variability of the tracking direction. Secondly, CDFs are constructed for each replicate and scenario, which describe the probability that a water particle will cross the LWB in a given amount of time. The six plots and the CDFs are presented in Section TFIELD-6.3.

### ***TFIELD-6.3 Particle Tracking Results***

Particle tracks were computed using DTRKMF (Rudeen, 2003), which uses the binary cell-by-cell flow budget files produced by MODFLOW-2000. In flow calculations, the full 7.75 m thickness of the Culebra is used, while for transport and particle tracking purposes the thickness is reduced to 4.0 m to focus all flow through the lower, more permeable portion of the Culebra (Holt, 1997). An average value of 16% porosity is used for the particle tracking calculations, as was used in AP-114 Task 7 (Hart et al., 2009). Porosity directly affects transport, but is not needed for the calibration of the flow model.

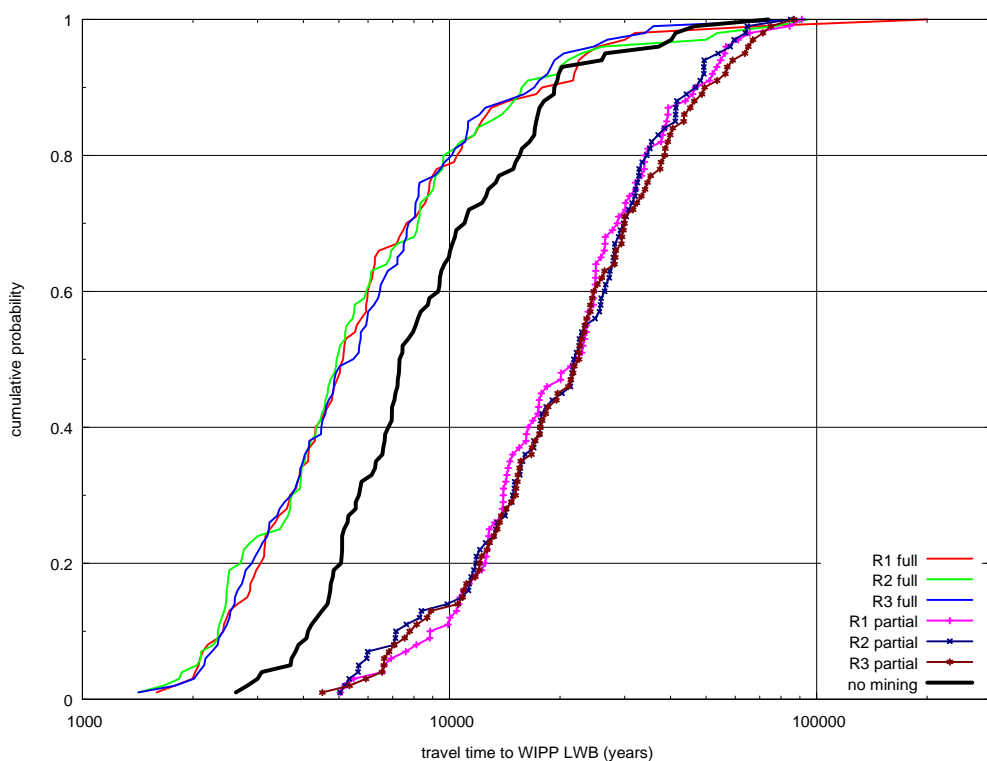
Particle tracking is performed to allow comparison between the two mining scenarios and the non-mining scenario, which was not used in the SECOTP2D radionuclide transport calculations. The particle tracking results illustrate the advective pathway taken by a marked water particle and do not take into consideration retardation, dispersion, or molecular diffusion. The particle tracks also allow easier comparison of the 600 results (each a 1D trace) in a single plot, in contrast showing 600 sets of concentrations (each a 2D field) produced from SECOTP2D.

#### **TFIELD-6.3.1 Particle Travel Times**

Compared to the non-mining scenario (results already given in AP-114 Task 7 (Hart et al., 2009)), the travel times for the partial-mining scenarios are longer, while travel times for the full-mining scenarios are shorter. The median travel time across all three replicates for the full-mining scenario is approximately 0.689 times the median travel time of the non-mined scenario (see Table TFIELD 6-1, Figure TFIELD 6-6 and Figure TFIELD 6-7 for summary statistics and comparison to PABC-2004 results). All advective particle travel times are plotted, but it should be noted that the regulatory limit for radionuclide transport modeling is 10,000 years, taking into consideration retardation, diffusion, and dispersion (which don't apply to particle track modeling). The median travel time across all three replicates for the partial-mining scenario is 3.034 times greater than for the non-mining scenario. For PABC-2004, travel times in both the full- and partial-mining scenarios were slower (longer) than for the non-mining scenario. The CDFs for the full-, partial-, and non-mining scenarios are shown in Figure TFIELD 6-6.

**Table TFIELD 6-1. Particle tracking travel time statistics (years); PABC-2004 statistics from Table 3.22 of Lowry and Kanney (2005)**

Replicate	Statistic	PABC-2009			PABC-2004		
		Full	Partial	No Mining	Full	Partial	No Mining
R1	Median	5,138	22,581	N/A	64,026	117,815	N/A
	Max	200,260	91,119		2,175,165	2,727,191	
	Min	1,591	5,042		2,130	5,185	
R2	Median	4,956	21,999		80,801	148,489	
	Max	94,852	84,929		2,059,263	1,667,084	
	Min	1,421	5,037		2,463	4,855	
R3	Median	5,560	22,537		74,315	118,919	
	Max	93,172	86,758		1,779,512	3,128,693	
	Min	1,421	4,505		2,507	3,314	
Global	Median	5,084	22,376	7,374	70,170	131,705	18,289
	Max	200,260	91,119	73,912	2,175,165	3,128,693	101,205
	Min	1,421	4,505	2,618	2,130	3,314	3,111



**Figure TFIELD 6-6. CDF of advective particle travel times from the center of the WIPP waste panels to the WIPP LWB for full, partial, and non-mining scenarios**

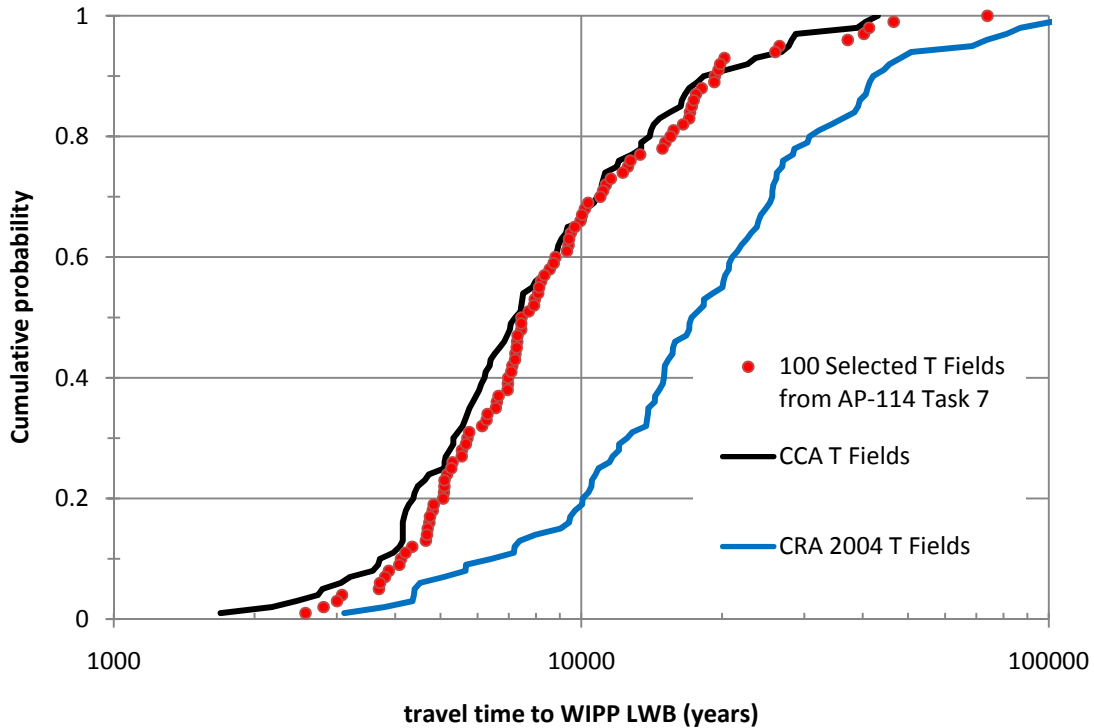


Figure TFIELD 6-7. Comparison of advective particle travel time CDFs for PABC-2009, PABC-2004, and CCA.

### TFIELD-6.3.2 Flow Directions

The particle track directions for the non-, full-, and partial-mining scenarios for the PABC-2009 are illustrated in Figure TFIELD 6-8 to Figure TFIELD 6-11. Figure TFIELD 6-13 shows the non-mining case particle tracks all the way to the edge of the MODFLOW model domain, rather than only to the WIPP LWB. Like past mining scenario calculations (i.e., PABC-2004), there is a strong similarity between the three replicates (R1, R2, and R3) for each scenario (full or partial mining), although the travel directions for the PABC-2009 are different than for the PABC-2004 (Lowry and Kanney, 2005). A larger amount of minable ore exists inside the WIPP LWB, especially the ore immediately to the east of the particle release point; this leads to different effects of full mining on travel times, compared to PABC-2004. Nearly all particles immediately go east to this boundary and then move south along it towards to the edge of the LWB at approximately  $x = 612.75$  km (see Figure TFIELD 6-9 and Figure TFIELD 6-12). This is in contrast to the partial-mining scenario where the tracking directions are more similar to the non-mining scenario, but more evenly distributed spatially along the southern boundary. In the non-mining scenario, most of the particles exit near the high-transmissivity zone at approximately  $x = 615$  km.



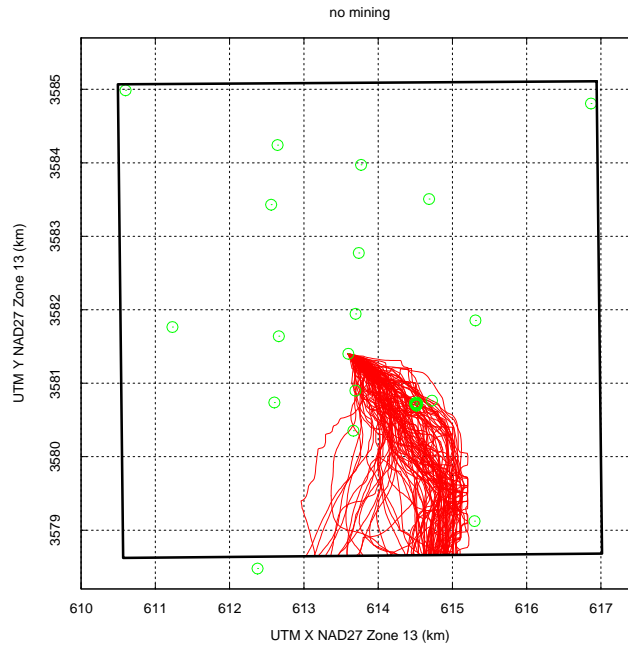


Figure TFIELD 6-8. Particle tracks for non-mining scenario; black box is WIPP LWB, green circles are Culebra monitoring well locations.

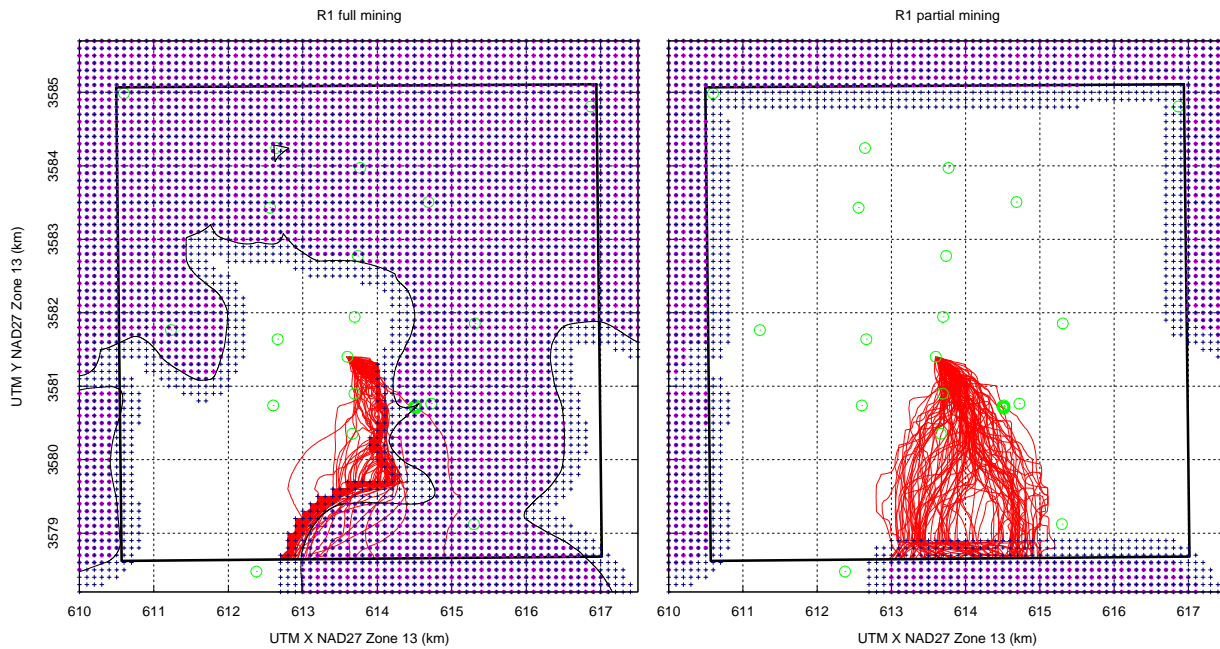
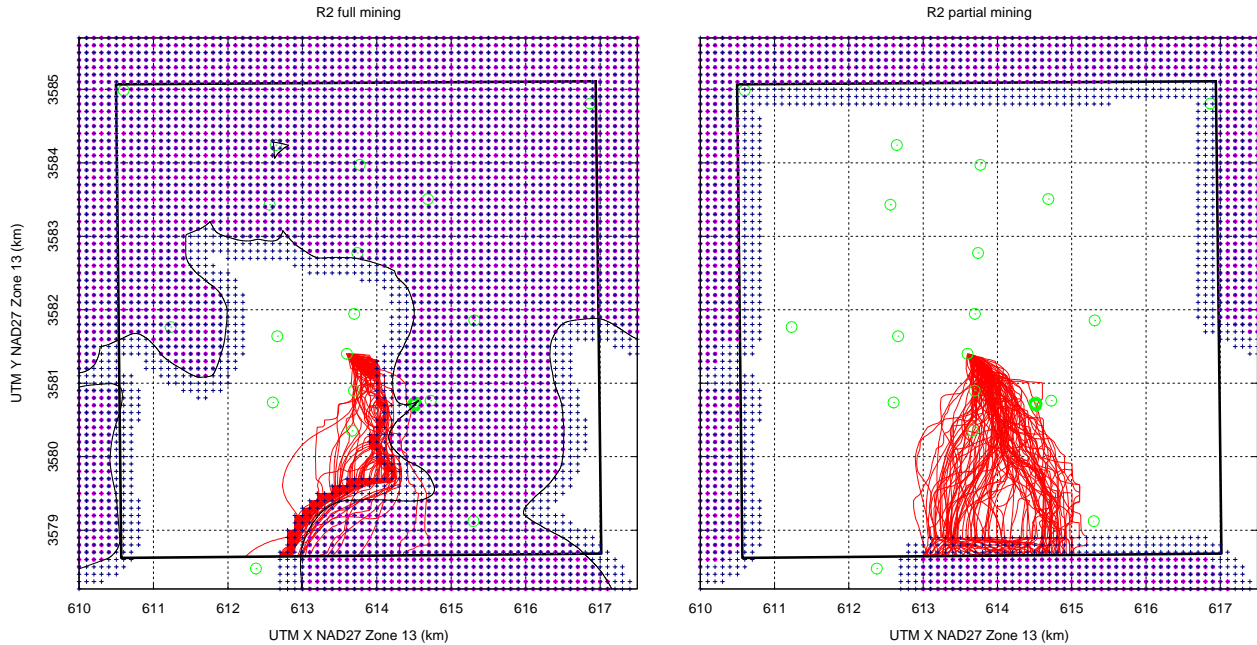
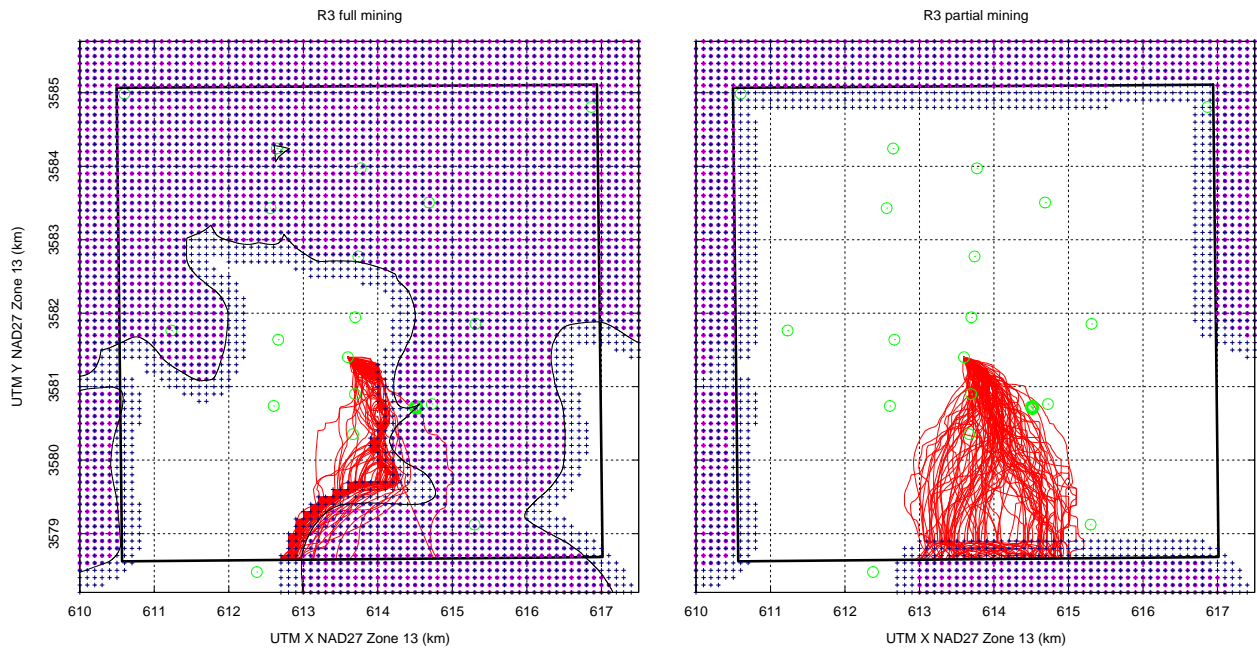


Figure TFIELD 6-9. Particle tracks for R1. Small magenta squares and black crosses indicate centers of MODFLOW cells located within potash and mining-affected areas, respectively; thin black line is minable potash definition.



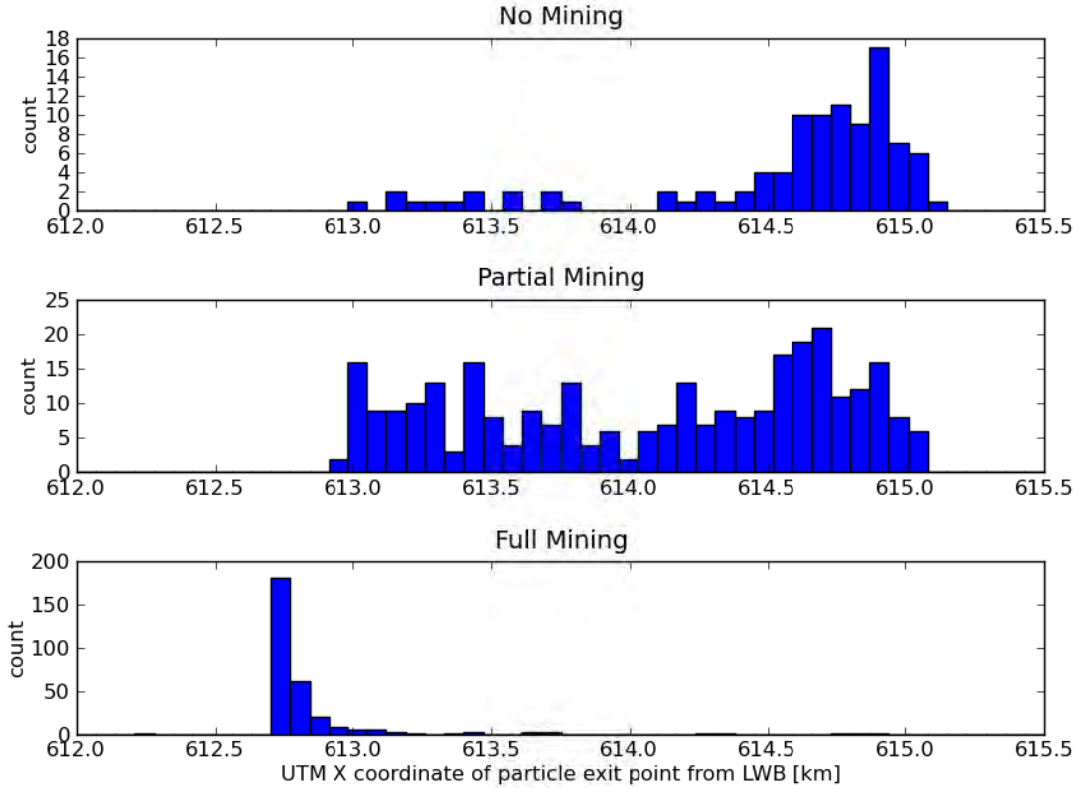
**Figure TFIELD 6-10. Particle tracks for R2. Small magenta squares and black crosses indicate centers of MODFLOW cells located within potash and mining-affected areas, respectively; thin black line is minable potash definition.**



**Figure TFIELD 6-11. Particle tracks for R3. Small magenta squares and black crosses indicate centers of MODFLOW cells located within potash and mining-affected areas, respectively; thin black line is minable potash definition.**

High-transmissivity areas corresponding to the mining-affected zones create preferential pathways through the system (see oranges and yellows in Figure TFIELD 6-14). These preferential pathways result in higher velocities and flow rates through the mining zone and therefore relatively slower

velocities in the non-mined areas. In the partial-mining scenario, where there is no mining inside the WIPP LWB, the preferential pathway goes “around” the LWB, rather than through it (similar to behavior seen in both mining scenarios for PABC-2004). In the full-mining scenario, the mined regions are closer to the release point than in PABC-2004 (see Figure TFIELD 6-5 for comparison), giving the particles a high-transmissivity pathway from the release point to the LWB, resulting in shorter travel times than the non-mined scenario (this behavior is different from that predicted using the PABC-2004 model). A comparison of the median, maximum, and minimum travel times for each scenario is presented in Table TFIELD 6-1.



**Figure TFIELD 6-12. Histograms of particle  $x$ -coordinates at exit point from LWB; full and partial-mining include all three replicates (note different vertical scales between plots; no mining contains 100 particles while mining scenarios include 300 particles)**

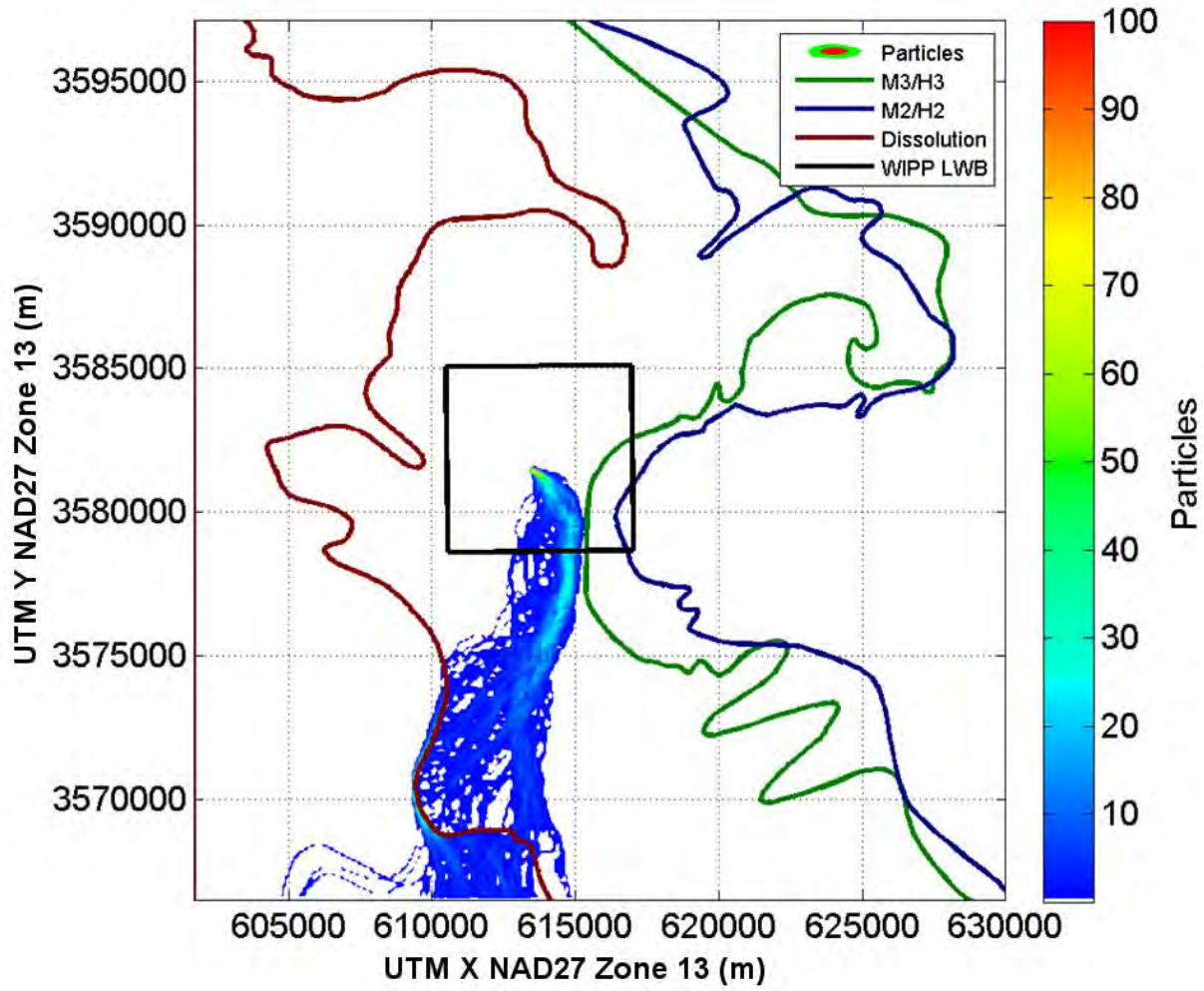


Figure TFIELD 6-13. Particle density in each cell for non-mining scenario.

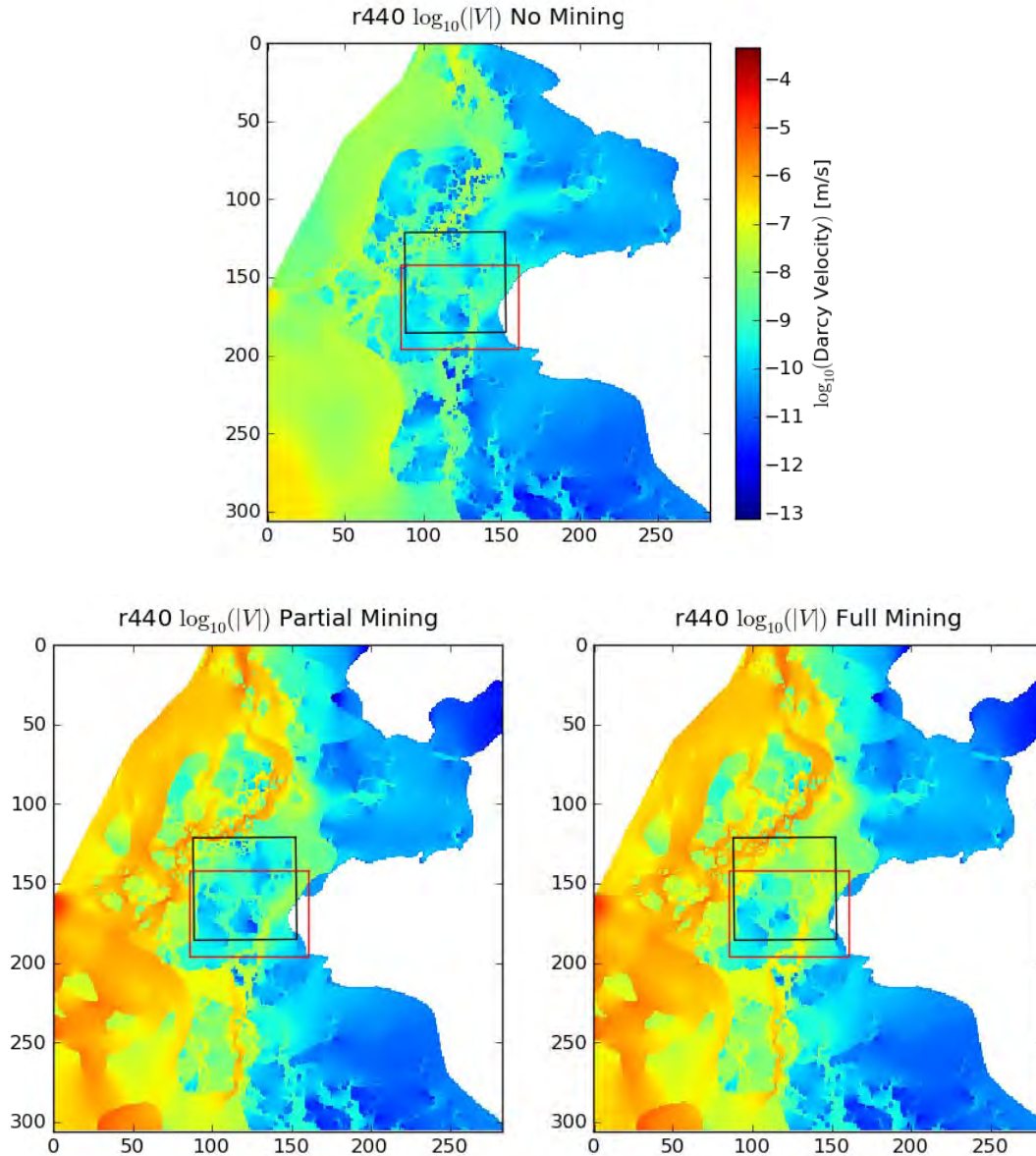


Figure TFIELD 6-14. Magnitude of Darcy flux for r440 R2 for no, partial, and full-mining scenarios using cell-based coordinates; LWB (black) and SECOTP2D transport model domain (red) shown for reference.

### TFIELD-6.3.3 Particle Speeds

Instantaneous speeds (the magnitude of particle velocities) were calculated from the DTRKMF particle locations and times using backwards finite differences,

$$v_{(t_{i+1})} = \frac{\sqrt{[x(t_i) - x(t_{i+1})]^2 + [y(t_i) - y(t_{i+1})]^2}}{t_{i+1} - t_i} \quad (\text{TFIELD 6.2})$$

where a subscript  $i$  indicates the previous time step (a record or line in the DTRKMF output file) and a subscript  $i+1$  is the current time step. This approach assumes a straight line connects the

locations at the beginning and ends of the step, so it is potentially underestimating speeds, but step sizes are small and error should be minimal; these values should be used for qualitative comparisons between realizations and scenarios, rather than quantitative estimates of true particle velocities.

In Figure TFIELD 6-15 through Figure TFIELD 6-18, the color of the diamond indicates the particle velocity; the dots are located at the midpoint of the step, e.g.,  $x_{\text{midpt}} = \frac{1}{2}[x(t_i) + x(t_{i+1})]$ ,  $y_{\text{midpt}} = \frac{1}{2}[y(t_i) + y(t_{i+1})]$ . In the no-mining case (Figure TFIELD 6-15), the highest particle velocities are in the southeastern portion of the particle swarm, corresponding to the high-transmissivity pathway (Hart et al., 2009) exiting the LWB at approximately  $X=614,750$  m (Figure TFIELD 6-12). The effects of the full-mining scenario are clearly evident in the left portions of Figure TFIELD 6-16 through Figure TFIELD 6-18; high particle velocities (yellows and oranges) are found along the margin of the mining-affected areas, where particles enter the increased-transmissivity region. For comparison, in the partial-mining scenario the particles are relatively slowed down and more evenly distributed in the region between the release point and the southern WIPP LWB.

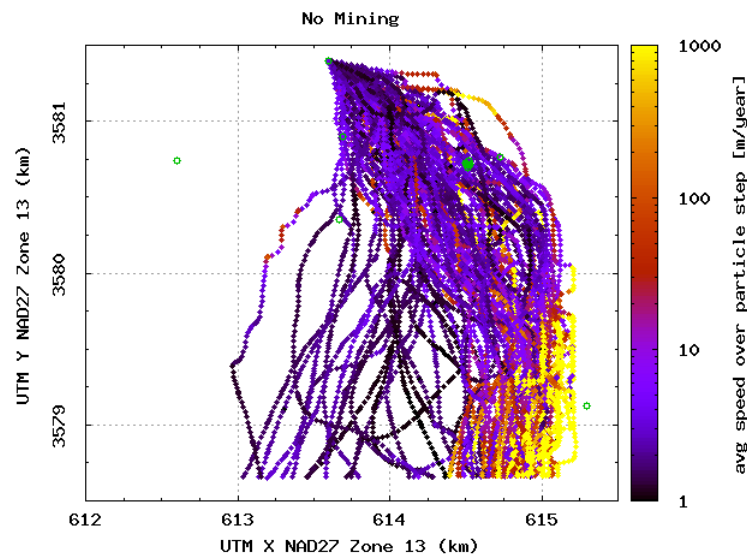


Figure TFIELD 6-15. Particle speeds for non-mining scenario computed from DTRKMF results

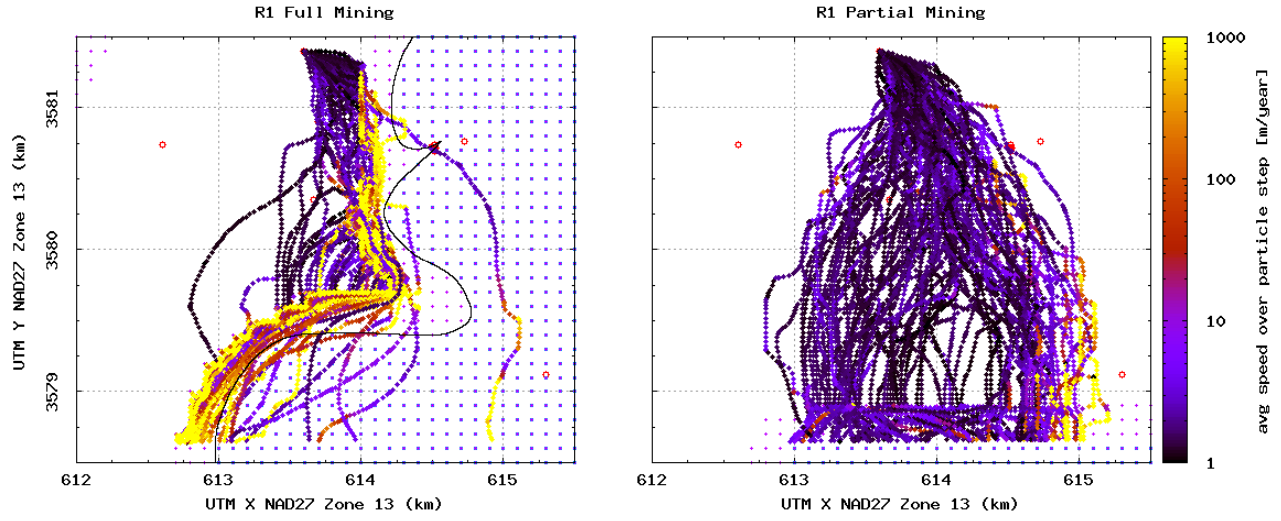


Figure TFIELD 6-16. Particle speeds for R1, computed from DTRKMF results

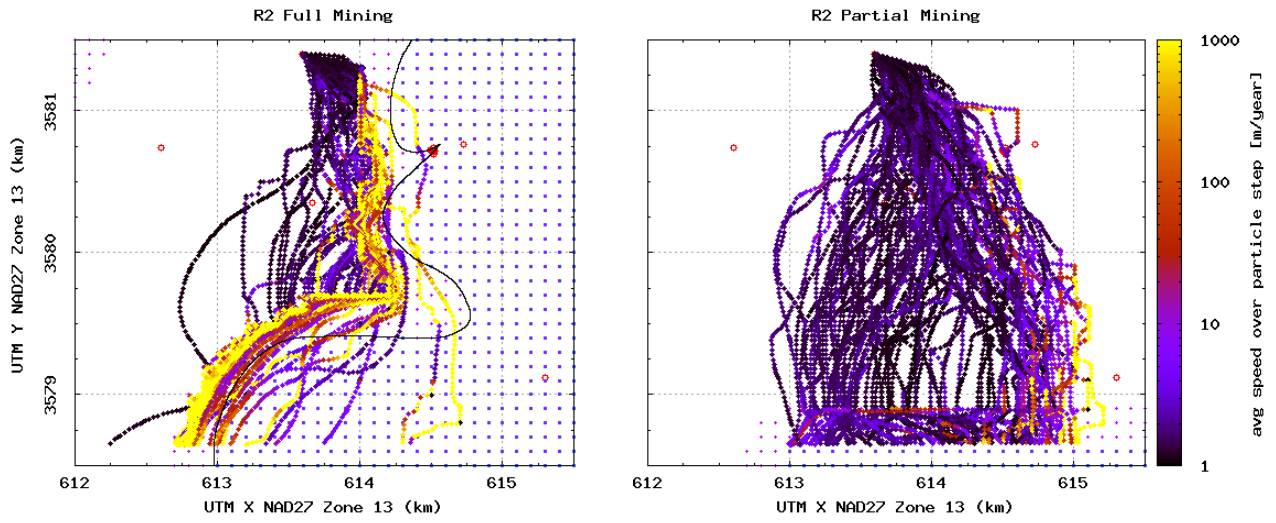


Figure TFIELD 6-17. Particle speeds for R2, computed from DTRKMF results

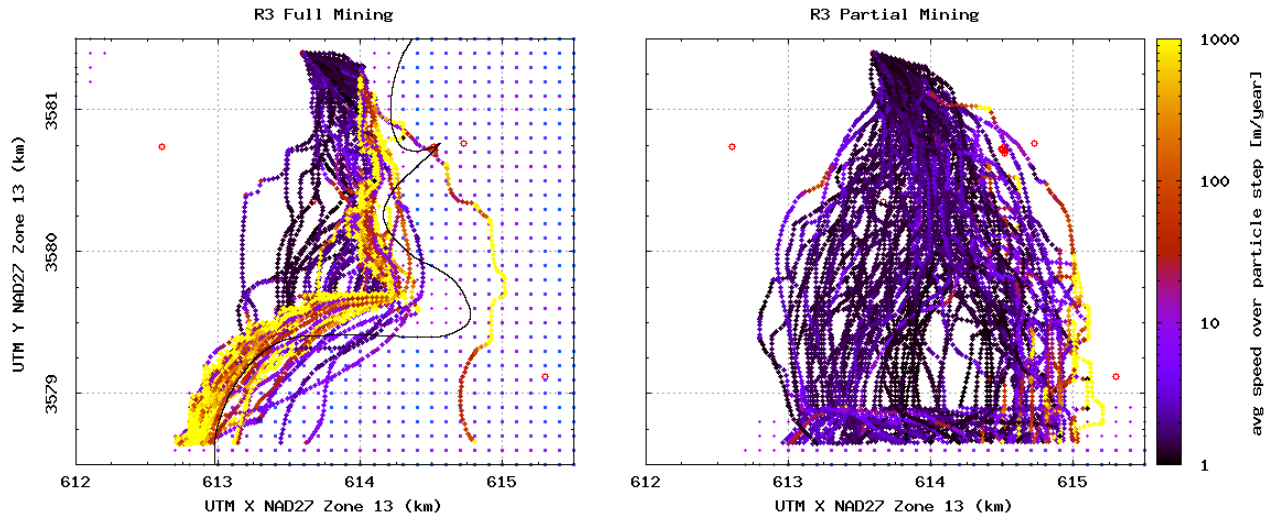


Figure TFIELD 6-18. Particle speeds for R3, computed from DTRKMF results

### TFIELD-6.3.4 Particle Tracking Discussion

Correlation analysis for the PABC-2009 particle tracking calculations shows that travel time and the random mining factor are weakly correlated for the full- (Figure TFIELD 6-19) or partial-mining (Figure TFIELD 6-20) scenarios. This is similar to what was observed for the PABC-2004 (Lowry and Kanney, 2005). The high scatter in Figure TFIELD 6-19 and Figure TFIELD 6-20 indicates that the transmissivity spatial distribution plays the more significant role in determining the travel time than the mining factor does. See Appendix 1 of Kuhlman (2010) for a cross-sectional comparison of transmissivity for each mining type, showing that the variability in the transmissivity due to calibration is on the same order as that due to mining for a single realization. The mining factor plays a weak but slightly larger role in explaining the observed variance for the partial-mining realizations (Figure TFIELD 6-20) than the full-mining realizations (Figure TFIELD 6-19), based on the larger (but still very small)  $R^2$  value for the straight-line fit of  $\log_{10}$  travel times to mining factors.



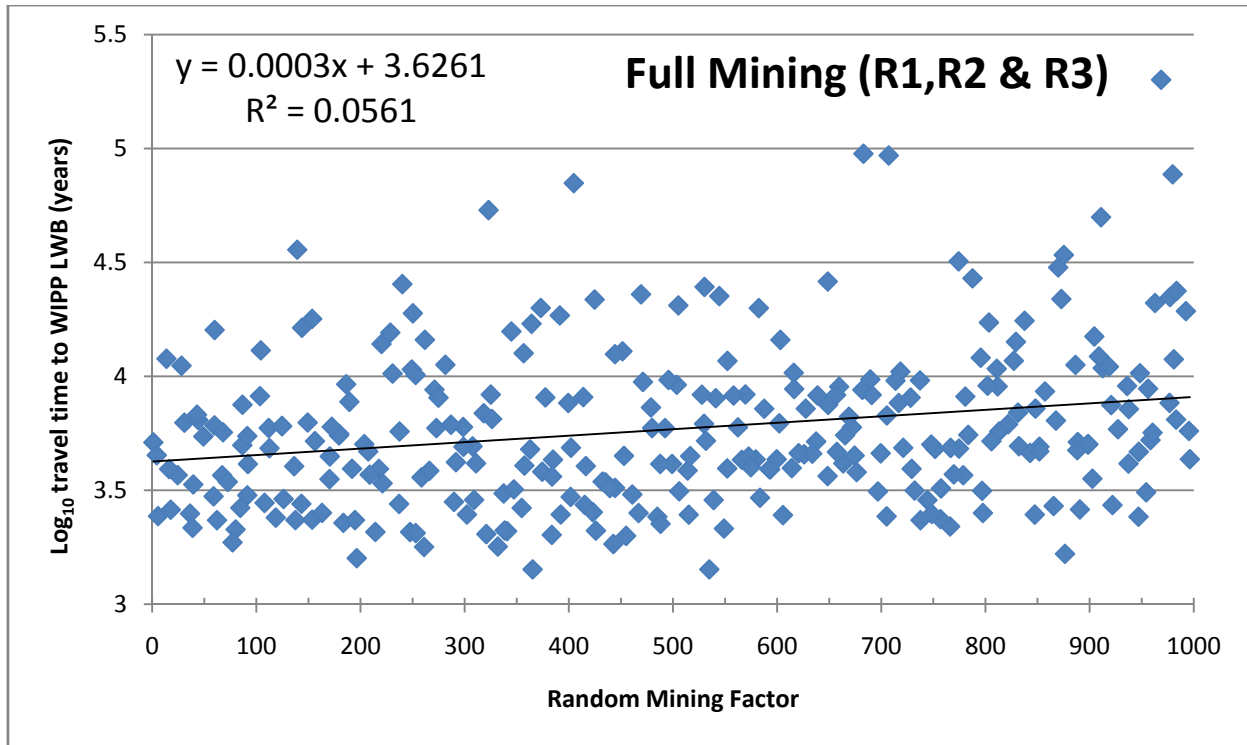


Figure TFIELD 6-19. Mining factor and travel time to WIPP LWB for full-mining scenario (all replicates)

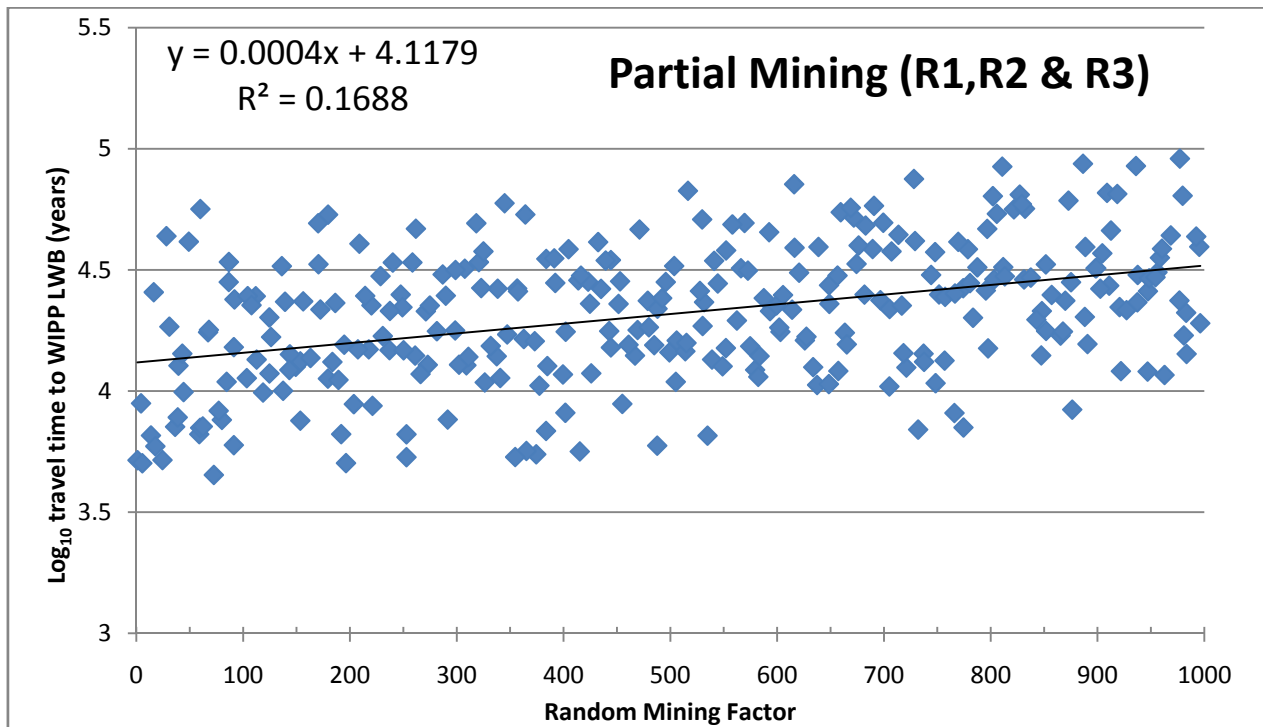


Figure TFIELD 6-20. Mining factor and travel time to WIPP LWB for partial-mining scenario (all replicates)

## **TFIELD-6.4 Mining Modification Summary**

The 100 transmissivity fields resulting from calibration to both steady-state and transient observed freshwater heads in the Culebra (Section TFIELD-5) were modified to account for potential effects due to mining potash from the Salado Formation above the repository. A definition of the areal extent of minable potash was obtained from the Bureau of Land Management (Cranston, 2009) and used to define areas where Culebra transmissivity was increased by a randomly sampled mining factor ( $1 \leq \text{MINP\_FACT} \leq 1000$ ). Two mining scenarios were developed: a full-mining scenario with all minable potash removed and a partial-mining scenario with only potash outside the WIPP LWB removed.

The mining-modified transmissivities were inputs to a MODFLOW flow model, which was used by DTRKMF to compute advective particle tracks from a release point at the center of the WIPP waste panels (C-2737) to the edge of the WIPP LWB. Results show that for the partial-mining scenario, the median particle travel time of 22,376 years is 3.03 times greater than for the non-mining scenario (7,374 years); the median particle travel time for the partial-mining scenario in PABC-2004 was 7.06 times greater than for the non-mining scenario. In contrast to the PABC-2004, the full-mining scenario decreased median travel time to 5,084 years, a factor of 1.45 *faster* than for the non-mining scenario; the median particle travel time for the full-mining scenario in PABC-2004 was 3.84 times slower than for the non-mining scenario. For the partial-mining scenario, the increase in transmissivity due to mining increases the relative flow rate through the mining zones, with a corresponding decrease in flow through the non-mining zones. This decrease in flow through the non-mining zones produces longer travel times for the partial-mining scenario. For the full-mining scenario, the potash definition from BLM (Cranston, 2009) locates minable potash ore much closer to the C-2737 release point than in PABC-2004 (see Figure TFIELD 6-5). This new shortened distance from the release point to minable potash (in the full-mining scenario) reverses the slowing-down trend observed in the PABC-2004 analysis.

As in the PABC-2004 calculations, a very weak positive correlation was found between the travel times and the random mining factor (the higher the random mining factor, the longer the particle travel time – see Figure TFIELD 6-19 and Figure TFIELD 6-20). As the mining factor is increased, the flow through the non-mining areas is decreased, producing longer travel times and the positive correlation. Most of the advective particle travel time variability is due to differences in the base T-fields and not the random mining factor.

## TFIELD-7 Summary

Observed Culebra transmissivities (T) have been related to three deterministic factors: the thickness of overburden above the Culebra, the presence or absence of dissolution of the upper Salado, and the presence or absence of halite in units above and below the Culebra. Culebra T is also related to the occurrence of open, interconnected fractures that cannot be mapped as easily as the other three factors and therefore must be treated stochastically. A linear-regression model for Culebra T has been developed based on these factors that provides an excellent match to the observed data, and can be tested through the collection of additional data. This model was used to create 1000 stochastic realizations of the distribution of Culebra T (“base” T-fields) in the vicinity of the WIPP site.

A MODFLOW-2000 modeling domain was defined extending 30.7 km north-south and 28.4 km east-west, roughly centered on the WIPP site. This domain was discretized into 87,188 uniform 100-m square two-dimensional finite-difference cells. An inactive portion of the northwest corner of the domain is used to represent a no-flow boundary in the axis of Nash Draw. A low-permeability constant-head portion of the eastern section of the domain is used to represent the lithostatic portion of the Culebra sandwiched above and below by halite units. Freshwater head observations in 42 monitoring wells from May 2007 were used as steady-state calibration targets. Drawdown observations in 62 observation wells, in response to nine unique pumping tests, were used as transient calibration targets. A subset consisting of 100 of the 200 calibrated Culebra model realizations was selected based on their ability to simulate these observed heads.

The EPA requires that the potential effects of future potash mining be taken into account when evaluating the performance of the WIPP disposal system. Accordingly, transmissivities in the areas within the model domain where current or future mining might affect the Culebra were scaled by a random multiplier between 1 and 1,000 obtained from LHS. A single multiplier was used for each T-field, applied first to the areas outside the WIPP LWB that might be mined to create a partial-mining T-field, and then to all areas (both inside and outside the WIPP LWB) to create a full-mining T-field. Three statistically similar replicates of mining multipliers were generated, leading to a total of 600 unique T-fields (100 calibrated realizations, 2 mining scenarios, and 3 replicates). The MODFLOW-2000 flow budgets were used from each T-field as input for both advective particle tracking (DTRKMF) and radionuclide solute transport (SECOTP2D).

The non-mined travel times from the center of the WIPP waste panels to the WIPP LWB are similar to those computed for the CCA and therefore faster than those computed for the CRA-2004 PABC. The decrease in travel time to the LWB can be attributed to the presence of a consistent high-transmissivity pathway leaving the south-east portion of the LWB. The presence of this pathway is supported by observed drawdown data from the SNL-14 pumping test.

In the partial-mining case, particle tracks show increased travel times from the center of the WIPP waste panels to the WIPP LWB, compared to the non-mining scenario. In the full-mining case, particle tracks showed decreased travel times to the WIPP LWB, due to the close proximity of minable potash to the center of the WIPP waste panels.

## TFIELD-8      References

- Beauheim, R.L., 1987a. *Analysis of Pumping Tests of the Culebra Dolomite Conducted at the H-3 Hydropad at the Waste Isolation Pilot Plant (WIPP) Site*. Albuquerque, NM: Sandia National Laboratories. SAND86-2311.
- Beauheim, R.L., 1987b. *Interpretation of the WIPP-13 Multipad Pumping Test of the Culebra Dolomite at the Waste Isolation Pilot Plant (WIPP) Site*. Albuquerque, NM: Sandia National Laboratories. SAND87-2456.
- Beauheim, R.L., 1989. *Interpretation of H-11b4 Hydraulic Tests and the H-11 Multipad Pumping Test of the Culebra Dolomite at the Waste Isolation Pilot Plant (WIPP) Site*. Albuquerque, NM: Sandia National Laboratories. SAND89-0536.
- Beauheim, R.L., 2007. Diffusivity mapping of fracture interconnections. In *Proceedings of the 2007 US EPA/NGWA Fractured Rock Conference*. Westerville, OH, 2007. National Ground Water Association.
- Beauheim, R.L., 2008. *Analysis Plan for Evaluation and Recalibration of Cuelbra Transmissivity Fields AP-114, Revision 1*. Carlsbad, NM: Sandia National Laboratories.
- Beauheim, R.L., 2009. *Changes to Culebra T-Field Calibration Procedures under AP-114 Task 7*. Carlsbad, NM: Sandia National Laboratories. ERMS 551437.
- Beauheim, R.L. and Holt, R.M., 1990. Geological and Hydrological Studies of Evaporites in the Northern Delaware Bains for the Waste Isolation Pilot Plant (WIPP). In D.W. Powers, R.M. Holt, R.L. Beauheim and N. Rempe, eds. *Guidebook 14*. Geological Society of America (Dallas Geological Society). pp.45-78.
- Beauheim, R.L. and Ruskauff, G.J., 1998. *Analysis of Hydraulic Tests of the Culebra and Magenta Dolomites and Dewey Lake Redbeds Conducted at the Waste Isolation Pilot Plant Site*. Albuquerque, NM: Sandia National Laboratories. SAND98-0049.
- Bertram, S.G., 1995. *Record of FEP Screening Work, FEP ID#NS-11: Subsidence Associated with Mining Inside or Outside the Controlled Area*. Carlsbad, NM: Sandia National Laboratories. ERMS 230761.
- Bowman, D.O. and Roberts, R.M., 2008. *Analysis Report for AP-070, Analysis of Hydraulic Tests Performed in IMC-461, SNL-6, H-11b2, H-15, and C-2737*. Carlsbad, NM: Sandia National Laboratories. ERMS 539221.
- Camphouse, R.C., 2010. *CCDFGF Analysis Package for the 2009 Performance Assessment Baseline Calculation (AP-145)*. Carlsbad, NM: Sandia National Laboratories. 553027.
- Chavez, M., 2006. *NP 19-1 Software Requirements, Revision 12*. Carlsbad, NM: Sandia National Laboratories.

- Chavez, M., 2008. *NP 9-1 Analyses, Revision 7*. Carlsbad, NM: Sandia National Laboratories.
- Clayton, D.J., 2009a. *Analysis Plan for the CRA-2009 Performance Assessment Baseline Calculation, AP-145 Revision 0*. Carlsbad, NM: Sandia National Laboratories. ERMS 551603.
- Clayton, D.J., 2009b. *Update to the Kd values for the PABC-2009*. Carlsbad, NM: Sandia National Laboratories. ERMS 552395.
- Clayton, D.J., Camphouse, R.C., Garner, J.W., Ismail, A.E., Kuhlman, K.L., Kirchner, T.B. and Nemer, M.B., 2010. *Summary Report of the CRA-2009 Performance Assessment Baseline Calculation*. Carlsbad, NM: Sandia National Laboratories. ERMS 553039.
- Clayton, D.J., Dunagan, S., Garner, J.W., Ismail, A.E., Kirchner, T.B., Kirkes, G.R. and Nemer, M.B., 2008. *Summary Report of the 2009 Compliance Recertification Application Performance Assessment*. Carlsbad, NM: Sandia National Laboratories. ERMS 548862.
- Corbet, T., 1995. *Record of FEP Screening Work FEP ID# NS-9 Justification of SECO2D Approximation for PA Transport Calculation*. Carlsbad, NM: Sandia National Laboratories. ERMS 230802.
- Corbet, T., 1996. *Two-dimensional Assumption for Culebra Calculations Technical Memorandum*. Carlsbad, NM: Sandia National Laboratories. ERMS 230802.
- Corbet, T.F. and Knupp, P.M., 1996. *The role of regional groundwater flow in the hydrogeology of the Culebra Member of the Rustler Formation at the Waste Isolation Pilot Plant (WIPP), Southeastern New Mexico*. Albuquerque, NM: Sandia National Laboratories. SAND96-2133.
- Corbet, T. and Swift, P., 1996. *Parameters required for SECOFL2D: Climate Index*. Carlsbad, NM: Sandia National Laboratories. ERMS 237465.
- Cotsworth, E., 2005. *EPA Letter on Conducting the Performance Assessment Baseline Change (PABC) Verification Test*. Washington, D.C.: U.S. Environmental Protection Agency, Office of Radiation and Indoor Air. ERMS 538858.
- Cotsworth, E., 2009. *EPA CRA-2009 First Set of Completeness Comments*. Washington, D.C.: U.S. Environmental Protection Agency, Office of Radiation and Indoor Air. ERMS 551444.
- Cranston, C.C., 2009. *Minable Potash Ore*. Carlsbad, NM: Bureau of Land Management. ERMS 551120.
- Currie, J.B. and Nwachukwu, S.O., 1974. Evidence on incipient fracture porosity in reservoir rocks at depth. *Bulletin of Canadian Petroleum Geology*, 22, pp.42-58.

- Deutsch, C.V. and Journel, A.G., 1998. *GSLIB: Geostatistical Software Library and User's Guide*. 2nd ed. New York: Oxford University Press.
- Doherty, J., 2000. *PEST Manual*. Brisbane, Australia: Watermark Numerical Computing.
- ESRI, 1998. *ESRI Shapefile Technical Description - An ESRI White Paper*. Redlands, CA: Environmental Systems Research Institute, Inc.
- Harbaugh, A.W., Banta, E.R., Hill, M.C. and McDonald, M.G., 2000. *MODFLOW 2000: The U.S. Geological Survey Modular Ground-Water Model User Guide*. Reston, VA: U.S. Geological Survey. OFR 00-92.
- Hart, D.B., 2010. *WIPP PA Validation Document for MODFLOW-2000 Version 1.6: addenda for direct solver*. Carlsbad, NM: Sandia National Laboratories. ERMS 552422.
- Hart, D.B., Beauheim, R.L. and McKenna, S.A., 2009. *Analysis Report for Task 7 of AP-114: Calibration of Culebra Transmissivity Fields*. Carlsbad, NM: Sandia National Laboratories. ERMS 552391.
- Hart, D.B., Holt, R.M. and McKenna, S.A., 2008. *Analysis Report for Task 5 of AP-114: Generation of Revised Base Transmissivity Fields*. Carlsbad, NM: Sandia National Laboratories. ERMS 549597.
- Hillesheim, M.B., Hillesheim, L.A. and Toll, N.J., 2007. Mapping of Pressure-Head Responses of a Fractured Rock Aquifer to Rainfall Events. In *Proceedings of the 2007 EPA/NGWA Fractured Rock Conference*. Westerville, OH, 2007. National Groundwater Association.
- Holt, R.M., 1997. *Conceptual Model for Transport Processes in the Culebra Dolomite Member of the Rustler Formation*. Albuquerque, NM: Sandia National Laboratories. SAND97-0194.
- Holt, R.M., Beauheim, R.L. and Powers, D.W., 2005. Predicting fractured zones in the Culebra Dolomite. In B. Faybishenko, P.A. Witherspoon and J. Gale, eds. *Dynamics of Fluids and Transport in Fractured Rock*. American Geophysical Union. pp.103-16.
- Holt, R.M. and Powers, D.W., 1988. *Facies variability and post-depositional alteration within the Rustler Formation in the vicinity of the Waste Isolation Pilot Plant, southeastern New Mexico*. Carlsbad, NM: Department of Energy. WIPP-DOE-88-004.
- Holt, R.M. and Yarbrough, L., 2002. *Analysis Report, Task 2 of AP-088, Estimating Base Transmissivity Fields*. Carlsbad, NM: Sandia National Laboratories. ERMS 523889.
- Johnson, P.B., 2009. *Potentiometric Surface, Adjusted to Equivalent Freshwater Heads, of the Culebra Dolomite Member of the Rustler Formation near the WIPP Site*. Carlsbad, NM: Sandia National Laboratories. ERMS 548162.

- Johnson, P.B., 2009. *Routine Calculations Report In Support of Task 6 of AP-114: Potentiometric Surface, Adjusted to Equivalent Freshwater Heads, of the Culebra Dolomite member of the Rustler Formation near the WIPP Site, Revision 2*. Carlsbad, NM: Sandia National Laboratories. ERMS 551116.
- Kelly, T.E., 2009. *EPA Third Letter Requesting Additional Information on the CRA-2009*. Washington, D.C.: U.S. EPA Office of Radiation and Indoor Air. ERMS 552374.
- Kirchner, T., 2008. *User's Guide to CVS, ReadScript.py, and Related Utilities, Version 1.00*. Carlsbad, NM: Sandia National Laboratories. ERMS 550579.
- Kirchner, T.B., 2010. *Generation of the LHS Samples for the AP-145 (PABC09) PA calculations*. Carlsbad, NM: Sandia National Laboratories. ERMS 552905.
- Kuhlman, K.L., 2009. *AP-144 Analysis Plan for the Calculation of Culebra Flow and Transport for CRA2009PABC*. Carlsbad, NM: Sandia National Laboratories. ERMS 551676.
- Kuhlman, K.L., 2010. *Analysis Report for the CRA-2009 PABC Culebra Flow and Transport Calculations (AP-144)*. Carlsbad, NM: Sandia National Laboratories. ERMS 552951.
- Leigh, C.D., Kanney, J.F., Brush, L.H., Garner, J.W., Kirkes, G.R., Lowry, T., Nemer, M.B., Stein, J.S., Vugrin, E.D., Wagner, S. and Kirchner, T.B., 2004. *2004 Compliance Recertification Application Performance Assessment Baseline Calculation, Revision 0*. Carlsbad, NM: Sandia National Laboratories. ERMS 541521.
- Long, J.J., 2010. *Execution of Performance Assessment Codes for the CRA-2009 Performance Assessment Baseline Calculation*. Carlsbad, NM: Sandia National Laboratories. ERMS 552947.
- Lowry, T.L., 2003a. *Analysis Report, Task 5 of AP-088: Evaluation of Mining Scenarios*. Carlsbad, NM: Sandia National Laboratories. ERMS 531138.
- Lowry, T.L., 2003b. *Analysis Report, Tasks 2 & 3 of AP-100: Grid Size Conversion and Generation of SECOTP2D Input*. Carlsbad, NM: Sandia National Laboratories. ERMS 531137.
- Lowry, T.S., 2004. *Analysis Report for Inclusion of Omitted Areas in Mining Transmissivity Calculations in Response to EPA Comment G-11*. Carlsbad, NM: Sandia National Laboratories. ERMS 538218.
- Lowry, T.S. and Kanney, J.F., 2005. *Analysis Report for the CRA-2004 PABC Culebra Flow and Transport Calculations*. Carlsbad, NM: Sandia National Laboratories. ERMS 541508.
- MacKinnon, R.J. and Freeze, G., 1997a. *Summary of EPA-Mandated Performance Assessment Verification Test (Replicate 1) and Comparison With the Compliance Certification*

- Application Calculations, Revision 1*. Carlsbad, NM: Sandia National Laboratories. ERMS 422595.
- MacKinnon, R.J. and Freeze, G., 1997b. *Summary of Uncertainty and Sensitivity Analysis Results for the EPA-Mandated Performance Assessment Verification Test, Rev 1*. Carlsbad, NM: Sandia National Laboratories. ERMS 420669.
- MacKinnon, R.J. and Freeze, G., 1997c. *Supplemental Summary of EPA-Mandated Performance Assessment Verification Tests (All Replicates) and Comparison With the Compliance Certification Application Calculations, Revision 1*. Carlsbad, NM: Sandia National Laboratories. ERMS 414880.
- McKenna, S.A. and Hart, D.B., 2003. *Analysis report for Task 4 of AP-088: Conditioning of Base T Fields to Transient Heads*. Carlsbad, NM: Sandia National Laboratories. ERMS# 531124.
- McKenna, S.A. and Wahi, A., 2006. Local Hydraulic Gradient Estimator Analysis of Long-Term Monitoring Networks. *Ground Water*, 44(5), pp.723-31.
- Mehl, S.W., 2001. *MODFLOW-2000, The US Geological Survey Modular Ground-Water Model User Guide to the Link-AMG (LMG) Package for Solving Matrix Equations using an Algebraic Multigrid Solver*. USGS (US Geological Survey). OFR 01-177.
- Meigs, L.C., Beauheim, R.L. and Jones, T.L., eds., 2000. *Interpretation of Tracer Tests Performed in the Culebra Dolomite at the Waste Isolation Pilot Plant Site*. Albuquerque, NM: Sandia National Laboratories. SAND97-3109.
- Powers, D.W., 2002. *Addendum to Analysis Report, Task 1 of AP-088, Construction of Geologic Contour Maps*. Carlsbad, NM: Sandia National Laboratories. ERMS 523886.
- Powers, D.W., 2002. *Analysis report Task 1 of AP-088, Construction of geologic contour maps*. Carlsbad, NM: Sandia National Laboratories. ERMS 522085.
- Powers, D.W., 2003. *Addendum 2 to Analysis report Task 1 of AP-088, Construction of geologic contour maps*. Carlsbad, NM: Sandia National Laboratories. ERMS 522085.
- Powers, D.W., 2006. *Analysis Report Task 1B of AP-114: Identify possible area of recharge to the Culebra west and south of WIPP*. Carlsbad, NM: Sandia National Laboratories. ERMS 547094.
- Powers, D.W., 2007a. *Analysis Report for Task 1A of AP-114: Refinement of Rustler Halite Margins Within the Cuelbra Modeling Domain*. Carlsbad, NM: Sandia National Laboratories. ERMS 547559.



- Powers, D.W., 2007b. *Analysis Report for Task 1A of AP-114: refinement of Rustler Halite margins within the Culebra modeling domain*. Carlsbad, NM: Sandia National Laboratories. ERMS 547559.
- Powers, D.W. and Holt, R.M., 1995. *Regional geological processes affecting Rustler hydrogeology*. IT Corporation for Westinghouse Electric Corporation.
- Powers, D.W. and Holt, R.M., 1999. The Los Medanos Member of the Permian Rustler Formation. *New Mexico Geology*, 21(4), pp.97-103.
- Powers, D.W. and Holt, R.M., 2000. The salt that wasn't there: mudflat facies equivalents to halite of the Permian Rustler Formation, southeastern New Mexico. *Journal of Sedimentary Research*, 70(1), pp.29-36.
- Powers, D.W., Holt, R.M., Beauheim, R.L. and McKenna, S.A., 2003. Geologic factors related to the transmissivity of the Culebra Dolomite Member, Permian Rustler Formation, Delaware Basin, southeastern New Mexico. In K.S. Johnson and J.T. Neal, eds. *Evaporite Karst and engineering/environmental problems in the United States*. 109th ed. Oklahoma Geological Survey. pp.211-18.
- Powers, D.W., Holt, R.M., Beauheim, R.L. and Richardson, R.G., 2006. Advances in depositional models of the Permian Rustler Formation, southeastern New Mexico. In *Caves & Karst of Southeastern New Mexico*. Fifty-seventh Annual Field Conference Guidebook ed. NM Geological Society. pp.267-76.
- Powers, D.W., Lambert, S.J., Shaffer, S.-E., Hill, L.R. and Weart, W.D., eds., 1978. *Geological Characterization Report, Waste Isolation Pilot Plant (WIPP) Site, Southeastern New Mexico*. Albuquerque, NM: Sandia National Laboratories. SAND78-1596.
- Powers, D.W. and Owsley, D., 2003. A field survey of evaporite karst along NM 128 realignment routes. In K.S. Johnson and J.T. Neal, eds. *Evaporite karst and engineering / environmental problems in the United States*. 109th ed. Oklahoma Geological Survey. pp.233-40.
- Ramsey, J.L., 1997. *WIPP PA User's Manual for SECOTP2D, Version 1.41*. Carlsbad, NM: Sandia National Laboratories. ERMS 245734.
- Ramsey, J.L. and Wallace, M., 1996. *Analysis Package for the Culebra Flow and Transport Calculations (Task 3) of the Performance Assessment Analyses Supporting the Compliance Certification Application*. Carlsbad, NM: Sandia National Laboratories. ERMS 240516.
- Roberts, R.M., 2006. *Analysis Report for AP-070, Analysis of Culebra Pumping Tests Performed Between December 2003 and August 2005*. Carlsbad, NM: Sandia National Laboratories. ERMS 543901.

- Roberts, R.M., 2007. *Analysis Report for AP-070, Analysis of Culebra Hydraulic Tests Performed Between June 2006 and September 2007*. Carlsbad, NM: Sandia National Laboratories. ERMS 547418.
- Rudeen, D.K., 2003. *User's Manual for DTRKMF Version 1.00*. Carlsbad, NM: Sandia National Laboratories. ERMS 523246.
- Salari, K. and Blaine, R., 1996. *WIPP PA User's Manual for SECOTP2D, Version 1.30*. Carlsbad, NM: Sandia National Laboratories. ERMS 236695.
- Toll, N.J. and Johnson, P.B., 2006a. *Routine Calculations Report In Support of Task 6 of AP-114, SNL-14 August 2005 Pumping Test Observation Well Data Processing, Summary of Files*. Carlsbad, NM: Sandia National Laboratories. ERMS 543371.
- Toll, N.J. and Johnson, P.B., 2006b. *Routine Calculations Report In Support of Task 6 of AP-114, WIPP-11 February 2005 Pumping Test Observation Well Data Processing - Summary of Files*. Carlsbad, NM: Sandia National Laboratories. ERMS 543651.
- U.S. DOE, 1996. *Title 40 CFR Part 191 Compliance Certification Application for the Waste Isolation Pilot*. Carlsbad, NM: U.S. Department of Energy Waste Isolation Pilot Plant, Carlsbad Area Office. DOE/CAO-1996-2184.
- U.S. DOE, 2004. *Title 40 CFR Part 191 Subparts B and C Compliance Recertification Application for the Waste Isolation Pilot Plant*. Carlsbad, NM: US Department of Energy Carlsbad Field Office. DOE/WIPP 2004-3231.
- U.S. EPA, 1993. *Title 40 CFR Part 191 Environmental Radiation Protection Standards for the Management and Disposal of Spent Nuclear Fuel, High-Level and Transuranic Radioactive Wastes; Final Rule Federal Register*. Vol 58 66398-66416.
- U.S. EPA, 1996. 40 CFR Part 194: Criteria for the Certification and Recertification of the Waste Isolation Pilot Plant's Compliance with 40 CFR Part 191 Disposal Regulations; Final Rule., 1996. Federal Register Vol 61, 5223-5245.
- U.S. EPA, 1998. *Criteria for the Certification and Recertification of the Waste Isolation Pilot Plant's Compliance with the Disposal Regulations: Certification Decision: Final Rule. Federal Register, Vol. 63*. ERMS 251924.
- Vine, J.D., 1963. *Surface Geology of the Nash Draw Quadrangle, Eddy County, New Mexico*. U.S. Geological Survey. Bulletin 1141-B.
- Wallace, M.G., 1996. *Record of FEP Screening Work, FEP ID#NS-11: Subsidence Associate with Mining Inside or Outside the Controlled Area*. Carlsbad, NM: Sandia National Laboratories. ERMS 240816.